MRI-PET for Investigating Cerebral Iron-Load and Associated Pathology in Preclinical Alzheimer's Disease

---

Dissertation

zur

Erlangung der naturwissenschaftlichen Doktorwürde
(Dr. sc. nat.)

vorgelegt der

Mathematisch-naturwissenschaftlichen Fakultät

der

Universität Zürich

von

Jiri Marinus Gerardus van Bergen

aus den Niederlanden

Promotionskommission

Prof. Dr. Roger M. Nitsch (Vorsitz)
Prof. Dr. Klaas P. Prüssmann
PD Dr. Paul Gerson Unschuld (Leitung der Dissertation)

Zürich, 2018

Table of Contents

1 Acknowledgements

It is hard to believe that the more than three years I have been working on this accumulated thesis have passed so quickly. Looking back, it’s truly an accumulated work that would not have been possible without the efforts of many, thank you all!

I would like to start by thanking Prof. Nitsch and Prof. Hock, who created the environment in which my supervisor, Dr. Paul Gerson Unschuld, was able to let me do all this work. Of course, the appreciation goes to Paul for making me part of the Gersonians and supporting me so much throughout all these years. There were many times when the research seemed endless, that none of the hard work actually resulted in any noteworthy results, but a simple meeting with Paul could change all that. The unmatched ability to see the positive side of everything would sprout so many new ideas and research paths to take that after every meeting my spirits and motivation were high. Yes, some research paths turned out to not be completely realistic or even technically impossible, but they eventually lead to the interesting results in this work. I could not have wished for a more supportive and motivated supervisor!

None of the QSM work would have been possible without the great time I had in Baltimore with Xu and Peter van Zijl. Not only during that time, but also during my time in Zurich there was always feedback from both of you that improved all of my abstracts, papers and even this thesis. Thank you for always sharing your knowledge on methods and making sure I always perform research in the best way possible.

Without the support of Prof. Pruessman the most cutting-edge parts of this and future work would not have been possible, I am very grateful for this. On top of that he gave me great excitement by informing me of another person doing QSM research in Zurich. Thank you, Pinar for being a discussion-partner in all things QSM! While the results are not yet in this thesis, working with Laetitia and Nicole was very intellectually stimulating and reminded me of the fun of doing hands-on experiments, even if sometimes things fail, I enjoyed it very much.

In this thesis there are a lot of things that sound easy, like acquiring all these imaging and neuropsychological testing data. But the reality is quite the opposite! Thank you to the team in Schlieren: Anton, the doctors, the neuropsychologists, the interns and the support staff. In particular to Marlena, Sabrina and the other technicians at the MRI scanners that had to endure me constantly checking if everything was set perfectly and me making the tweaks that caused weird scanner problems. This brings me to another irreplaceable part of this research puzzle: Valerie. It was a lot of fun working with you, since you understood very well all the things that were going wrong and why. You were always there to help us with the latest idea of Paul and me, or to just tell us if it was a bad idea. And in case something went wrong without Valerie there, luckily Edwin was always there to offer assistance or troubleshooting when I wasn't around. Thank you Edwin for that, and all the interesting discussions over the years.

Schlieren and Hegibach would not have been the same without all the people that made coming to work fun! Noemi, Matthias, Alicia, Daniel and Derya, you not only helped my work by performing the neurophysiological assessments of all study participants, but also by creating a great atmosphere at work to discuss basically any aspect of work and life. The same applies to Rafael and Simon, who were both fun to be around and detrimental to this thesis by making it possible for me to graduate relatively quickly by acquiring all the data before even my first day in Zurich. Thank you Vera, for not only administrative support, but also being a great friend that was always had a positive outlook for me and of whom I learned so much.

No part of my PhD experience would have been the same without Frances and Clemens. Clemens for always being direct and decisive about work, pushing me to work harder by setting such a great example. But also for being my friend outside work, explaining me the Swiss ways of extreme hiking, the language and just always being so genuinely welcoming to me. Frances, you and I were the core-Gersonians for a long time and together we experienced and helped each other through all the highs and lows of what being a Gersonian means. It's hard to summarize the experience and all the stories shared and told, but I am very happy to have had you there for it! Thank you, Clemens and Frances, for being such great friends.

Thank you to my parents for since a young age creating such a supportive environment and never doubting my path, even if it led me away from the Netherlands and you. There were points in time where you were even more certain I could finish this PhD than I was!

Lastly, I would not have been here at all without you, Maria. You supported me throughout these years and through thoughtful remarks pushed me to work harder while keeping everything in perspective.

2 Summary

Alzheimer's disease (AD) is a neurogenerative disease that leads to memory loss and is the most common form of dementia. Its main pathological hallmark is the amyloid-β (Aβ) protein in its soluble and aggregated forms, which according to the amyloid hypothesis triggers neurodegeneration in AD. While there are strong correlations between β-amyloid plaque-load and cognitive decline on an individual and group level, there are also numerous adults with clinically silent AD pathology. These elderly adults have significant accumulations of β-amyloid plaques in the absence of cognitive impairment. Several neuropathological changes have been shown to occur in diseased brains, including aggregation of pathological tau, vascular damage, alterations in brain functioning and neuroinflammation. In recent years there has been evidence that iron dyshomeostasis in various ways might influence the effect and progression of neurodegeneration. In three studies in this work we have used neuroimaging markers of β-amyloid plaques, iron, vascular integrity and functional connectivity to explore possible effects of iron-load in populations of cognitively healthy and mildly impaired older adults. In particular, Quantitative Susceptibility Mapping (QSM) MRI was implemented both at ultra-high field strength of 7T and high field strength of 3T, allowing for in vivo inferences on iron-load in cortical gray matter.

In the first study we investigated a sample of 37 subjects of which 15 had mild cognitive impairment (MCI) using 7T MRI. Using functional connectivity analysis, we found altered brain functioning in subjects with higher iron-load. In particular in the medial prefrontal cortex a significant increase in connectivity was observed. From this region we extracted regional β-amyloid plaque-load and iron-load to investigate local interactions. Within the MCI subjects, a significant correlation was observed between both neuroimaging markers, indicating a co-localization of both pathologies within this region. MCI carriers of the Apolipoprotein E ε4 (APOE4) genetic risk factor showed both higher β-amyloid plaque-load and iron-load compared to cognitively healthy subjects, which only had increased β-amyloid plaque-load compared to non-carriers.

In the second study we investigated a sample of 44 cognitively healthy oldest-old: healthy adults of 85 years and older without signs of cognitive decline. This study was performed on the 3T PET-MRI to investigate markers of resistance to aging associated cognitive decline by comparing the oldest-old to 36 cognitively healthy younger-old (aged 55-80) participants. Despite having significantly higher β-amyloid plaque-load,

atrophy and indicators of small vessel cerebrovascular disease the oldest-old only had slightly lower cognitive performance compared to younger-old. However, cortical iron-load was significantly lower in the oldest-old and entorhinal cortex volume positively correlated with β-amyloid plaque-load.

In the final study a large sample of 116 cognitively healthy elderly were scanned on the 3T PET-MRI for simultaneous measurement of iron-load and β-amyloid plaque-load. This setup is the best possible input for voxel-to-voxel correlation analysis using Biological Parametric Mapping (BPM) of iron-load and β-amyloid plaque-load. We found a bilateral pattern of strong correlations throughout the brain, most notably in the basal ganglia and frontotemporal cortex. No relationship between global β-amyloid burden and cognitive performance was observable in this cognitively healthy sample. For two bilateral clusters, located in the frontotemporal cortex, significant relationships between local β-amyloid and cognitive performance could be observed. No specific links to APOE4-carrier status was observable in the correlations or in the relationships of the correlations to cognitive performance.

Taken together, in this work we have shown that neuroimaging markers of iron-load and β-amyloid plaque-load correlate in cognitively healthy and impaired older adults. Additionally, we showed effects of iron-load on brain functioning and relationships between APOE4 and iron-load. By investigating both MCI subjects and, in a separate study, healthy oldest-old subjects, we showed effects of altered iron-loading on cognitive performance. These findings support hypotheses of iron dyshomeostasis contributing to AD pathology. However, as neuroimaging studies are limited to their acquisition resolution, further studies are required to determine the exact location of the iron within the diseased system and to investigate longitudinally changes.

3 Zusammenfassung

Die Alzheimerkrankheit ist eine neurodegenerative Erkrankung, die Gedächtnisverlust bewirkt und und zur häufigsten Form von Demenz führt. Ihr pathologisches Hauptmerkmal ist das Protein β-Amyloid in seiner löslichen und aggregierten Form: die Amyloid-Hypothese. Obwohl innerhalb von Personen und auf Gruppenebene das Ausmass an β-Amyloid-Plaques stark mit kognitivem Abbau korreliert, gibt es zahlreiche Erwachsene mit klinisch nicht feststellbarer Alzheimerpathologie. Diese älteren Erwachsenen haben signifikante Ansammlungen von β-Amyloid-Plaques aber legen keinen kognitiven Abbau an den Tag, oder erst in sehr viel späteren Stadien. Das Stattfinden einiger neuropathologischer Veränderungen wurde in Gehirnen von Erkrankten gezeigt, darunter Aggregation von pathologischem Tau, vaskuläre Schädigung und Neuroinflammation. In den letzten Jahren bestand Evidenz, dass Eisen-Dyshomeostase den Effekt und das Fortschreiten von Neurodegeneration auf vielfältige Weise beeinflussen könnte. In drei Studien in der vorliegenden Arbeit haben wir Neuroimaging-Marker für β-Amyloid-Plaques, Eisen, vaskuläre Integrität und funktionelle Konnektivität verwendet, um mögliche Effekte der Eisenbelastung in Populationen kognitiv gesunder und leicht beeinträchtigter älterer Erwachsener zu explorieren. Insbesondere wurde quantitative Suszeptibilitätskartierung (Quantitative Susceptibility Mapping; QSM) sowohl für Ultra-Hochfeld-MRT bei 7T als auch für Hochfeld-MRT bei 3T implementiert, was in-vivo-Inferenzen zu kortikaler grauer Substanz erlaubte.

In der ersten Studie untersuchten wir eine Stichprobe von 37 Personen, wovon 15 eine leichte kognitive Beeinträchtigung (LKB) aufwiesen, mit 7T-MRT. Mithilfe von funktioneller Konnektivitätsanalyse fanden wir veränderte Gehirnfunktion in Personen mit höherer Eisenbelastung. Insbesondere im medialen Präfrontalkortex wurde signifikant erhöhte Konnektivität beobachtet. Von dieser Region extrahierten wir Belastungswerte für β-Amyloid-Plaques und Eisen, um lokale Interaktionen zu untersuchen. Innerhalb der Personen mit LKB wurde eine signifikante Korrelation zwischen diesen beiden Neuroimaging-Markern beobachtet, was auf eine Kolokalisation beider pathologischer Bürden innerhalb dieser Region hinweist. Träger des genetischen Risikofaktors Apolipoprotein E ε4 (APOE4) mit LKB zeigten höhere Belastungswerte für β-Amyloid-Plaques und Eisen verglichen mit kognitiv gesunden Trägern, welche nur erhöhte Werte für für β-Amyloid-Plaques hatten verglichen mit Nicht-Trägern.

In der zweiten Studie untersuchten wir eine Stichprobe von 44 kognitiv gesunden ältesten Alten: Personen im Alter von 85 und mehr Jahren ohne Anzeichen kognitiven Abbaus. Diese Studie wurde mit dem 3T-PET-MRT-Gerät durchgeführt, um Marker für Resistenz gegenüber altersbedingtem kognitivem Abbau zu untersuchen, wofür die ältesten Alten mit 36 kognitiv gesunden jüngeren Alten (im Alter von 55-80) verglichen wurden. Die kortikale Eisenbelastung war jedoch signifikant niedriger in den ältesten Alten und das Volumen des entorhinalen Kortex korrelierte positiv mit β-Amyloid-Plaque-Belastung.

In der letzten Studie wurde eine grosse Stichprobe (N=116) kognitiv gesunder Älterer mit dem 3T-PET-MRI-Gerät gescannt zur simultanen Messung von Eisen- und mit β-Amyloid-Plaque-Belastung. Diese Konfiguration ist die Bestmögliche für die Voxel-zu-Voxel-Korrelationsanalyse mithilfe von biologischer parametrischer Kartierung (Biological Parametric Mapping; BPM) von Eisen- und β-Amyloid-Plaque-Belastung. Wir fanden ein bilaterales Muster starker Korrelationen über das gesamte Gehirn hinweg mit Höchstwerten in den Basalganglien und frontotempralem Kortex. Keine Beziehung konnte zwischen globaler β-Amyloid-Plaque-Belastung und kognitiver Leistung gezeigt werden in dieser kognitiv gesunden Stichprobe. Für zwei bilaterale Cluster, lokalisiert im frontotemporalen Kortex, konnten signifikante Zusammenhänge zwischen lokalem β-Amyloid und kognitiver Leistung beobachtet werden. Keine spezifischen Verbindungen zu APOE4-Trägerstatus waren beobachtbar in den Korrelationen oder Beziehungen der Korrelationen zu kognitiver Leistung.

Zusammengenommen haben wir in der vorliegenden Arbeit gezeigt, dass Neuroimaging-Marker von Eisen- und β-Amyloid-Plaque-Belastung in kognitiv gesunden und beeinträchtigten älteren Erwachsenen korrelieren. Zusätzlich haben wir Effekte von Eisenbelastung auf Hirnfunktion und Beziehungen zwischen APOE4 und Eisenbelastung gezeigt. Durch das Untersuchen von sowohl Personen mit LKB als auch, in einer separaten Studie, gesunden ältesten Alten, zeigten wir Effekte veränderter Eisenbelastung auf kognitive Leistung. Diese Befunde unterstützen Hypothesen eines Beitragens von Eisen-Dyshomeostase zur Pathologie der Alzheimerkrankheit. Da jedoch Neuroimaging-Studien durch die Auflösung ihrer Aufnahmen limitiert sind, werden weitere Studien gebraucht, um die exakte Lokalisierung des Eisens innerhalb des erkrankten Systems sowie deren potenzielle longitudinale Veränderungen zu untersuchen.

4 Introduction

4.1 Alzheimer’s Disease

Alzheimer’s disease (AD) is a neurogenerative disease that leads to memory loss and is the most common form of dementia. In the United States, AD is the sixth leading cause of death and while since 2000 the number of deaths from heart disease have decreased by 14%, the number of deaths due to AD has increased by 69% (Association 2017). There are two main forms of AD: early-onset or familial-AD originating from genetic mutations, that accounts for a small number of the total number of AD cases, and sporadic-AD, occurring in adults over 65 years of age due to decades of pathological accumulations. Currently, one in nine people age 65 and older (1%) and one third (32%) of people aged 85 and older has AD (Association 2017). While there is no medication that can stop the progression of AD related neurodegeneration at present, recent developments of potential drugs in clinical trials (Patel 2015; Selkoe and Hardy 2016; Sevigny et al. 2016) raises the hope that in the near future AD progression can be halted.

AD is often confused with normal aging and dementia. Severe memory loss, characteristic of AD, is not a symptom of normal aging. It is common to have slower recall of information at higher age, however, cognitive decline that impacts daily life is not a normal part of the aging process. Dementia is defined as the significant loss of cognitive abilities severe enough to interfere with social functioning (McKhann et al. 2011). There are many diseases that can lead to neurodegeneration and cognitive decline that could be classified as dementia. As such AD can lead to dementia and it accounts for 60-80% of dementia cases (Association 2017). Other major causes of dementia are vascular dementia, dementia with Lewy bodies and frontotemporal lobar degeneration. These types of dementia have overlapping features with AD dementia and can be identified using neuroimaging such as magnetic resonance imaging (MRI) and positron emission tomography (PET) or using cerebral spinal fluid (CSF) biomarkers.

4.1.1 Amyloid-β (Aβ) pathology

The main antagonist in AD has long been identified to be the amyloid-β (Aβ) protein in its soluble and aggregated forms, refered to as the amyloid-hypothesis (Selkoe and Hardy 2016). Aβ originates from proteolytic processing of the amyloid precursor protein (APP). APP itself has been implicated in a vast number of neuronal processes (van der Kant and Goldstein 2015), in particular, APP seems to be involved in intracellular signaling pathways supporting axonal growth, dendritic process and synaptic maintenance. The normal regulated proteolysis of APP into its fragments regulate intracellular trafficking as well as neuronal migration in early embryogenesis. Additionally, APP and its fragments respond to cellular damaged or changes in neuronal activity by controlling cholesterol homeostasis, delivery of vesicular carriers, cellular growth and proliferation (van der Kant and Goldstein 2015).

The proteolysis of APP can be amyloidogenic (resulting in generation of Aβ) or anti-amyloidogenic (preventing Aβ generation) depending on the specific extracellular cleavage. In the anti-amyloidogenic pathway, APP is cleaved by α-secretase in the APP-extracellular Aβ domain, resulting in a fragment that lacks the amino-terminal of the Aβ domain. However, in the amyloidogenic pathway β-secretase cleaves a shorter fragment, leaving the Aβ domain. In both pathways, the final step is an intra-membrane cut by γ-secretase, resulting in Aβ (amyloidogenic) or the seemingly harmless p3 fragment (anti-amyloidogenic) respectively. The remaining amyloid intercellular domain (AICD) is taken up by the cytoplasm. Aβ is produced in this way mostly in neurons in varying lengths, where Aβ40 is the most abundant and Aβ42 the most aggregation prone (Masters and Selkoe 2012).

The formation of insoluble β-amyloid plaques from Aβ monomers occurs through the formation of misfolded globules, followed by oligomers, β-sheet intermediates and protofibrils (Lee et al. 2011) (**Figure 1** and **Figure 3**). In the initial development of plaques the different stages are in equilibrium and can transition among each other (Serrano-Pozo et al. 2011). This initial development is followed by a secondary stage in which the polymerization of Aβ into fibrils and β-amyloid plaques is accelerated. This process is visualized in the chapter *Iron in Alzheimer's Disease*.

While not in the focus of this work, the other main pathological marker of AD is presence of neurofibrillary tangles (NFT) within neurons (Mandelkow and Mandelkow 2012). NFTs are the resultant of tau protein aggregation, which in its normal function is mainly responsible for stability and reorganization of microtubules within the cell. Tau protein aggregation follows a distinct pattern that is different from the spread of β-amyloid plaques. In general, tau pathology follows after the formation of β-amyloid plaques. While NFT can be viewed as a downstream effect of Aβ pathology due to phosphorylation of Tau, it has also been suggested as being a necessary step for Aβ-induced-toxicity (Morris et al. 2011). Pathological example slices with staining for both plaques and NFT are shown below (**Figure 1**).

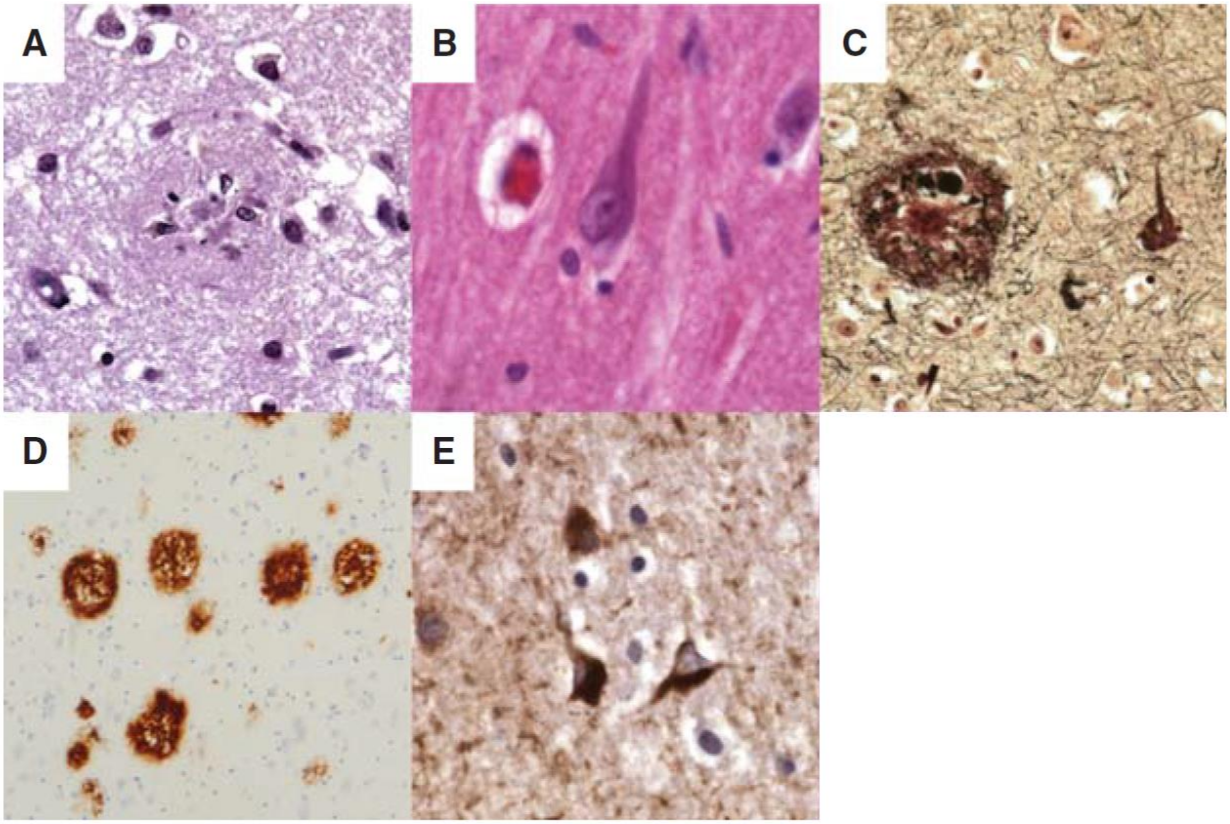

Figure 1: *Adapted from (Serrano-Pozo et al. 2011). Core pathological lesions observed in AD. (A) Plaque evident on routine H&E stained section of frontal cortex; (B) tangle in a hippocampal pyramidal neuron; (C) silver stain highlights both a plaque and a tangle; (D) immunohistochemistry against Ab highlights plaques; (E) immunohistochemistry against tau highlights tangles.*

The presence of Aβ oligomers and β-amyloid plaque build-up leads to several downstream pathologies such as neuroinflammation, dystrophic neurites, axonal loss and eventually neuronal loss (Benilova, Karran, and De Strooper 2012; Mucke and Selkoe 2012; Serrano-Pozo et al. 2011; Sperling et al. 2011; Serrano-Pozo et al. 2016; Jagust et al. 2009; Dubois et al. 2016). This process happens over decades in the case of late-onset AD, making age one of the biggest risk factors for AD. At this point it is not yet clear if the β-amyloid plaques or the Aβ oligomers are largest source of neuronal damage and downstream pathologies. In vivo measures of β-amyloid plaques do relate strongly to risk for AD (Jansen et al. 2015; Pietrzak et al. 2015) and removal of the plaques was shown to nearly halt progressive cognitive decline (Sevigny et al. 2016). However, it is also suggested that AD neurodegeneration is due to Aβ oligomers released from the β-amyloid plaques and not due the plaques themselves (Benilova, Karran, and De Strooper 2012; Mucke and Selkoe 2012; Selkoe and Hardy 2016).

While every part in the Aβ related cascades and seemingly every part of the protein has been investigated, it is astonishing to realize that adults with AD only have approximately 4.8 mg more Aβ protein in their cortical gray matter compared to controls (Roberts et al. 2017).

4.1.2 Cerebral amyloid angiopathy (CAA)

Capillaries in the brain can be as small as 7–10 μm in diameter with an average intercapillary distance of about 40 μm (Duvernoy, Delon, and Vannson 1983). This small vasculature is affected by Aβ deposits in the vessel walls, in particular in the medium and small-sized arteries and cortical arterioles and this phenomena is known as cerebral amyloid angiopathy (CAA) (Dierksen et al. 2010; Holland et al. 2008; Weller et al. 1998). CAA is present in almost all AD subjects to a varying degree, with up to 25% suffering from advanced CAA (Ellis et al. 1996). However, CAA can also be present in the absence of AD-pathology, with up to 50% of cases not meeting AD pathological criteria (Ellis et al. 1996; Esiri et al. 2015; Weller et al. 1998). In contrast to the Aβ42 that mainly makes up the β-amyloid plaques in AD, it is Aβ40 that builds up in the media and adventitia of small vessel walls. The build-up of Aβ in the vessel walls can result in total loss of smooth muscle, collagen and elastic tissue (Esiri et al. 2015). These alterations impair the normal functioning of the vasculature and can result in microbleeds or local infarctions.

4.1.3 Apolipoprotein E4 (APOE4)

The most consistent and strongest genetic predisposition for late-onset AD has been observed for mutations in the Apolipoprotein E (APOE) gene (Farrer et al. 1997; Corder et al. 1993; Schmechel et al. 1993), with an increase in the risk of developing AD up to 30 times higher in carriers of two e4 alleles (APOE4) alleles (Farrer et al. 1997; Corder et al. 1993; Schmechel et al. 1993).

While the exact link between APOE4 and AD is not clear, APOE is a protein normally involved in formation of lipoproteins which are responsible for transport of cholesterol and other fatty acids in the bloodstream and the brain. However, in the literature various links have been made between AD and APOE4 or other APOE variants (e2 and e3). Furthermore, databases set up to identify other genetic risk factors have revealed that many of the top results are genes related to inflammation, cholesterol metabolism, transport/trafficking proteins and neuronal signaling (Bertram et al. 2008).

4.1.4 Changes in brain functioning

Changes in functioning of the brain can be measured by resting-state functional MRI (rs-fMRI), revealing functional connectivity between brain regions based on inferences of their synchronized neuronal activity. The theory, measurement and analysis of rs-fMRI is explained in the *Methods* section of this work. With rs-fMRI, almost all the stages of AD progression starting from onset of clinical symptoms have been analyzed. The findings in AD and mild cognitive impairment (MCI) have been consistent across several studies. Using network analysis in a large sample of cognitively normal, MCI and AD subjects, loss of intra-network connectivity was shown in large networks including the default mode network (DMN), salience network, dorsal attention network, control network and sensory motor network (Brier et al. 2012). Additionally, the strength of between-network connectivity decreased between MCI and AD, indicating reduced coherence of brain activity. Much of research focus has been on the DMN, which is active at rest but has decreased activity during cognitive tasks. The DMN comprises the posterior cingulate cortex, medial prefrontal cortex, lateral temporal and parietal cortices, and hippocampus (Agosta et al. 2012). In the DMN, activity decreases with progression of AD and is even affected in subjects with higher β-amyloid plaque-load that do not (yet) experience cognitive decline (Sheline et al. 2010). The regions of the DMN are also the regions earliest involved in abnormal β-amyloid plaque depositions (Braak and Braak 1991), which is also suggestive of β-amyloid spreading along functionally connected regions (Seeley et al. 2007; Seeley et al. 2009). Other task-based fMRI studies have shown that the ability to downregulate the DMN during cognitive task is positivity correlated with memory performance (Hamalainen et al. 2007). Therefore, changes in DMN activity, in particular increases, are often investigated in relation to potential biomarkers.

4.2 Iron in Alzheimer's Disease

4.2.1 Iron: helpful and harmful

Iron has been used by the earliest known organisms that existed on earth (Coby et al. 2011) and iron-phosphide meteorites have been linked to the origins of life on earth (Pasek and Lauretta 2005). In the human body, iron is used for redox reactions and the majority (70%) is bound to hemoglobin within the red blood cells. In the brain, iron is the most abundant transition metal and essential for synthesis of neurotransmitters such as dopamine ATP (Lill and Muhlenhoff 2006; Meiser, Weindl, and Hiller 2013; Sun, Pham, and Waite 2016) and for myelination (Ortiz et al. 2004). Iron transport in the human body is facilitated by the transferrin protein, which can carry two iron ions each. The uptake of iron by the brain is regulated by transferrin receptor 1 and divalent metal transporter 1 which are highly expressed on arterial endothelial cells. Trafficking of iron into the brain is further tightly controlled by the blood-brain-barrier and in the mature brain the exchange is limited compared to other organs (Moos et al. 2007). While iron is essential for normal functioning, if left unbound, Fe^{2+} can take part in a Fenton-reaction and Haber-Wiess chemistry (Koppenol 2001) in which reactive oxygen species (ROS) are created that can result in cellular damage and accelerate cellular aging (Harman 1956; Winterbourn 1995; Dixon et al. 2012; Dixon and Stockwell 2014) (**Figure 2**). ROS have been shown to impair cellular growth and to be a source of apoptosis (ferroptosis) by reacting with essential amino acids, lipid peroxidation and instigating DNA damage (Dixon et al. 2012; Dixon and Stockwell 2014). During normal brain functioning, excess iron is stored inside the ferritin protein, which can hold up to 4500 iron atoms (Harrison and Arosio 1996). This is further described in the chapter *Magnetic susceptibility* (**Figure 5**).

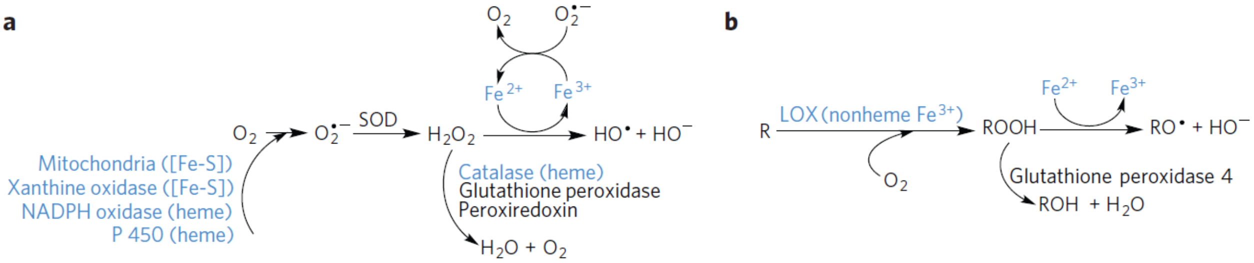

Figure 2: *Adapted from (Dixon et al. 2012). Pathways of formation of select soluble (a) and lipid (b) ROS via Fenton chemistry. Key enzymes that contribute to ROS formation or detoxification are shown. Those whose function is iron dependent are colored blue, and the relevant iron species is in parentheses. SOD = superoxide dismutase, LOX = lipoxygenase.*

4.2.2 Iron and Aβ

The interest in iron in a context of AD originates from histopathological findings of increased iron deposits in brains of AD subjects and specifically around β-amyloid plaques (Andersen, Johnsen, and Moos 2014; Meadowcroft et al. 2009; Rottkamp et al. 2001). While copper and zinc also play an important role in brain functioning and have been linked to AD (Bush 2013; Squitti 2012), their concentrations in the human brain are significantly lower than those of iron (Deibel, Ehmann, and Markesbery 1996).

Aβ in its monomeric and aggregated forms can bind iron, converting Fe^{3+} into Fe^{2+} (Khan, Dobson, and Exley 2006). While Fe^{3+} can bind to all forms of Aβ, it has difficulty dissociating from the fibrillar forms, resulting in aggregation of iron inside and on the border of the plaques (Everett et al. 2014; Derry and Kent 2017; Peters, Connor, and Meadowcroft 2015) (**Figure 3**). Iron associated with β-amyloid plaques has been commonly observed and could be a potential source of the oxidative damage due to ROS observable in AD brains (Nunomura et al. 2001; Andersen, Johnsen, and Moos 2014; Meadowcroft et al. 2009; Rottkamp et al. 2001; Derry and Kent 2017). The ROS rich halo around plaque-bound iron can trigger ferroptosis (Dixon et al. 2012) and promote production of Aβ monomers due to increased β-secretase cleavage (Zhang et al. 2007) in the cells surrounding the β-amyloid plaques. Additionally, Aβ-bound iron accelerates the extent and speed of aggregation from Aβ monomers into β-amyloid plaques (Peters, Connor, and Meadowcroft 2015; Everett et al. 2014; Acosta-Cabronero et al. 2013; Ha, Ryu, and Park 2007). Subsequent white matter damage is also a frequent finding in AD. As white matter contains relatively large amounts of iron the degeneration of white matter occurring during development of AD can be a continuous source of iron-loading (Agosta et al. 2011).

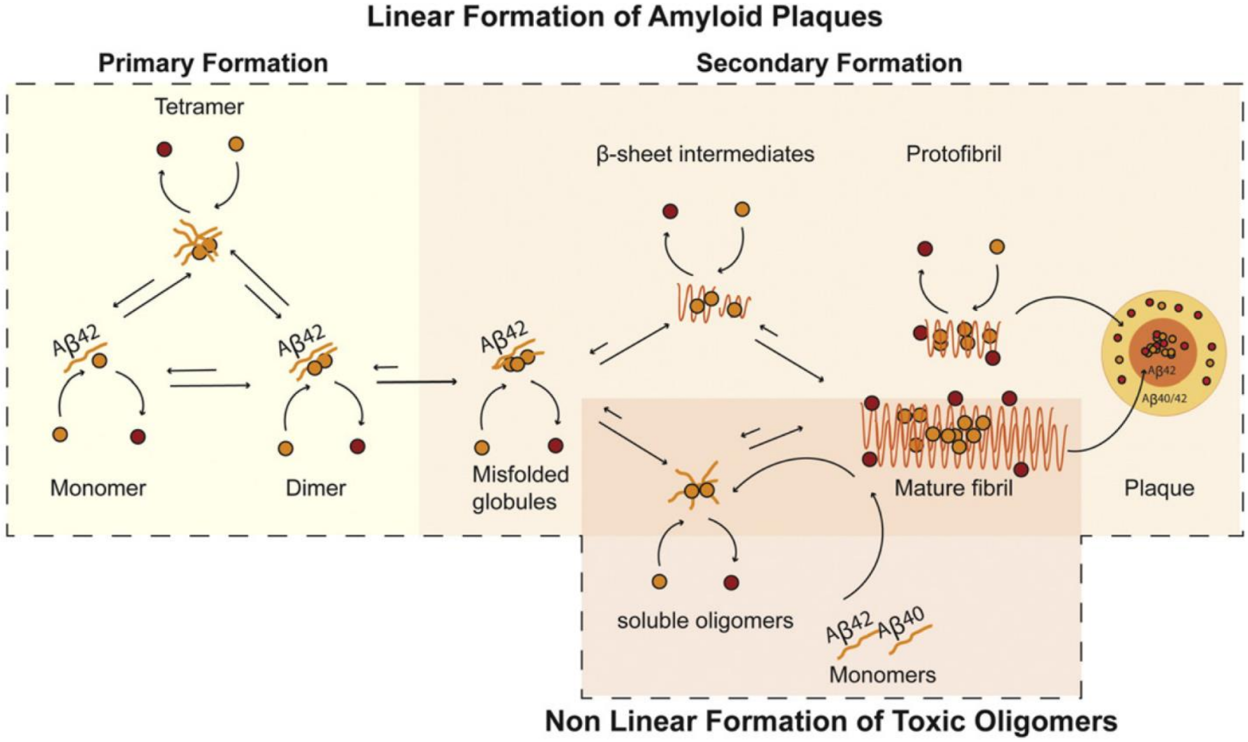

Figure 3: *Image adapted from (Peters, Connor, and Meadowcroft 2015). The formation of β-amyloid plaques and the incorporation of iron. B-amyloid plaque formation can be characterized by primary and secondary aggregation. During primary formation, ferric iron interacts with Aβ as it fluctuates between monomer, dimer, and tetramer formations. Iron–amyloid interactions increase ferrous iron, which can lead to the production of reactive oxygen species. Eventually, β-sheet intermediates and toxic soluble oligomers are formed from which the iron no longer can dissociate easily. Iron gets incorporated in the mature stable plaques and in the defuse halo around the plaques.*

ROS detection and removal mechanisms are present in healthy neuronal cells. In particular nuclear factor E2-related factor 2 (Nrf2) regulates the antioxidant response pathway that can buffer and degrade ROS. In an AD mouse model transcription of Nrf2 was shown to be reduced (Mladenka et al. 2006) while overexpression of Nrf2 lead to increased spatial memory (Caldeira, Ferreira, and Rego 2013). Part of the response to ROS is the antioxidant glutathione which is produced primarily in astrocytes and microglia. However, in human AD brains both cell types have been shown throughout the cortex to have reduced production of glutathione (Karelson et al. 2001). Both findings are indicative of reduced protection against iron-induced ROS in AD, resulting in increased neuropathological burden.

There has also been evidence that APOE4 might play a role in iron homeostasis, as ferritin levels in the CSF predicted progression from MCI to AD in a large cohort and this effect was modulated significantly by APOE4 status (Ayton et al. 2015). The exact mechanism is not clear and, therefore, it was hypothesized that APOE functions to lower neuronal iron as APOE knockout mice exhibit elevated brain iron (Bush 2013; Bush et al. 2014). In a later study it was found that while controlling for APOE4-status, high CSF ferritin levels was predictive for increased brain β-amyloid plaque-loading in subjects with higher baseline levels of Aβ42 (Ayton, Diouf, and Bush 2017).

However, investigating iron in a context of AD is complicated by the β-amyloid plaque-formation in transgenic mice models not completely mimicking the formation in human AD. Specifically, the β-amyloid plaques found in animal models exhibit opposite iron characteristics compared to human AD histology: no presence of focal iron and reduced free iron around the plaques due to iron binding to Aβ (Meadowcroft et al. 2009). Animal models more closely replicating the iron patterns found in humans are currently still under development.

The pathological work by Hallgren and Sourander and recent MRI-based work (Hallgren and Sourander 1958; Langkammer et al. 2012; Lim et al. 2013; Betts et al. 2016) have shown that brain iron-levels increase strongly in the first decades of life followed by stabilization around the age of 40. After this age variability in iron-levels strongly increase, which coincides with the assumed start of Aβ accumulation (Hallgren and Sourander 1958; Langkammer et al. 2012; Lim et al. 2013; Betts et al. 2016). Combined with findings of increased iron-loading in AD subjects (Nunomura et al. 2001; Andersen, Johnsen, and Moos 2014; Meadowcroft et al. 2009; Rottkamp et al. 2001; Derry and Kent 2017) these are indications that iron dyshomeostasis plays a central role in development of AD.

4.2.3 Iron modification therapies in AD

In animal models, the iron chelator Deferoxamine was shown to decrease tau phosphorylation, slow down aggregation of β-amyloid plaques and reduce behavioral impairment (Guo, Wang, Zhong, et al. 2013; Guo, Wang, Zheng, et al. 2013). This approach was followed by a 24-month trial in AD subjects that showed behavioral improvements (Crapper McLachlan et al. 1991). However, there was no follow-up to this study and with current knowledge effects of chelation therapy are hypothesized to be only effective when administered in much earlier, asymptomatic, stages of life (Malecki and Connor 2002).

5 Hypotheses

The information summarized previously has brought us to the following hypotheses that will be investigated in this work:

1. Iron accumulation in human brains co-localizes with β-amyloid plaques in healthy and pre-clinical Alzheimer's disease subjects independent from iron accumulations due to microbleeds.
2. Iron accumulation co-localized with β-amyloid plaques in human brains negatively affects cognitive performance in healthy and pre-clinical Alzheimer's disease subjects.
3. Iron accumulation in human brains correlates with changes in functional connectivity between brain regions measured by fMRI.
4. APOE-e4 genotype is associated with high β-amyloid plaque related iron accumulation.

The main chapters will be presented in the order that the research was conducted, which is slightly different from the order of the hypotheses.

6 Methods

6.1 β-amyloid PET

One of the revolutions in the field of AD-diagnostics has been the development of PET tracers to measure β-amyloid in vivo. Until as recent as 10 years ago pathological hallmarks of AD could only be evaluated post-mortem (Mathis et al. 2012). The instigator of the current state of β-amyloid-plaque-PET was the development of the 11C-Pittsburgh Compound B (PiB) tracer. PiB is based on the Thioflavin-T, a small molecule used as a fluorescent dye for histological staining of protein aggregates such as β-amyloid plaques. Studies have shown that, as expected, PiB mostly binds to fibrillar β-amyloid such as those in plaques but also to vascular deposits due to CAA (Johnson et al. 2007). However, there is also strong non-specific white matter binding, requiring the need to mask out the gray matter for analysis.

In order to overcome the limitation of 11C PET-tracers such as the short half-life and thus requirement of a production center close to the PET-scanner, 18F versions of PiB have been developed. The analogue 18F-Flutemetamol is used in this work (**Figure 4**). It has similar characteristics as PiB with respect to β-amyloid plaque binding but also suffers from increased non-specific white matter binding, despite the only minute change in the chemical structure (Vandenberghe et al. 2010). Both PiB and 18F-Flutemetamol do not bind to Aβ oligomers, limiting the in vivo investigations into the source of neurotoxicity of β-amyloid plaques and anti-Aβ therapy.

It should also be noted that the larger samples used in this study were acquired using a 3T GE Signa PET-MRI with very fast digital PET detectors. This allows for the use of time-of-flight reconstruction, which enables filtering of false-positive scattered counts resulting in significantly higher signal-to-noise ratios (Conti 2011).

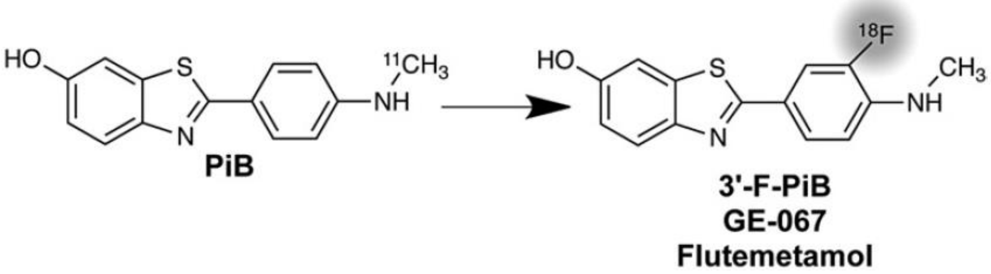

Figure 4: *Adapted from (Mathis et al. 2012), chemical modification of 11C-PiB to 18F-Flutemetamol,.*

6.2 Quantitative Susceptibility Mapping (QSM)

6.2.1 Magnetic susceptibility

Magnetic susceptibility (χ) is a dimensionless property of a material that indicates whether a material is magnetized when it is placed in an external magnetic field, it can also be referred to as “magnetizability” (Schenck 1996). When a material interacts with the magnetic field an internal magnetization (polarization) is created that either opposes or amplifies the external field. If the magnetization opposes the external field, the material is diamagnetic. If the magnetization is amplified, the material is paramagnetic, superparamagnetic, or ferromagnetic, depending on the strength of the amplification. Examples of this in human tissues are fat (χ=-10, diamagnetic), organic free radicals (χ=+1, paramagnetic), ferritin, hemosiderin (χ=+5000, superparamagnetic) and pure iron (χ=+10000, ferromagnetic). Measuring magnetic susceptibility using MRI was envisioned at the early days of MRI (Young et al. 1987) but only recent developments in methodology and computer processing power have made it feasible to circumvent the problems involved in this type of reconstruction.

An overview of biomedical magnetic materials that can be found in the human brain is given below, adapted from (Wang and Liu 2015) (**Figure 5**). The main sources of susceptibility contrast in the human brain are Fe^{3+} in various bound and unbound states and the myelin in the white matter. However, it is known from the Maxwell Equations for static magnetism that the strong susceptibility induced fields occur near the susceptibility edges perpendicular to the main magnetic field B_0 (Li et al. 2012). This results in orientation dependent changes to the measured susceptibility signal in myelin. In addition to this, the susceptibility itself is anisotropic in myelin due to molecular anisotropy of lipid and the microstructure (**Figure 5**). Therefore, when investigating iron sources in the brain the regions of interest are limited to the gray matter. When interpreting the susceptibility data of gray matter regions it needs to be considered that the iron-load could vary on an inter-voxel basis and that QSM is biased by decreased myelin density (Langkammer et al. 2012; Liu, Li, et al. 2011). However, the cortical and deep gray matter regions investigated in the context of AD are low in myelin content and thus the myelin contribution is usually considered negligible.

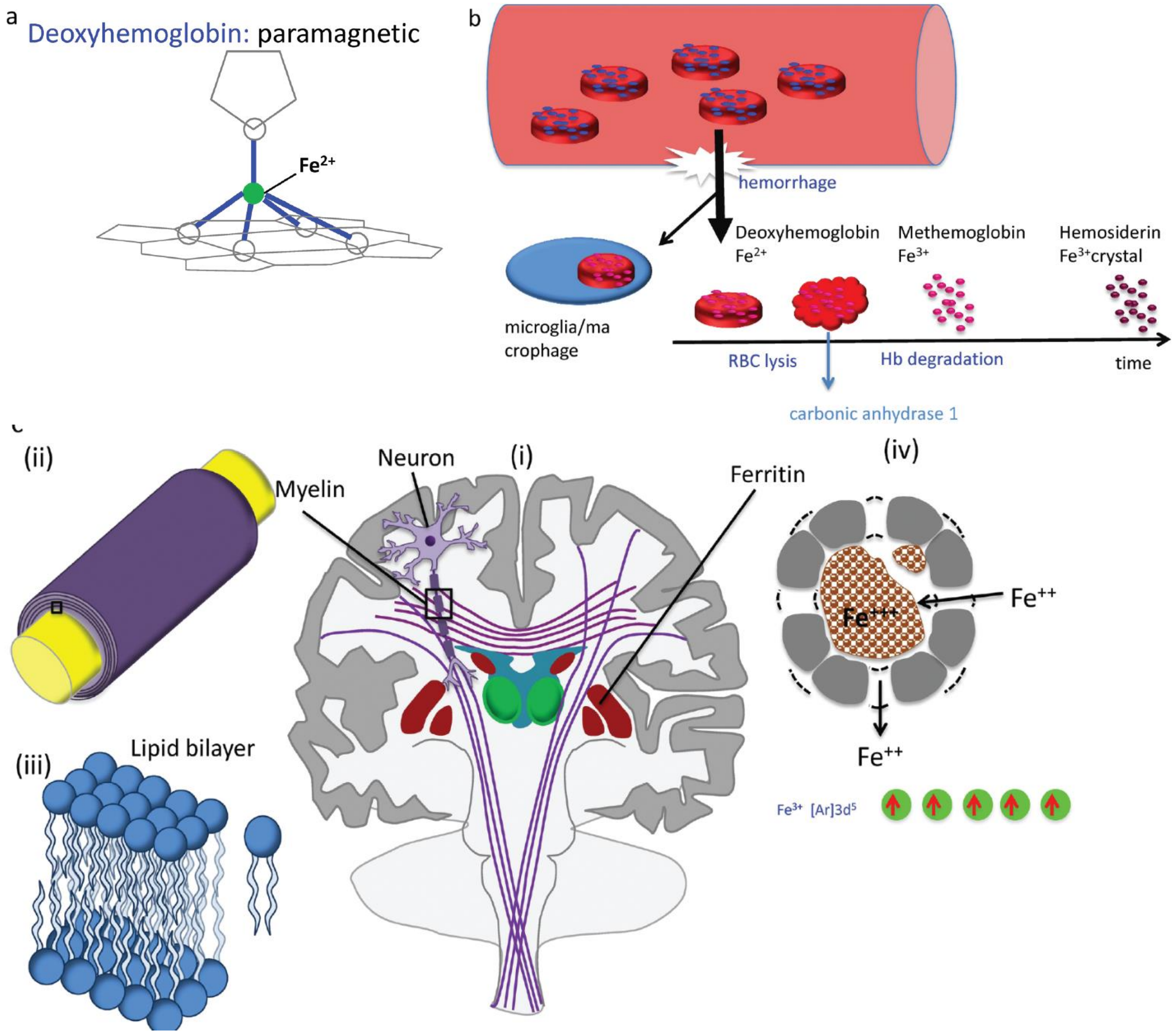

Figure 5: *Biomedical magnetic materials. Adapted from (Wang and Liu 2015). (a) During metabolic consumption of oxygen, weakly diamagnetic oxyhemoglobin releases* O_2 *and becomes strongly paramagnetic deoxyhemoglobin. (b) Blood degradation in hemorrhage. Following a hemorrhage, a small fraction of red blood cells (RBCs) may be endocytosed by microglia/macrophages. The majority of RBCs undergo cell lysis and hemoglobin (Hb) degradation from deoxyhemoglobin into methemoglobin (*Fe^{3+}*) and hemosiderin (possible magnetic domain). Modeled after: (Keep, Hua, and Xi 2012). (c) Susceptibility sources in the human brain. Major susceptibility sources in (i) the brain include myelin and ferritin. The white matter tracts in the brain consist of myelinated nerve fibers. (ii) Zoomed view of the box in (i) showing axon (yellow) and myelin sheath (purple). Myelin consists of several layers of lipid bilayer. (iii) Zoomed view of the box in (ii) showing a lipid bilayer and an individual lipid. (iv) Ferritin in a cross-section. Ferritin consists of a peptide spherical shell 2-nm thick with an 8-nm diameter cavity.* Fe^{2+} *enters through a four-fold symmetric channel, is stored as* Fe^{3+} *oxide mineral, and is released as* Fe^{2+} *through a three-fold symmetric channel. There are five unpaired 3d electrons in* Fe^{3+}*, generating strong paramagnetism.*

6.2.2 Measuring magnetic susceptibility using MRI

Amplification of the local magnetic field due to a materials' magnetic susceptibility adds phase accumulation to the protons within a measured voxel, causing dephasing or magnitude decay in T2*-weighted MRI. In particular Gradient Echo (GRE) MRI is sensitive to this type of contrast, which can be used in susceptibility-weighted imaging (SWI). This type of imaging is non-quantitative because the signal at the local tissue is affected by all susceptibility sources around it (**Figure 6**).

The effect of the susceptibility sources on the frequency map δB in any point in space can be described by the convolution of the dipole kernel with the surrounding susceptibility distribution χ (Jackson 1975):

$$\delta B(r) = \int_{r' \neq r} \chi(r') \frac{3cos^2(\theta_{r-r'}) - 1}{4\pi|r' - r|^3} d^3r' = \frac{3cos^2(\theta_r) - 1}{4\pi r^3} \otimes \chi(r)$$

Where δ are the normalized field shifts, r and r' are the locations of the observed field and the susceptibility source, and θ_r is the angle between B_0 and the vector $r - r'$. For every point in space the field shift is a convolution of the susceptibility distribution with the unit magnetic dipole kernel $(3cos^2(\theta_r) - 1)/4\pi r^3$.

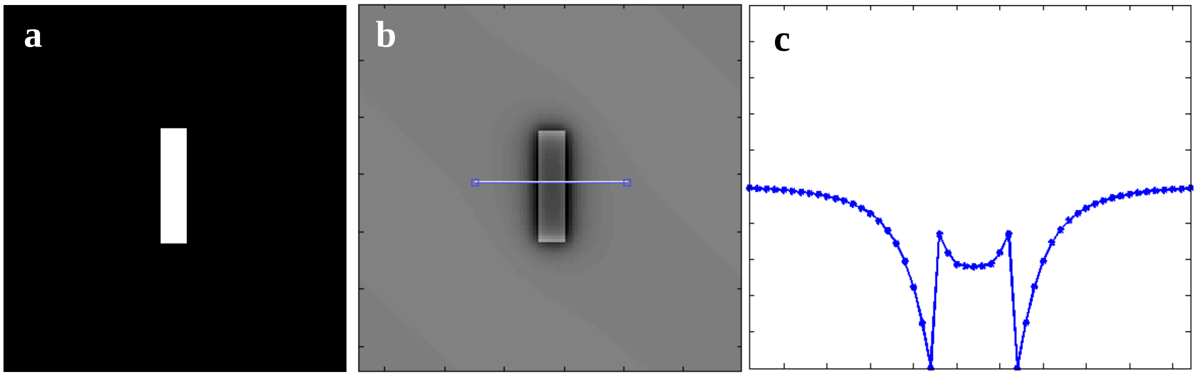

Figure 6: *Example of the magnetic susceptibility convolution effect: (a) bar with constant susceptibility in a region with zero susceptibility. (b) Simulation of the resulting frequency map δB for the bar in (a). (c) Cross-section of the measured frequency map at the location indicated in (b).*

The convolution becomes a multiplication in the Fourier domain:

$$F(\delta) = F(\chi)\left(\frac{1}{3} - \frac{k_z^2}{|\boldsymbol{k}|^2}\right) = F(\chi)D(\boldsymbol{k})$$

With F the Fourier transform and $D(\boldsymbol{k}) = \frac{1}{3} - k_z^2/|\boldsymbol{k}|^2$, the Fourier transformed dipole kernel. This shows that resolving the underlying χ from the measured δ is an ill-posed problem, meaning that the solution is not stable in all regions. Due to the term $\frac{1}{3} - k_z^2/|\boldsymbol{k}|^2$ the de-convolution is not defined when the $\boldsymbol{k}$-vector and the field direction is equal to 54.7° or 125.3°. On this conical surface in the Fourier domain the solution goes to infinity and there is high amplification of any noise for values on or near these cones. On the reconstructed image this results in streaking artifacts originating from areas with high susceptibility.

This can be solved by oversampling the data: the direction of the susceptibility effect is dependent on the orientation of the source relative to the magnetic field B_0. When the subject's head is rotated relative to the magnetic field, the cone of undefined values is also rotated in the Fourier domain. Undefined regions of one orientation can then be restored by information from the other orientations (Liu et al. 2009). With respect to the head-angle θ and ϕ the dipole kernel can then be rewritten:

$$D_{multi}(\boldsymbol{k}, \theta, \phi) = \left(\frac{1}{3} - \frac{(k_z \cos\theta \cos\phi - k_y \sin\theta \cos\phi + k_x \sin\phi)^2}{|\boldsymbol{k}|^2}\right)$$

It is possible to fully reconstruct the susceptibility map with 3 orientations since any of the regions of the 3 cones is described by well-defined data from one of the other orientations. This method is called Calculation of susceptibility through multiple orientation sampling (COSMOS). In a clinical setting this approach would be highly unpractical since a great number of patients would not be physically able to rotate their head in the scanner. Therefore, new methods were developed to be able to reconstruct the susceptibility with only 1 head orientation that use other information to reconstruct the QSM map.

In the following sections the specific processing steps and methodology required will be described.

6.2.3 QSM reconstruction: phase unwrapping

To use the underlying phase data the phase wraps have to be removed. Phase wraps occurs because the phase data is wrapped around 2π resulting in a phase image as shown in the example image (**Figure 7**). To perform susceptibility calculations this phase wrapping must be removed. This is done in the Fourier domain with Laplacian based phase unwrapping by (Li, Wu, and Liu 2011). The method involves applying a Laplacian operator to the phase image that only uses the trigonometric functions of the phase. The Laplacian operator is not only insensitive to phase wraps, but also automatically removes part of the phase components originating from outside of the Field of View (FOV), since they satisfy the Laplacian equation $\nabla^2\theta = 0$. This unwrapping is performed for each echo time (TE).

When the phase is unwrapped the frequency shift can be found by least squares fitting of the linear slope of the phase θ as a function of the TE in the first echoes for each image voxel. The magnetic field shift is related to the frequency shift in Hz as $\Delta f = \gamma \Delta B_z / 2\pi$. The relative magnetic field shift in ppm can then be found by dividing the frequency shift in Hz by the scanner frequency.

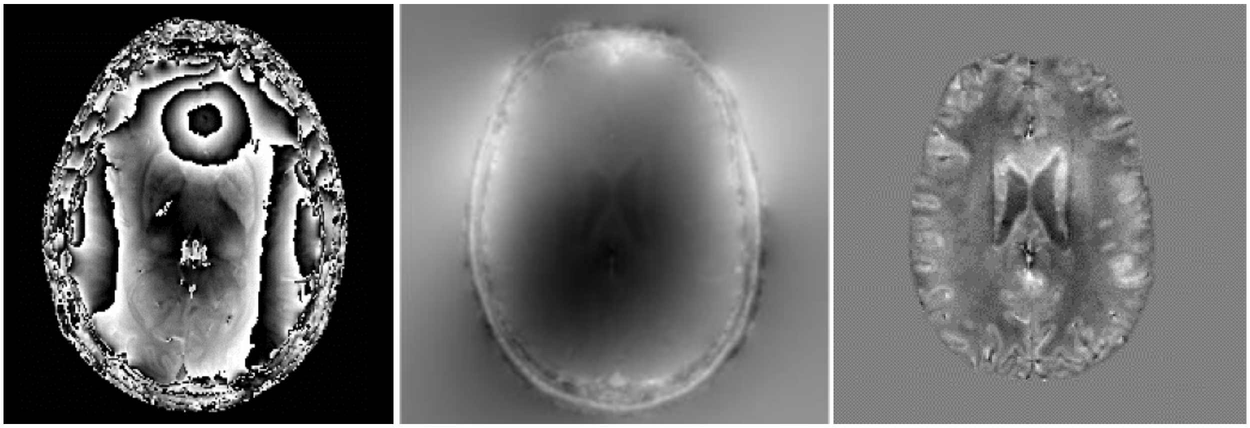

Figure 7: *From left to right: 1) Raw phase data from the scanner is wrapped around 2π. 2) Unwrapping using Laplacian based phase unwrapping results in continuous phase information. 3) Resulting image after background-field removal.*

6.2.4 QSM reconstruction: background-field removal

After phase unwrapping there are still clear slow varying phase effects present in the images. These are caused by the air-tissue interfaces and are an order of magnitude larger than the phase variations caused by local susceptibility differences. Multiple methods are developed to remove these effects without removing the variations due to the tissue susceptibility. The most commonly used method is the Sophisticated harmonic artifact reduction for phase data (SHARP) (Schweser et al. 2011) approach. This method uses inherent properties of the magnetic field changes both inside and outside of the brain (**Figure 7**).

In SHARP we define the total susceptibility sources inside and outside the brain as $B_{tot} = B_{int} + B_{ext}$. Because the magnetic field changes outside the brain (B_{ext}) result from sources that are located outside the brain, it is harmonic throughout the entire brain, therefore it satisfies Laplace's equation throughout the brain itself: $\nabla^2 B_{ext} = 0$. The field changes inside the brain (B_{int}) have their sources inside the brain they are inherently not harmonic. Using these properties the B_{int} can be calculated from the total sum of sources by solving:

$$\nabla^2 B_{tot} = \nabla^2 B_{int}$$

This equation can be solved by using the mean value property of harmonic function which stats that an underlying harmonic function is preserved when convolved with any nonnegative radially symmetric function that has a total volume of 1 (ρ). This can be rewritten with $\tilde{B}$ the underlying harmonic function of a magnetic field change as:

$$\tilde{B}_{tot} = B_{tot} - \rho \otimes B_{tot} = B_{int} - \rho \otimes B_{int}$$

$$B_{int} = (\delta - \rho) \otimes^{-1} \tilde{B}_{tot}$$

With δ the unit impulse at the center of the radial convolution kernel ρ. Due to size of the convolution kernel determines the extend to which pixels at the edge of the brain can be recovered. Smaller kernels result in fewer pixels lost at the edges of the brain but enforce less of the required spatial harmonicity. To overcome this problem smaller kernels are used near the edge of the brain while larger kernels are used in the center. This method is referred to as Variable spherical kernel SHARP (V-SHARP).

During processing described in the accumulated works, V-SHARP is applied using a variable spherical kernel size with a maximum radius of 4mm and a regularization parameter of 0.05 (Schweser et al. 2011; Wu, Li, Guidon, et al. 2012). A brain mask to determine the location of B_{int} and B_{ext} was obtained by skull-stripping the GRE magnitude image using FSL's brain extraction tool (BET, FMRIB Oxford, UK).

6.2.5 QSM reconstruction: dipole inversion

To solve the ill-posed problem at the heart of QSM it is possible to introduce a priori information to identify a meaningful solution. Results obtained via the multi-head-angle method COSMOS show that edge regions in the susceptibility image coincide with edges in the GRE magnitude images and regions with more constant susceptibility match more constant regions in the magnitude images. The edges showing streaking artifacts in the susceptibility images have artifacts that radiate away from tissue boundaries. This effect can be utilized to find the optimal solution by minimizing the voxels of the susceptibility gradient map that are not on the magnitude gradient map, thereby eliminating false gradients. The method is called Morphology-Enabled Dipole Inversion (MEDI), which is described as an L1 norm minimization, formulated by the following unconstrained Lagrangian problem:

$$\text{argmin}_{\chi} \|M \nabla \chi\|_1 + \lambda \|W(\delta - F^{-1} D F \chi)\|_2^2$$

where M is the binary gradient weighting matrix, in which the elements are 0 when they correspond to non-negligible gradients in the magnitude image. Non-negligible gradients are defined as gradients larger than μ, a constant that needs to be optimized manually. ∇ is the 3D gradient operator, λ the Lagrangian parameter that needs to be optimized, W a data weighting matrix to account for non-uniform phase noise and D the dipole kernel defined earlier. The Lagrangian parameter λ determines the relative weighting of the edge information in the minimization.

Simply put: this minimization will start with an almost empty "guess" of the underlying susceptibility $\check{\chi}$ and calculate which magnetic field fluctuations ($\check{B}_{int}$) would result from that distribution if an object was scanned like that. Then it compares this guessed $\check{B}_{int}$ to the actually measured B_{int} and uses the resulting error term to improve the estimation of the underlying susceptibility $\check{\chi}$. To improve conversion and the estimation we include information from the structural image (M and W) such as limiting the result to just brain tissue and restricting sudden jumps in susceptibility, to "push" the solution in the right direction.

6.2.6 Improved reconstruction techniques

Alternative methods have also been used which vary in the way they estimate the initial guess and which extra information to include. In areas where the gradients in the magnitude image do not match the actual gradients in the underlying susceptibility distribution, the previously described method would suppress the signal and remove contrast. To overcome this problem, the iLSQR method used in parts of this work (Li et al. 2015) uses a multi-step approach. First, an initial estimation is performed using a standard least squares (LSQR) method (Li, Wu, and Liu 2011), after which a fast and simple threshold-based inversion is performed to estimate susceptibility boundaries where susceptibility artifacts could occur. This information is then used to create a final reconstruction described as:

$$\chi_{iLSQR} = \chi_{LSQR} - FT^{-1}(X_{artifacts}(k) \cdot M_{ill-conditioned})$$

Where $X_{artifacts}(k)$ are the estimated susceptibility artifacts in k-space $M_{ill-conditioned}$ is the mask of the ill-conditioned regions.

6.2.7 Interpretation of QSM measures and their quantitative value

Because the center of the dipole-inversion kernel $D(\boldsymbol{k})$ is also undefined, all dipole-inversion approximation methods have in common that they can only approximate the variations ("AC") in the image, but not the constant (“DC”) component. To overcome these potential differences in estimated constant component between subjects, all susceptibility values have to be referenced to 1 region that is considered most stable for all subjects. However, it has also been shown that the effect of this constant component is often negligible, which is currently still debated (Betts et al. 2016). Because in the context of potential AD pathology all brain regions could be affected the following approach was chosen: the means of the standard deviations of susceptibility in commonly accepted QSM reference regions, such as various white matter bundles and sections of the cerebrospinal fluid, were evaluated to select the region with the lowest mean standard deviations as the reference region (Deistung, Schafer, et al. 2013).

Finally, for clarity and consistency with earlier studies, changes in susceptibility values will be referred to as changes in iron-load, due to the previously demonstrated correlation of susceptibility values with tissue iron-load in brain gray matter (Deistung, Schafer, et al. 2013; Li, Wu, and Liu 2011; Lim et al. 2013; Schweser et al. 2012).

6.2.8 Alternatives to QSM: susceptibility weighted, phase, T2* and R2* imaging

Several other methods have been used to quantify the changes originating from iron which are measurable by MRI, before the uptick in QSM-based research.

- **Susceptibility Weighted Imaging (SWI):** SWI uses the same GRE experiment as used for QSM to exploit the susceptibility differences between tissues and uses the phase image to detect these differences. Both the magnitude and phase data is saved after which high pass filtering is applied to remove unwanted artifacts. The magnitude and phase data are used together to create the SWI dataset by multiplying a phase mask image into the original magnitude image (Haacke et al. 2009; Mittal et al. 2009). These images are particularly sensitive to veins and as such can be used to investigate the vasculature. SWI images do now use point-source localization like in QSM and as such iron rich areas spill signal into surrounding areas. The processing and filtering also removes several (lower frequency) components from the signal and cannot be used for quantification. For clinical settings, the excellent vessel contrast makes it a good diagnostic tool.
- **Phase imaging:** Using simple high-pass filtering the raw unprocessed T2* phase data can also be used to infer on local iron deposits since they affect the phase as discussed earlier. However, without QSM-processing this measurement is highly affected by non-local effects of iron or myelin

rich structures. Relative quantification is possible, but due to the previously mentioned non-local effects this method is far from precise (van Rooden et al. 2014).

- **T2* weighted imaging:** The raw unprocessed T2* weighted magnitude data can reveal any perturbations in the magnetic field, either from iron or other underlying tissue differences. This makes it a great clinical tool for example in cancer imaging or other conditions that require quick evaluation of differences without exact quantification (Tang et al. 2014).
- **R2* imaging:** Uses the multi-echo GRE data to curve-fit the T2* decay in each voxel. Has been shown to correlate well to iron-load in the gray matter (Daugherty and Raz 2016; House et al. 2007; Betts et al. 2016; Langkammer et al. 2010). R2* is a composite measure sensitive to T2 effects but also magnetic field inhomogeneities and can be driven by intravoxel spin dephasing near steep field gradients. Additionally, it is also sensitive to sources of external field fluctuation such as air cavities and other non-local field disturbances. Compared to QSM, R2* cannot correctly quantify very high iron-concentrations for example in iron-based contrast agents. Nonetheless it has been shown to be one of the easier alternatives to QSM that is still semi-quantitative and relates closely to local iron content (Langkammer et al. 2010). As myelin effects QSM (decreases the measured susceptibility) and R2* (increases the measured R2* value) differently, the methods can be combined to do quantitative analysis of myelin density in brain structures.

6.3 FLAIR MRI

Fluid attenuation inversion recovery (FLAIR) is a heavily T2-weighted technique resulting in the nerve connections of white matter to appear gray, and the congregations of neurons of gray matter to appear white, while the CSF appears dark (**Figure 8**). This is achieved by adjusting the inversion time (TI) of the FLAIR inversion recovery sequence such that at magnetic equilibrium there is no net transverse magnetization of fluid. On FLAIR images white matter hyperintensities (WMH) can be identified which are indications of local dysfunction of underlying axonal tracts. This can be due to breakdown of the axonal tracts or extravasation of fluid from the vascular system due to leakage or microbleeds. WMH have been associated with various cognitive disorders such as multiple sclerosis, depression and AD (Schmidt et al. 2012; Schreiner et al. 2014; Sperling et al. 2012). At higher age and in AD pathology, SVCD is assumed to be the main cause of WHM and as such a large potential source of cortical iron deposits.

Manual delineation of WMH is time-consuming in larger samples such as the samples used in this work, therefore an automated method was implemented. Each participant's FLAIR images were segmented into gray matter and major white matter regions using a previously generated atlas. The WMH in each white matter region were automatically identified by segmenting and grouping voxels with intensities *1.5* standard deviation above the average gray matter intensity of each subject (Iorio et al. 2013). Automatically segmented regions were then and manually validated. The SVCD-burden was inferred on by summing the number of regions exhibiting WMH.

The WMH score is only a rough estimator of vascular integrity because WMH can also be caused by other pathologies, it's extension to the gray matter can therefore be debated. In future studies other measures of vascular integrity, such as contrast-enhanced MRI or PET-measures, should be used to properly investigate the effect of SVCD on brain iron in a context of AD.

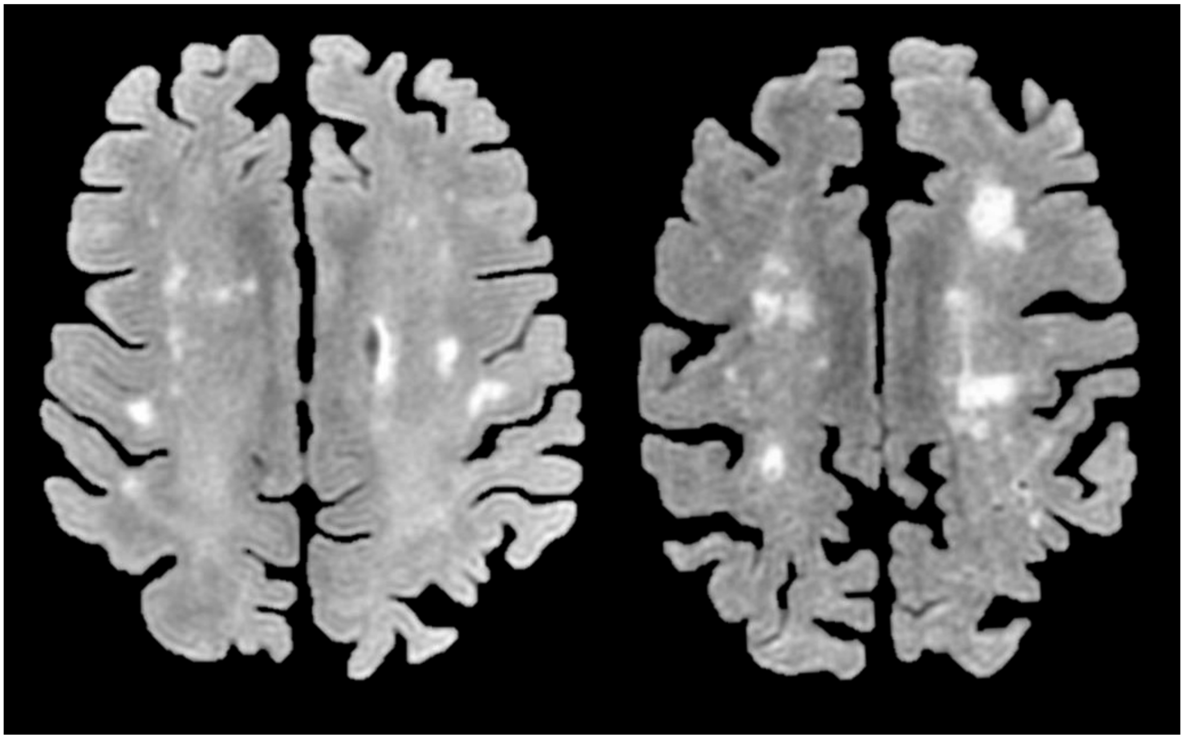

Figure 8: *Example 3T FLAIR images for 2 subjects acquired as part of the imaging samples used in this work. Both exhibit strong white matter hyperintensities.*

6.4 fMRI

6.4.1 fMRI background

Functional magnetic resonance imaging (fMRI) has made it possible to infer on brain activity in vivo throughout the brain, either while performing a task or with the brain at rest (Biswal et al. 1995). fMRI exploits a mechanism described in the previous section: Magnetic susceptibility. The change from oxyhemoglobin to deoxyhemoglobin alters the measured MRI signal and is therefore described as the blood oxygen level-dependent (BOLD) signal. The BOLD response is governed by 3 consecutive physiological processes: neuronal response, signaling and vascular response.

Using simultaneous fMRI and electrophysiology it was found that the measured BOLD signal reflects the input and the intracortical synaptic processing rather than the spiking output of a given brain area (Logothetis et al. 2001). When such activation is present, there will be an increase in demand for oxygen and nutrients. The local neuronal environment will signal to the blood vessels (arterioles) to increase cerebral blood flow (CBF) in order to satisfy this demand. At onset of activation the resulting consumption of oxygen causes the weakly diamagnetic oxyhemoglobin to release O_2, transforming it to paramagnetic deoxyhemoglobin, leading to a drop in measured MRI signal. This signaling occurs both through metabolic signaling from the increase local energy consumption and through neurotransmitter signaling. The respective contributions of the two factors differs across the brain. In response to the signaling the local and upstream vasculature responds by adapting the tone of the vascular wall in order to increase the local cerebral blood flow and volume (**Figure 9**).

The described cascade has been validated in healthy subjects (Logothetis 2008; Logothetis et al. 2001), however, all three steps leading to BOLD signal can be affected by disease pathology. This can be advantageous when investigating baseline changes such as in resting state analysis, but can strongly affect results in task-fMRI where controls are compared to diseases populations.

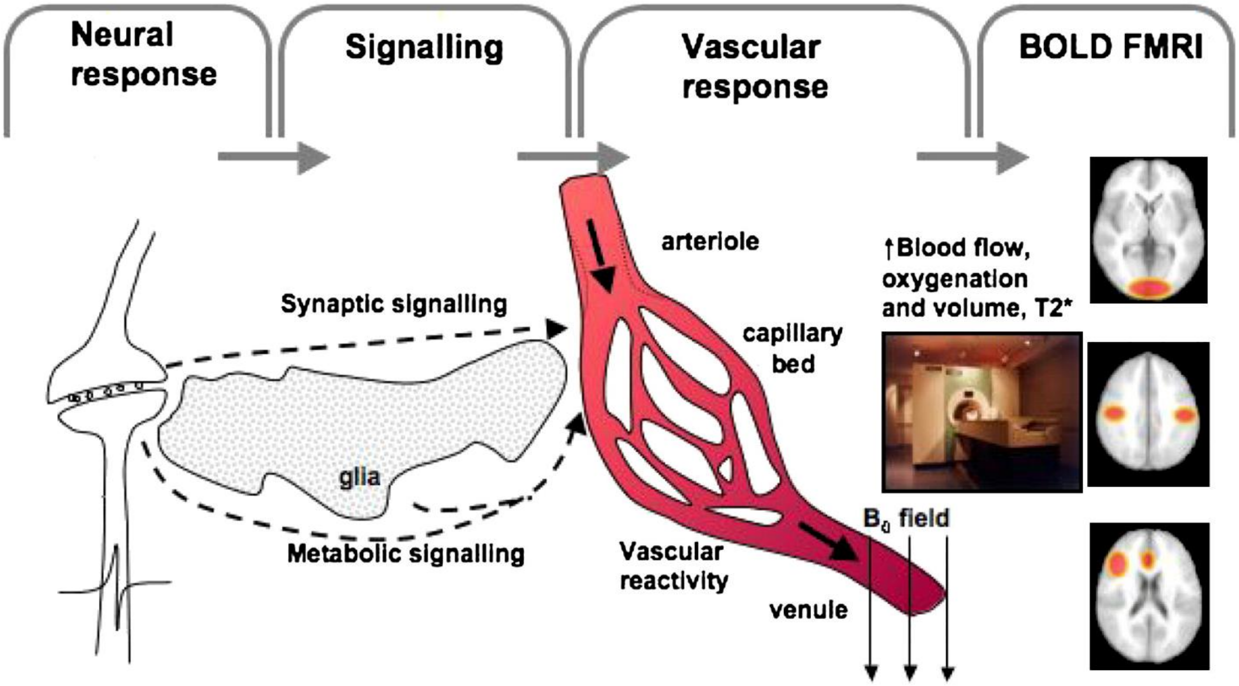

Figure 9: *Adapted from (Iannetti and Wise 2007). Schematic overview of the generation of the blood oxygen level-dependent (BOLD) signal.*

6.4.2 fMRI resting state analysis

At the advent of fMRI analysis, the focus was on task-related fMRI in which the brain’s activity during a task is compared to the baseline activity to identify task-associated brain regions. It was observed that the BOLD signal has slow spontaneous fluctuations at rest (< 0.1 Hz), but this was initially regarded as noise resulting from vascular properties instead of brain activity. Later it was observed that this activity at rest is synchronous across brain regions, indicating functional connectivity between regions (Biswal et al. 1995) (**Figure 10**). The significance of resting state BOLD signal correlations was given little importance until visual representations of one of the key resting state networks, the default mode network (DMN), were published and were found relevant in a neuroscience context (Greicius et al. 2003). Task-related fMRI was not used in this work and therefore the next sections only describe resting state fMRI (rsfMRI) processing.

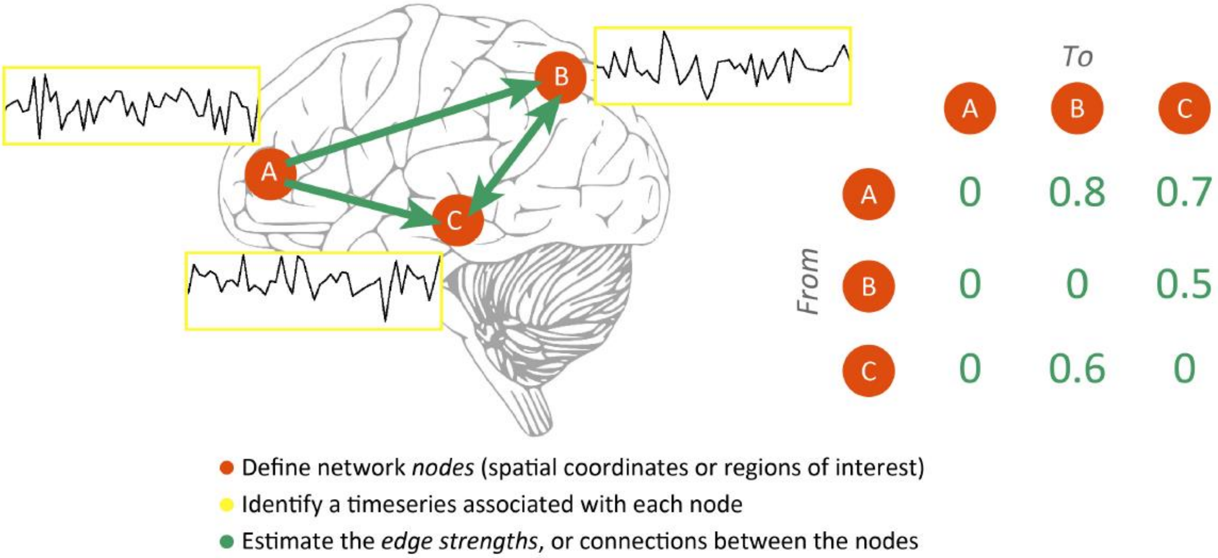

Figure 10: *Adapted from (Smith et al. 2013). Basic concept of rsfMRI: calculate correlation of temporal activity across voxels and as such brain regions (nodes, indicated as A, B, C).*

6.4.3 fMRI resting state processing

Before the rsfMRI scan subjects are asked to "lie still, do not think of anything in particular and to not fall asleep" while the BOLD signal is measured for 8 minutes (values between 5-15 minutes are common in rsfMRI studies). Most common MRI sequence to measure this signal is gradient echo planar imaging (EPI) in which one 2D slice is acquired to cover the whole brain within 2-3s with a spatial resolution of around 3-5mm in each dimension. Consecutively a structural scan with higher resolution is acquired in order to map activations to brain regions.

Various software packages are available to process the raw 4D rsfMRI data using standardized approaches. In this work the CONN-toolbox (Whitfield-Gabrieli and Nieto-Castanon 2012) is used in which the following pre-processing steps are performed:

1. Analyze and realign changes in orientation of the rsfMRI data over time due to head motion.
2. Warp the high resolution structural scan to Montreal Neurological Institute (MNI) standardized-space and use the deformation matrixes to also warp the rsfMRI data to this space.
3. Use the structural image in MNI space to generate tissue maps in order to separate non-brain regions, gray matter and white matter.
4. Smoothing of the rsfMRI data is applied to improve signal-to-noise ratio and statistical power.
5. Filtering of rsfMRI data to remove the slowest temporal drifts.

6. Regression of motion parameters (estimated in step 1) and signal changes from the CSF.
7. Independent component analysis (ICA) identifying noise components which are subsequently removed.

After pre-processing temporal synchronicity between spatially separated voxels needs to be calculated (**Figure 10**). This can either be done in a seed-based approach, in which a seed region is selected and time courses in all other voxels are compared to the seed region, or an ICA analysis to identify similar components throughout the brain (Cole, Smith, and Beckmann 2010). While seed-based approach allows for less variation due to possible underlying changes since the seed is fixed, ICA requires manual identification of significant components and is less established. Both techniques are used throughout currently published works, with a tentative preference for ICA in more recent works.

When the networks are identified, comparisons can be made on a group or linear-correlation basis. Either participants are grouped based on some classifier and the same network is compared between the two groups, or within the selected network voxels are weighted by a linear value for each subject and evaluated for significance within the whole sample. The statistics involved for these large 4D datasets is called Statistical Parametric Mapping (SPM) (Friston 1994), in which a General Linear Model (GLM) is used to describe the statistical contrast being tested as a correlation between measurements and a design matrix with a noise term. Correction for multiple testing is handled by applying Gaussian random fields theory (Friston 1994) after T-testing of each voxel for significance.

6.5 Volumetric analysis

Volume loss of gray matter, particular in memory regions such as the hippocampus and temporal lobe (Ball et al. 1985), is a common feature of AD. Reduced hippocampal volume correlates to early memory decline, however, it is also a feature of other dementias and even of regular aging (Driscoll et al. 2003). In this work we did not focus particularly on advanced volumetric analysis, such as Voxel-based morphometry (VBM) (Mechelli et al. 2005) or advanced hippocampus sub-segmentations (Pipitone et al. 2014).

To analyze local iron and β-amyloid plaque-load subject-specific segmentations are required to select regions of interest (ROIs). While many standardized approaches are available for segmentation in software packages like SPM, they are based on healthy brains and are not very well suited for diseased brains which can be anthropic or have enlarged ventricles. Therefore, the T1-weighted image was segmented using a multi-atlas matching approach consisting of 143 Regions of Interest (ROIs) developed as part of the Johns Hopkins University brain atlas. The atlas system is optimized for the parcellation of potential non-healthy brains by applying a Multiple-Atlas Likelihood Fusion algorithm and Ontology Level Control technology on the JHU multi-atlas sets (Djamanakova et al. 2014; Tang et al. 2013; Mori et al. 2016). Specifically, the atlas set of 26 participants aged between 50 and 90 years was used to cover all possible types of brain morphologies in the investigated populations.

To normalize different brain sizes across participants, individual structural volume was corrected with the following approach: *Corrected structure volume = Original structure volume × (whole sample mean intracranial volume / participant intracranial volume).* To investigate possible relationships between structure volume and local β-amyloid plaque-load or local iron-load, gray-matter regions of interest (ROIs) were selected from the generated atlas based on earlier reports on distribution of brain pathology at early stages of AD (Frisoni et al. 2010; Serrano-Pozo et al. 2011). ROI-masks were eroded with two pixels to account for partial volume effects before being used as a mask to analyze average iron-load (QSM) and β-amyloid burden.

6.6 Biological Parametric Mapping (BPM)

The Biological Parametric Mapping (BPM) toolbox (Casanova et al. 2007; Yang et al. 2011a, 2011b) is an extension of the previously described SPM analysis to evaluate voxel wise correlations between two imaging modalities while controlling for covariates. The SPM analysis only has one statistical result for each voxel when checking for significance using random fields theory, because there is only one T/F-test result per voxel (**Figure 11**). When correlating two modalities per subject, each voxel in the resulting statistical image has the correlation statistic for each subject (**Figure 11**). Therefore, BPM uses an adapted version of the random fields theory for 3D correlation volumes.

The main limitation of this approach is that all data needs to be converted to standard space, usually MNI-space. In case of fMRI data the lower resolution and general smoothness of the signal mitigates issues to sub-optimal transformation to standard space. However, in higher resolution images such as QSM or β-amyloid-PET that also are strictly limited to being relevant in gray matter, quality of transformation could be a significant issue. Therefore, the optimized conversion to standard space of the Johns Hopkins University was used.

As described previously, the larger samples used in this work were acquired on an integrated PET-MRI, limiting distortion by processes of co-registration of PET with MRI images or bias due to changes occurring in the time between PET and MR acquisition.

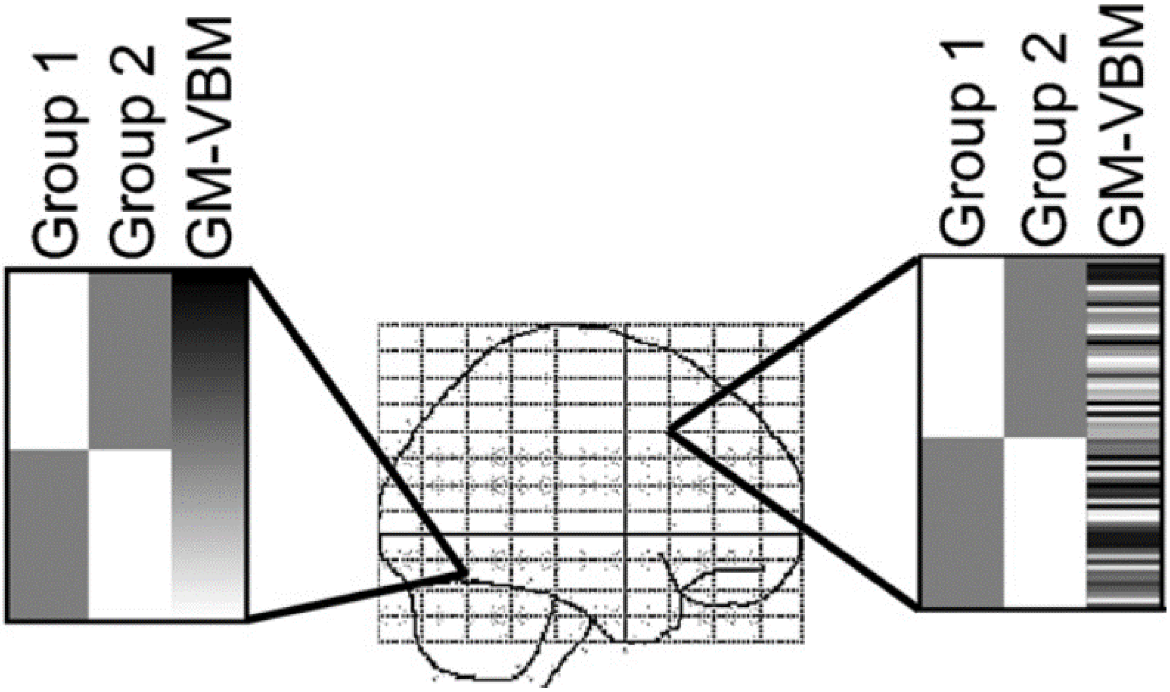

Figure 11: *Adapted from (Casanova et al. 2007). Differences between SPM analysis (left) and BPM analysis (right). In SPM all voxels have the same design matrix with set values for each voxel (left, column 3), while in BPM each voxel has a unique design matrix where it contains the unique imaging values for each subject in that voxel (right, column 3).*

7 Colocalization of cerebral iron with amyloid beta in Mild Cognitive Impairment

J.M.G. van Bergen[1]*, X. Li[2,3], J. Hua[2,3], S. J. Schreiner[1,4], S. C. Steininger[1,4], F.C. Quevenco[1],
M. Wyss[5], A. F. Gietl[1,4], V. Treyer[1,6], S. E. Leh[1,4], F. Buck[6], R. M. Nitsch[1,4],
K. P. Pruessmann[5], P.C.M. van Zijl[2,3], C. Hock[1], P. G. Unschuld[1,4]

[1] Institute for Regenerative Medicine, University of Zürich, Switzerland

[2] The Russell H. Morgan Department of Radiology and Radiological Science, Division of MR Research, The Johns Hopkins University School of Medicine, Baltimore, Maryland, USA

[3] F.M. Kirby Research Center for Functional Brain Imaging, Kennedy Krieger Institute, Baltimore, Maryland, USA

[4] Hospital for Psychogeriatric Medicine, University of Zürich, Switzerland

[5] Institute for Biomedical Engineering, University of Zürich and ETH Zürich, Zürich, Switzerland

[6] Department of Nuclear Medicine, University Hospital Zürich and University of Zürich, Zürich, Switzerland

Published in Scientific Reports (van Bergen, Li, et al. 2016)

7.1 Abstract

Quantitative Susceptibility Mapping (QSM) MRI at 7 Tesla and 11-Carbon Pittsburgh-Compound-B PET were used for investigating the relationship between brain iron and amyloid beta (Aβ) plaque-load in a context of increased risk for Alzheimer's disease (AD), as reflected by the Apolipoprotein E ε4 (APOE-e4) allele and mild cognitive impairment (MCI) in elderly subjects. Carriers of APOE-e4 with normal cognition had higher cortical Aβ-plaque-load than non-carriers. In MCI an association between APOE-e4 and higher Aβ-plaque-load was observable both for cortical and subcortical brain-regions. APOE-e4 and MCI was also associated with higher cortical iron. Moreover, cerebral iron significantly affected functional coupling, and was furthermore associated with increased Aβ-plaque-load (R^2-adjusted=0.80, $p<0.001$) and APOE-e4 carrier status ($p<0.001$) in MCI. This study confirms earlier reports on an association between increased brain iron-burden and risk for neurocognitive dysfunction due to AD, and indicates that disease-progression is conferred by spatial colocalization of brain iron deposits with Aβ-plaques.

7.2 Introduction

Alzheimer's disease (AD) is the most frequent cause of dementia and significantly increased risk for AD-dementia is associated with advanced age, mild cognitive impairment (MCI) and carrier-status of the Apolipoprotein E **ε**4 allele (APOE-e4)(Corder et al. 1993). Neuropathological hallmarks of AD include both intracellular pathological neurofibrils as well as extracellular accumulation of amyloid beta (Aβ) plaques (Morris et al. 2010; Schmechel et al. 1993). Particularly the accumulation of Aβ-plaques is considered to potentially represent preclinical disease stages (Liu et al. 2015; Sperling et al. 2015; Nitsch and Hock 2008). The APOE-e4 allele has been shown to be closely associated with the extent of cerebral Aβ-plaque-load (Reiman et al. 2009) and both exert interactive effects on cognitive decline (Mormino, Betensky, Hedden, Schultz, Amariglio, et al. 2014; Mormino, Betensky, Hedden, Schultz, Ward, et al. 2014). Recent data demonstrate that the risk for developing AD-dementia, as conferred by APOE-e4 carrier status, is closely linked to cerebral iron-burden, implicating potential benefit of therapeutic strategies aimed at lowering brain iron in this patient population (Wood 2015; Ayton et al. 2015).

Accumulation of iron in the human brain is a characteristic finding in several neurodegenerative disorders (Barbosa et al. 2015; Murakami et al. 2015) and has been reported for AD both in post-mortem studies (House et al. 2007; Bush 2013; Connor, Menzies, et al. 1992; Connor, Snyder, et al. 1992) as well as in vivo by using magnetic resonance imaging (MRI) (Bartzokis et al. 2000; Bartzokis and Tishler 2000; Acosta-Cabronero et al. 2013). In its normal function, amyloid precursor protein (APP) facilitates iron transport outside the cell (Duce et al. 2010). In mammalian cell cultures iron has been demonstrated to interfere in the aggregation of Aβ and thus may significantly promote Aβ neurotoxicity in AD (Liu, Moloney, et al. 2011). Additionally, local iron deposits are considered to reflect mitochondrial dysfunction (Bishop, Lu, and Yankner 2010) and abnormal microglial activation (Zeineh et al. 2015) in a context of pathological brain change taking place in AD. Recent developments on quantitative susceptibility mapping (QSM) techniques (Deistung, Schafer, et al. 2013; Lim et al. 2013; Langkammer et al. 2012; Schweser et al. 2012; Li, Wu, and Liu 2011) have made it possible to directly map brain tissue magnetic susceptibility, which has been shown to correlate well with tissue iron concentration in cerebral gray matter (de Rochefort et al. 2010; Deistung, Schafer, et al. 2013; Lim et al. 2013; Langkammer et al. 2012; Schweser et al. 2012; Li, Wu, and Liu 2011).

Positron Emission Tomography (PET) for measuring cerebral Aβ-plaque-load has been combined with functional MRI (fMRI) at rest for inferring on functional network integrity, in several studies so far that included both cognitively normal populations of elderly subjects, as well as individuals with MCI and manifest AD-dementia (Huijbers et al. 2014; Sperling et al. 2009; Johnson, Sperling, and Sepulcre 2013). Interestingly, there is a significant overlap between brain regions characterized by altered functional connectivity and localization of AD-pathology (Mintun et al. 2006). This overlap particularly affects structures connected with the medial prefrontal cortex (MPFC), which is a central hub within the default-mode network (DMN) and thus is considered to have spatially specific effects on neuronal functionality, as reflected by downstream memory deficits (Buckner 2005; Sheline et al. 2010; Sperling et al. 2010; Ward et al. 2014). The application of MRI at ultra-high field strength of 7 Tesla (7T) inherently increases signal to noise ratios (SNR) in QSM and BOLD fMRI, due to the linear relationship between susceptibility induced field shift and field strength, and supralinear relationship between BOLD contrast and field strength, respectively, allowing for detecting subtle changes in the brain with relatively small sample size (Hua et al. 2011; Hua et al. 2014; Schweser et al. 2012).

At this point several neuropathological and neuroimaging studies have demonstrated the close relationship between increased risk for AD and prevalence of MCI, APOE-e4 carrier status, Aβ-plaque-load and altered functional connectivity (Sperling et al. 2011), and also an association between APOE-e4 carrier status and increased brain iron-load (Ayton et al. 2015). However, to our knowledge there are no studies published on the impact of brain iron-load on functional brain network integrity and prevalence of regional Aβ-plaque-load in subjects at risk for AD. As the extent of regional Aβ-plaque-load may be estimated by applying radioactive tracers such as 11C-Pittsburgh Compound B for PET (PiB-PET) (Klunk et al. 2004; Solbach et al. 2005) and cerebral iron can be measured by QSM (Langkammer et al. 2012), the combination of QSM with PiB-PET can be used to infer on Aβ-plaque related iron-load. Thus, for the current study the following questions were investigated in a study population of elderly subjects with normal cognitive performance and MCI:

A) To investigate a potential relationship between increased AD-risk, as reflected by MCI and APOE-e4 carrier-status, with cerebral iron-burden, as measured by whole-brain QSM at ultra-high field strength of 7T.

B) To estimate combined effects of MCI and increased cerebral iron-load on MPFC-coupling by resting state BOLD fMRI.

C) To characterize the relationship between iron-load and Aβ-plaque density in brain regions with altered MPFC-coupling by whole-brain QSM and 11C-PiB-PET data.

7.3 Methods

7.3.1 Participants

37 study participants aged between 62 and 89 years (22 cognitively normal, 15 MCI) without evidence of significant medical illness, were recruited as part of an ongoing study at our hospital. The study was conducted in accordance with good clinical practice guidelines issued by the local ethics committee (Kantonale Ethikkommission Zürich), as well as with the declaration of Helsinki. All procedures were approved by the Kantonale Ethikkommission Zürich. Written informed consent was obtained from all participants before inclusion in the study.

All participants received psychiatric examination and neuropsychological testing during screening for eligibility to participate in the current study and were categorized either as cognitively normal or MCI according to established criteria for diagnosis of MCI (Petersen et al. 1999; McKhann et al. 2011). Neuropsychological tests included Mini Mental State Examination (Folstein, Folstein, and McHugh 1975) (MMSE), Montreal Cognitive Assessment (Nasreddine et al. 2005) (MOCA), Verbal Learning and Memory Test (Helmstaedter and Durwen 1990) (VLMT), Wechsler Memory Scale (Howard 1950) (WMS), Boston Naming Test (Nicholas et al. 1989) (BNT) and Trail Making Test (Tombaugh 2004). Clinical examination including clinical workup and neuropsychological testing were administered within 30 days of the PiB-PET scan and 7T MRI scan. Isoforms of the APOE gene were assessed for all participants (Tanzi 2012).

Exclusion criteria for the current study were: severe cognitive deficits indicating dementia, significant medication or drug abuse with possible effects on cognition, 7T MRI exclusion criteria (such as history of claustrophobia, vertigo, seizure disorder, middle-ear disorder, double vision and the presence of metals in or on the body), MRI scans with the evidence of infection, infarction, or other focal lesions, clinically relevant changes in red blood cell count, exclusion criteria for PiB-PET, history of severe allergic reactions to drugs or allergens, serious medical or neuropsychiatric illness and significant exposure to radiation.

7.3.2 Carbon-11 based Pittsburgh compound B Positron Emission Tomography (PiB-PET) for estimation of brain Aβ-plaque density

PiB-PET based estimation was used to estimate individual brain Aβ-plaque-load (Klunk et al. 2004). Individual dose of 350MBq of carbon-labelled PiB was injected into the cubital vein. Standard quantitative filtered back projection algorithm including necessary corrections was applied. Cerebral Aβ deposition values were extracted using PMOD Brain Tool software-package (PNEURO, Version 3.4, PMOD Technologies Ltd, Zürich, Switzerland). Late frame (minutes 50-70) values were standardized by the cerebellar gray matter average, resulting in 3D-volumes of PiB-PET retention (matrix=128x128x47, voxel size=2.3x2.3x3.3 mm). As a single measure of individual cortical Aβ-plaque-load, cortical PiB retention scores were determined by calculating a composite score using merged cortical PiB-PET intensity values, as reported earlier (Vandenberghe et al. 2010).

7.3.3 MRI data acquisition

All subjects were scanned using a Philips 7-Tesla Achieva whole-body scanner (Philips Healthcare, Best, The Netherlands) equipped with a Nova Medical quadrature transmit head coil and 32-channel receive coil array. A T1-weighted MP2RAGE image (TR/TE = 4.8ms/2.1ms, voxel size=0.6x0.6x0.6mm^3, SENSE-factor=2x1x2, scan duration=7:50min) was acquired for anatomical referencing and automated image segmentation. MR phase measurements used for QSM calculation were acquired using a multi-echo 3D gradient recalled echo (GRE) sequence with 3 echoes (TR/TE/ΔTE=23/6/6ms, flip angle=10°, voxel size=0.5x0.5x0.5mm^3, SENSE-factor=2.5x1x2, flow-compensated, scan duration=13:48min). Phase data acquired with an echo time in the range of 12-18ms was used for QSM reconstruction. rs-fMRI was acquired using 3D T2-prep GRE sequence (Hua et al. 2014) (TR=2s, TR_{GRE}/TE_{GRE}=3.08/1.6ms, voxel size=1.5x1.5x1.5 mm^3, scan duration=7:03min). The high resolution GRE images were inspected (by P.U.) for any imaging artifacts or abnormalities, in particular cerebral microhaemorrhages (microbleeds).

7.3.4 MRI data processing

7.3.4.1 Quantitative susceptibility mapping (QSM) for measuring brain iron-load

Multiple processing steps were performed to calculate from acquired MR phase images the quantitative susceptibility maps of which local cerebral iron-load is inferred. First, phase unwrapping was performed using Laplacian based discrete phase unwrapping (Li, Wu, and Liu 2011). A brain mask was then obtained by skull-stripping the GRE magnitude image acquired at TE of 12ms using FSL's brain extraction tool (BET, FMRIB Oxford, UK) with fractional threshold of 0.3. The unwrapped phase images were then divided by 2π*TE to obtain an image of the frequency shift in Hz for each echo. Subsequently, background fields were eliminated with the sophisticated harmonic artifact reduction for phase data (SHARP) (Schweser et al. 2011) approach using a variable spherical kernel size with a maximum radius of 4mm and a regularization parameter of 0.05 (Schweser et al. 2011). After removal of background fields, the resulting images of the two echoes were averaged to obtain a higher SNR as compared to single echo reconstruction (Wu, Li, Avram, et al. 2012; Wu, Li, Guidon, et al. 2012). Inverse dipole calculations to obtain the susceptibility maps were performed using a LSQR based minimization (Li, Wu, and Liu 2011). From suitable reference regions such as white matter tracts and central cerebral spinal fluid (CSF) regions (Deistung, Schafer, et al. 2013; Deistung, Schweser, et al. 2013), the region having the lowest standard deviation of mean susceptibility in all subjects was selected. In this sample the frontal central CSF region in the lateral ventricles was selected as a reference region for the final susceptibility quantification. All reported susceptibility values are then relative to the mean susceptibility value of this reference region. Classification of all subjects as “high” or “low” cerebral iron content was performed by a median split of the average cortical gray matter susceptibility of all subjects, in the same regions used for the determination of the individual cortical Aβ-plaque-load (Vandenberghe et al. 2010).

7.3.4.2 Assessment of structure volumes and mean susceptibility

In order to assess atrophy and susceptibility differences between MCI subjects and controls, the T_1-weighted image was co-registered to the GRE magnitude image. The co-registered T_1 image was then segmented using a multi-atlas matching approach developed as part of the Johns Hopkins University brain atlas, which is optimized for the parcellation of non-healthy brains (Tang et al. 2013; Djamanakova et al. 2014). ROIs were selected in the basal ganglia and several cortical gray matter structures for which mean susceptibility was calculated after eroding the ROI-masks with two pixels (1mm) to account for partial volume effects and possible edge artifacts in cortical ROI’s. To normalize different brain sizes across subjects, individual structural volume was corrected with the following approach: *Corrected structure volume = Original structure volume × (group mean intracranial volume / subject intracranial volume)*.

7.3.4.3 fMRI analysis

Pre-processing of the rs-fMRI data was performed using SPM12 (http://www.fil.ion.ucl.ac.uk/spm/), the following steps were performed: realignment, slice time correction, co-registration of structural scan, segmentation, normalization and smoothing (FWHM=4). The iron classification and MCI status were used as the covariates of interest in connectivity analysis using the CONN toolbox (Whitfield-Gabrieli and Nieto-Castanon 2012). The signal was filtered with a band-pass filter using the default CONN setting of 0.01–0.1 Hz. Seed-to-voxel analysis was performed with the seed placed in the MPFC. Motion parameters (extracted using the Artifact Detection Tool, ART, https://www.nitrc.org/projects/artifact_detect/), CSF, and white matter were regressed out, as variables of no interest. Connected voxels were included in the mask if they had a False Discovery Rate (FDR) corrected probability of $p<0.001$. Using this mask gray matter susceptibility and PiB-PET retention values were extracted and averaged for each subject.

7.3.5 Statistics

To examine the differences between groups 1-way MANCOVA was performed with the mean magnetic susceptibility or tissue volume of each brain structure as the outcome variable, while controlling for age and gender, followed by False Discovery Rate (FDR) multiple testing correction (Benjamini and Hochberg 1995). Effect sizes were calculated using Cohen’s d. All statistical tests were performed using MATLAB R2014b (Mathworks, Natick, MA).

7.4 Results

7.4.1 Demographics of the study population.

Demographic information for the investigated study population and neuropsychological test performance at time of inclusion are summarized in **Table 1**. MCI and healthy controls differed significantly in scores on the neuropsychological tests MOCA, VMLT, Boston Naming Test and WMS. Example PiB-PET images and QSM maps can be seen in **Figure 1**. Cortical PiB-PET retention differed significantly ($p=0.006$, effect size=3.1) between the two groups. The frontal central CSF region in the lateral ventricles, which was used as a reference for susceptibility calculations, was significantly different in volume (healthy: 19.1 ± 2.0 ml, MCI: 24.2 ± 3.3 ml, $p < 0.05$) but not in absolute susceptibility ppb reading before referencing (healthy: 5.8 ± 1.1 ppb, MCI: 5.6 ± 1.1 ppb). For all subjects, the median split of the average cortical PiB-PET retention was found to be 1.13 and the median split of the average cortical susceptibility was 3.0 ppb.

Accordingly, the study population was classified based on PiB-PET retention into “high” and “low” cortical PiB (“high”: 7 healthy, 11 MCI) and susceptibility for iron -load (“high”: 10 healthy, 8 MCI).

	Controls	**MCI**
N (F/M)	8 / 14	5 / 10
Age (years)	71.91 ± 5.25	75.27 ± 7.63
Education (years)	13.64 ± 2.56	15.2 ± 3.51
PiB-PET retention	1.16 ± 0.08	1.5 ± 0.17 **
APOE-e4 positive	7 (31%)	6 (40%)
MMSE	29.27 ± 0.70	28.61 ± 1.65
MOCA	27.36 ± 1.30	24.44 ± 2.17 **
VLMT: immediate recall	11.59 ± 2.22	7.11 ± 4.00 ***
VLMT: delayed recall	11.41 ± 2.94	6.83 ± 4.29 ***
VLMT: recognition	12.73 ± 2.31	7.78 ± 5.79 **
Boston Naming Test	14.68 ± 0.48	13.94 ± 1.26 *
WMS: pairs learning	14.76 ± 4.28	10.65 ± 4.72 **
WMS: pairs recall	5.52 ± 1.49	3.88 ± 1.75 **
Verbal Working Memory	6.32 ± 1.99	5.44 ± 1.42
Trail Making Test ratio	2.58 ± 0.74	2.6 ± 1.24

Table 1: *Demographic data and clinical assessment scores for control subjects with normal cognition and MCI subjects at time of inclusion in the study. Data are presented as mean ±standard deviation. APOE-e4 status presented as N (percentage of group). Age and Education are in years. * Significant difference between controls and MCI with $p < 0.05$, ** $p < 0.01$, *** $p < 0.001$.*

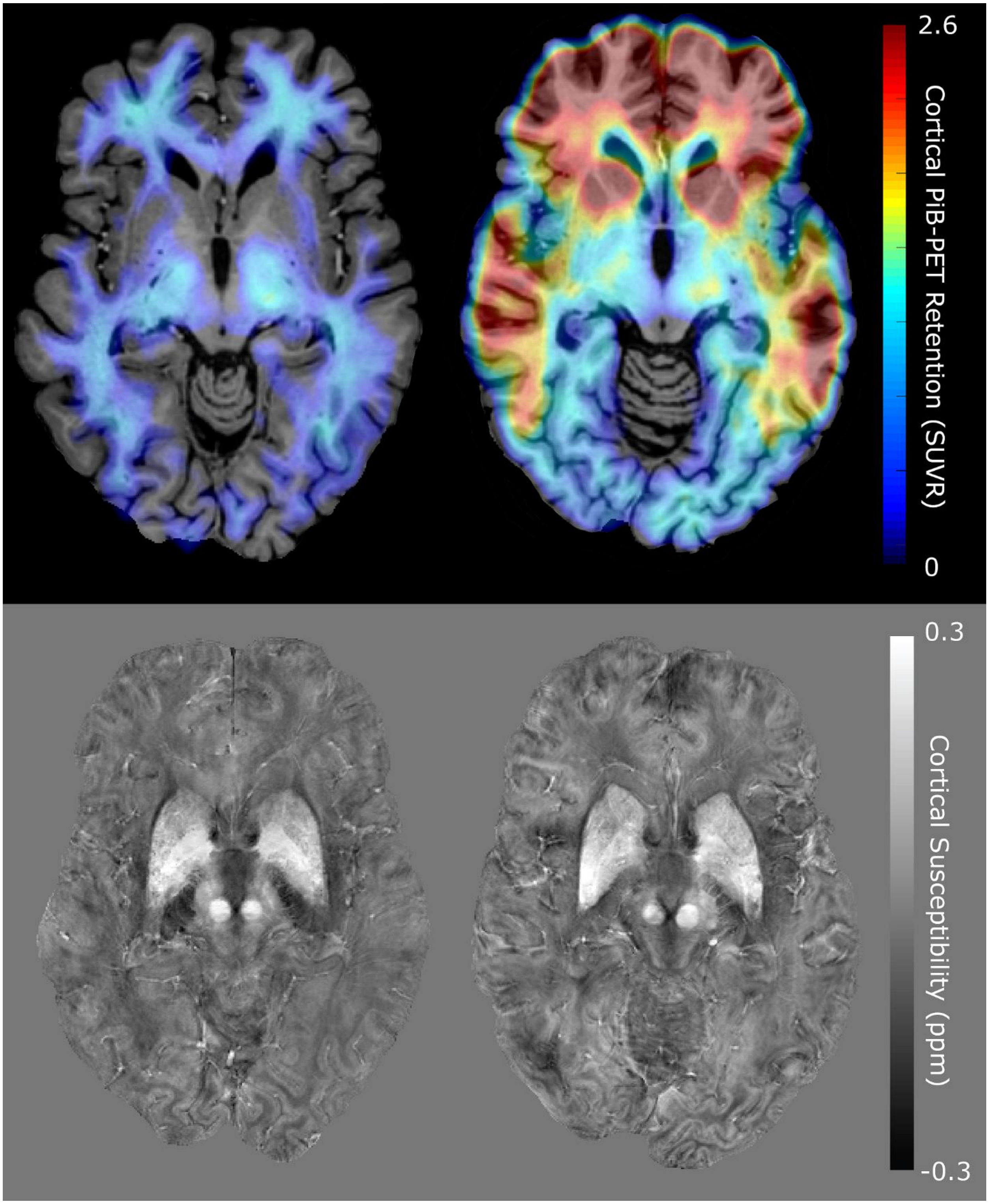

Figure 1: *Example images for a control subject (left) and MCI subject (right). The top row shows PiB-PET images of Aβ-plaque-load in gray matter, which is highly increased in the frontal regions in the MCI subject, the signal in the white matter is non-specific to Aβ-plaque-load and is also observed in the control subject. The bottom row shows QSM maps of the same slices indicating regions with high iron-load such as the basal ganglia.*

7.4.2 Effects attributable to MCI and APOE-e4 carrier status.

Corrected volume was significantly different between controls and MCI subjects in the amygdala, hippocampus, thalamus and putamen with p<0.001 and effect sizes of 0.80-1.2 (**Table 2**). However, no significant differences were found for the average susceptibility in any of these regions between the two groups.

	Corrected volume (ml) Mean ± STE		**χ (ppb) Mean ± STE**	
	Controls	**MCI**	**Controls**	**MCI**
Amygdala	4.03 ± 0.09	3.60 ± 0.15 ***	-16.6 ± 2.3	-17.4 ± 2.3
Nucleus Acc	1.76 ± 0.07	1.84 ± 0.10	11.8 ± 3.7	11.8 ± 5.5
Hippocampus	8.62 ± 0.18	7.55 ± 0.22 ***	-1.3 ± 1.7	-0.6 ± 2.9
Entorhinal Ctx	2.15 ± 0.13	2.01 ± 0.15	23.4 ± 3.8	25.8 ± 3.3
Thalamus	13.88 ± 0.19	12.83 ± 0.40 ***	-7.7 ± 1.8	-8.9 ± 1.8
Caudate Nucleus	9.53 ± 0.24	9.31 ± 0.30	41.4 ± 4.2	38.2 ± 3.7
Putamen	10.11 ± 0.27	8.92 ± 0.43 ***	63.6 ± 4.4	61.2 ± 4.3
Globus Pallidus	3.50 ± 0.07	3.35 ± 0.09	104.5 ± 4.9	99.3 ± 5.0
Frontal Ctx	16.56 ± 1.98	16.13 ± 2.36	2.1 ± 1.8	2.6 ± 2.2
Temporal Ctx	23.24 ± 2.40	22.13 ± 2.77	0.3 ± 1.6	2.1 ± 2.1
Parietal Ctx	21.63 ± 1.13	21.23 ± 1.32	4.3 ± 1.6	4.0 ± 1.8
Occipital Ctx	18.76 ± 2.51	18.38 ± 2.93	3.6 ± 1.8	3.8 ± 2.1

Table 2: *Changes in corrected volume and susceptibility (referenced to CSF) between controls and MCI. Ctx = Cortex. Data are presented as mean ± standard error (STE). *** Significant difference between controls and MCI with p < 0.001.*

Splitting the analysis based on MCI and APOE-e4 status showed no significant susceptibility differences in cortical regions of control subjects but strong significant increases in APOE-e4 carriers in the caudate nucleus (**Table 3**, p<0.01, effect size=1.03) and frontal, temporal, parietal and occipital cortices (p<0.001, effect sizes=0.67-1.11) for the MCI group. APOE-e4 positive subjects had significantly higher levels of Aβ-plaque-load in general, as indicated by PiB-PET retention (APOE-e4 positives: 1.56±0.12, APOE-e4 negatives, 1.17±0.04, p=0.006). There was no significant effect of APOE-e4 status on the volume for any of the investigated cortical and subcortical regions (data not shown).

	Iron-load (χ, ppb) Mean ± STE			**Aβ-plaque-load (PiB-PET, SUVR) Mean ± STE**		
	APOE-e4 -	**APOE-e4 +**	*d*	**APOE-e4 -**	**APOE-e4 +**	*d*
A) Controls						
Amygdala	-17.2 ± 2.5	-15.3 ± 2.2	0.19	1.19 ± 0.02	1.19 ± 0.02	0.02
Nucleus Acc	12.1 ± 4.1	11.2 ± 3.2	0.06	1.17 ± 0.02	1.23 ± 0.03	0.64*
Hippocampus	-1.4 ± 1.7	-1.2 ± 2.1	0.02	1.25 ± 0.02	1.31 ± 0.02	0.70*
Entorhinal Ctx	22.6 ± 5.1	25.0 ± 2.6	0.15	1.08 ± 0.02	1.14 ± 0.01	0.92**
Thalamus	-6.5 ± 1.9	-10.5 ± 1.4	0.55	1.48 ± 0.04	1.48 ± 0.04	0.01
Caudate Nucleus	46.0 ± 3.7	31.5 ± 5.5	0.75*	1.26 ± 0.03	1.28 ± 0.03	0.23
Putamen	67.2 ± 4.3	55.9 ± 5.3	0.56	1.33 ± 0.02	1.36 ± 0.01	0.46
Globus Pallidus	106.4 ± 5.0	100.4 ± 5.7	0.26	1.45 ± 0.02	1.50 ± 0.04	0.34
Frontal Ctx	2.6 ± 1.9	1.1 ± 2.0	0.18	1.02 ± 0.03	1.13 ± 0.04	0.69***
Temporal Ctx	0.7 ± 1.6	-0.6 ± 2.0	0.17	1.04 ± 0.02	1.10 ± 0.04	0.48***
Parietal Ctx	4.1 ± 1.6	2.7 ± 1.8	0.25	0.99 ± 0.02	1.15 ± 0.05	1.07***
Occipital Ctx	4.0 ± 1.9	2.9 ± 1.8	0.14	1.14 ± 0.03	1.19 ± 0.04	0.42**
B) MCI						
Amygdala	-17.5 ± 1.8	-17.2 ± 2.6	0.04	1.07 ± 0.02	1.54 ± 0.03	4.01***
Nucleus Acc	8.2 ± 4.9	17.3 ± 4.7	0.44	1.16 ± 0.02	2.41 ± 0.07	7.00***
Hippocampus	-2.0 ± 2.0	1.5 ± 3.5	0.31	1.14 ± 0.03	1.42 ± 0.03	2.55***
Entorhinal Ctx	23.1 ± 3.4	30.0 ± 2.5	0.56	1.02 ± 0.03	1.31 ± 0.03	2.80***
Thalamus	-9.1 ± 1.4	-8.5 ± 2.1	0.07	1.46 ± 0.02	1.80 ± 0.06	1.95***
Caudate Nucleus	32.7 ± 2.0	46.3 ± 4.5	1.03**	1.24 ± 0.04	2.13 ± 0.09	3.40***
Putamen	58.6 ± 3.7	65.2 ± 4.0	0.41	1.29 ± 0.01	2.23 ± 0.05	7.29***
Globus Pallidus	96.4 ± 3.3	103.5 ± 6.3	0.36	1.41 ± 0.03	1.92 ± 0.06	2.86***
Frontal Ctx	0.1 ± 1.6	6.3 ± 2.2	0.78***	0.98 ± 0.05	1.95 ± 0.10	3.32***
Temporal Ctx	0.0 ± 1.8	5.2 ± 1.8	0.67***	1.03 ± 0.02	1.73 ± 0.07	3.50***
Parietal Ctx	1.3 ± 1.2	8.1 ± 1.8	1.11***	1.00 ± 0.03	1.87 ± 0.09	3.60***
Occipital Ctx	1.5 ± 1.4	7.2 ± 2.4	0.71***	1.13 ± 0.02	1.59 ± 0.08	2.20***

Table 3: *Quantitative magnetic susceptibility (χ in ppb referenced to CSF) and PiB-PET retention (SUVR) separated by APOE-e4 status within the two groups. * Significant difference between APOE-e4 positive and negative with $p < 0.05$, ** $p < 0.01$, *** $p < 0.001$. d indicates effect sizes (Cohen's d).*

7.4.3 The combination of MCI with high iron-load is associated with altered MPFC-coupling.

The rs-fMRI functional connectivity analyses using MCI status and iron classification as covariates resulted in a mask consisting of 1502 voxels of significantly increased activation (p-FDR-corrected<0.001) with T(1,7) = 10.99. Main regions include frontal pole right (276 voxels, 3% of ROI), paracingulate gyrus left (188 voxels, 14%), frontal medial cortex (145 voxels, 15%), cingulate gyrus (146 voxels, 6%), frontal pole left (122 voxels, 2%) and paracingulate gyrus right (116 voxels, 9%), see also **Figure 2**.

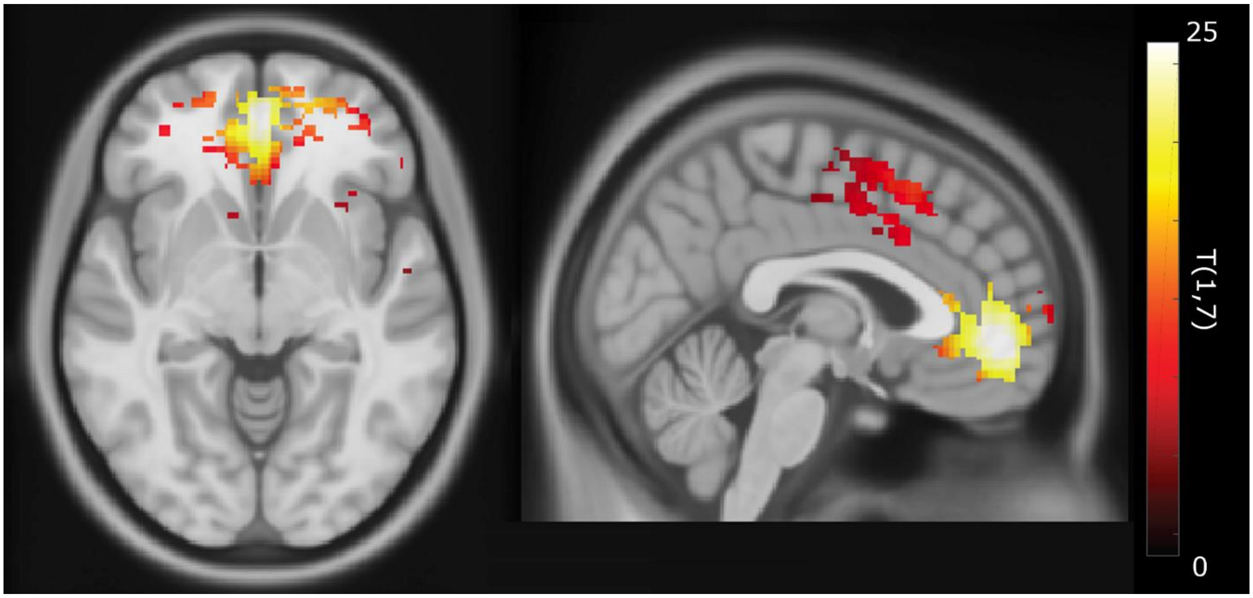

Figure 2: *Regions that show significant increased iron associated coupling (T(1,7) above 10.99 indicating p-FDR-corrected<0.001) with the medial prefrontal cortex (MPFC) in subjects with MCI.*

7.4.4 Susceptibility and Aβ-plaque-load correlate within brain regions defined by altered MPFC-coupling.

The mask of the region with significantly increased coupling was applied to the individual PiB-PET images and QSM maps of all MCI subjects (**Figure 3**). The Spearman's correlation between cortical PiB-PET retention and susceptibility was found to be $p<0.001$ (Spearman's rho=0.86, R^2-adjusted=0.80). Analysis of the extracted values per group showed significant increases of cortical PiB-PET retention and susceptibility in the APOE-e4 carrier group of the MCI subjects (**Figure 3**). Moreover, in the MCI group, the odds ratio for an APOE-e4 carrier to have "high" PiB-PET retention was 48 ($p<0.01$, 95% confidence interval=2.6-932.8) and 17.5 ($p<0.05$, 95% confidence interval=2.2-250.3) to be "high" iron compared to a non-carrier.

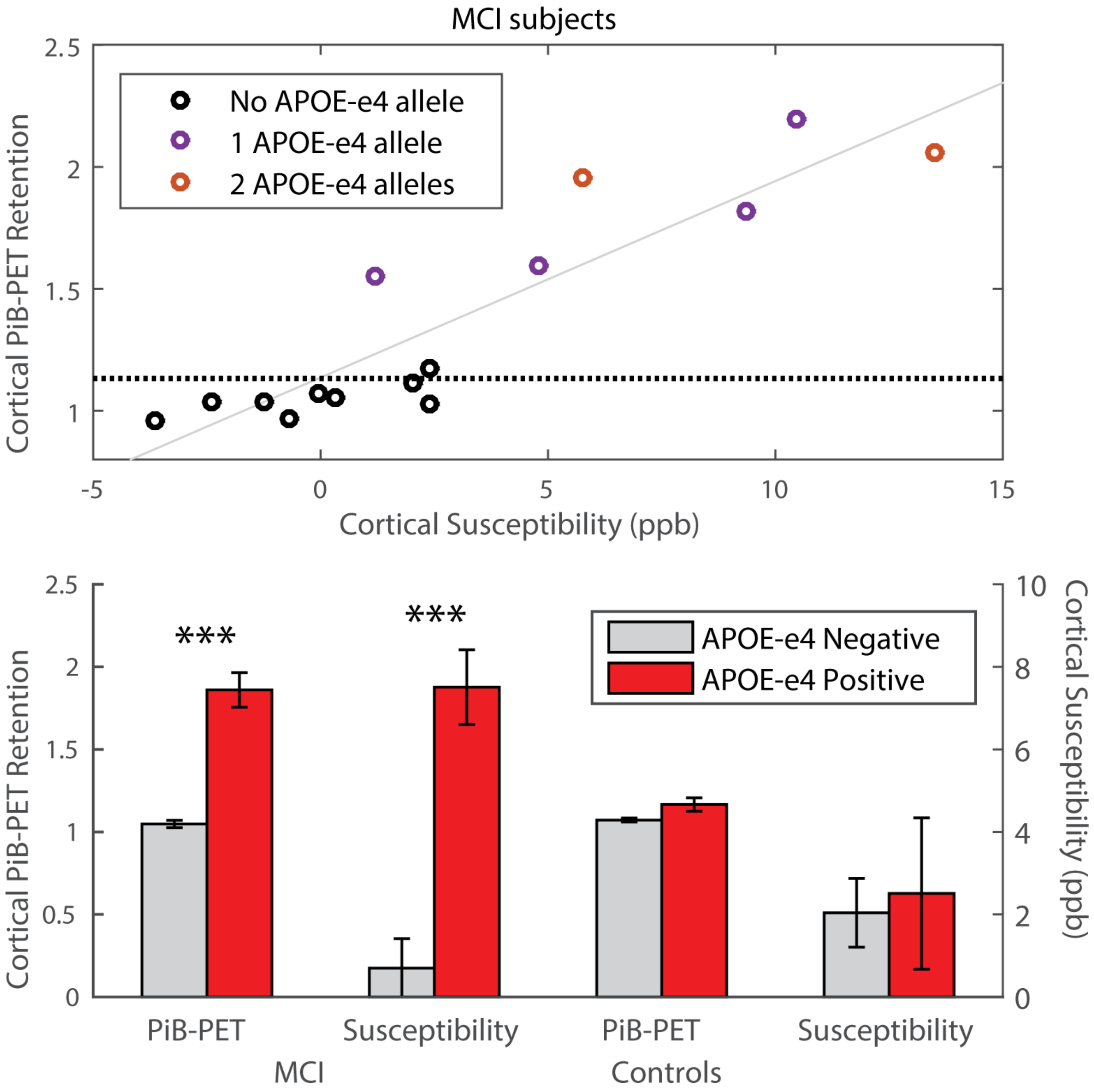

Figure 3: *Average Cortical PiB-PET Retention and Cortical Susceptibility of all MCI subjects (top) for the region with significantly increased coupling shown in* ***Figure 2****. The dotted line indicates the median split of the Cortical PiB-PET Retention of all subjects in the study, the trend line is indicated in gray (p<0.001, Spearman's rho=0.86,* R^2*-adjusted=0.80). Average Cortical PiB-PET Retention and Cortical Susceptibility for MCI subjects and controls when split based on APOE-e4 status (bottom), the error bars represent standard error. *** Significant difference between APOE-e4 positive and negative with p<0.001.*

7.5 Discussion

In this study magnetic susceptibility was used as a MRI-based measure of cerebral iron-load and combined with PiB-PET for measuring Aβ-plaque density in elderly subjects with normal cognition and MCI. For clarity and consistency with earlier studies, changes in susceptibility values will be referred to as changes in iron levels, due to the previously demonstrated correlation of susceptibility values with tissue iron levels in brain gray matter (Deistung, Schafer, et al. 2013; Lim et al. 2013; Langkammer et al. 2012; Schweser et al. 2012; Li, Wu, and Liu 2011). The main finding of our study is the characterization of brain regions affected by high iron in MCI, within which a spatial colocalization of Aβ-plaques and iron was observable. This effect was associated with increased genetic risk for AD-dementia. As this colocalization is consistent with neuropathologic accounts on AD-signature brain regions (Serrano-Pozo et al. 2011), our data may complement earlier considerations on the effect of cerebral iron on AD-risk (Ayton et al. 2015). To our knowledge this is the first report on a significant impact of iron on functional network integrity in subjects with MCI.

Although a previous smaller QSM-study reported higher iron-load in AD (Acosta-Cabronero et al. 2013), our data does not show a general effect for MCI when compared to controls (**Table 2**) indicating such differences might occur in later stages of AD progression. However, MCI subjects with the APOE-e4 allele did show significantly higher iron levels in the neocortex (**Table 3**), which is a brain region significantly affected by AD-pathology at early stages of disease progression (Serrano-Pozo et al. 2011). Our finding of increased cortical iron may therefore support earlier considerations that MCI in APOE-e4 carriers may represent a prodromal stage of AD (Sperling et al. 2015). Increased cortical iron may be a more specific correlate of emerging neuro-cognitive dysfunction in prodromal AD than cortical Aβ-plaque-load, which was in our data associated with APOE-e4 independently from MCI (**Table 3**). This may be consistent with earlier data from MRI phase experiments that indicate significant change only for MCI subjects that progressed to dementia (Kirsch et al. 2009) and considerations on synergistic effects of Aβ and other aspects of neurodegeneration in AD (Jagust 2016; Mormino, Betensky, Hedden, Schultz, Amariglio, et al. 2014). The fact that reduced volume of subcortical nuclei including the hippocampal area was associated with MCI but not APOE-e4 most likely reflects heterogeneity of possible causes for MCI in the elderly.

It has been shown that the T2-prep BOLD method can achieve comparable contrast-to-noise ratio (CNR) as the conventional echo-planar-imaging (EPI) based BOLD approach, but has much reduced signal dropout and image distortion especially in brain regions close to air cavities such as some frontal and temporal areas (Donahue et al. 2010; Hua et al. 2011; Rane et al. 2015). Such dropout and distortion are particularly problematic at 7T where magnetic susceptibility gradients increase substantially at air-tissue boundary. At 3T or lower fields, where most clinical scans are conducted, such EPI artifacts are much reduced. Therefore, the T2-prep BOLD fMRI method in this study at 7T was adopted and it is expected that the findings are generalizable to studies using conventional EPI BOLD fMRI sequences at 3T. For this study a seed based approach investigating functional connectivity of the MPFC was chosen, as the MPFC is a central component of the DMN, which has been demonstrated to be impaired by Aβ pathology already in the preclinical stage of AD (Mintun et al. 2006). Our findings of iron-load being associated with increased coupling in fronto-temporal brain regions is consistent with earlier reports on DMN-change in AD (Agosta et al. 2012; Damoiseaux et al. 2012) and thus indicate that increased iron may contribute to the dysfunction of cognitive brain networks in subjects at risk for AD. However, as the current study investigated combined effects of MCI and iron-load for definition of a brain region with particular liability for AD-associated brain change based on altered coupling to the MPFC (Buckner et al. 2009), our data does not support an independent role of iron for augmenting pathological decline in AD.

The reported correlation (**Figure 3**) between cortical iron and Aβ-plaque-load within these functionally altered brain regions suggest that increased cerebral iron relates to regional accumulation of Aβ in subjects at risk for AD and reflects preclinical neuronal dysfunction in AD-signature regions. Additionally, our finding of significantly higher levels of both iron and Aβ in APOE-e4 carriers is consistent with earlier reports and suggests that the APOE-e4 allele may confer susceptibility to AD via brain iron accumulation (Ayton et al. 2015).

Our data furthermore suggest that the co-occurrence of iron and Aβ may be mediated by APOE-e4, which has been demonstrated to both promote cerebral Aβ accumulation by competing for the same clearance pathways (Verghese et al. 2013) and increase cerebral iron retention by impaired lipoprotein trafficking due to low affinity of APOE-e4 to high-density lipoprotein (Ayton et al. 2015). While direct interactions between iron and Aβ may result in increased toxicity by production of redox-active iron forms and oxidative stress (Liu, Moloney, et al. 2011; Huang et al. 1999), brain iron accumulation is also associated with microglial over-activation (Zeineh et al. 2015), promoting neurodegeneration in AD (Mosher and Wyss-Coray 2014). Our observation of altered functional connectivity, may reflect these processes and thus indicate preclinical brain change with the potential of causing progressive neuronal damage, as reflected by worsening neurocognitive disorder. Although the sample size is small, the increased sensitivity at the high field strength of 7T with inherently better SNR in QSM, provides currently the most sensitive detection of in vivo gray matter iron levels (Langkammer et al. 2012). When interpreting the current data it needs to be taken into account that the QSM-signal is biased by decreased myelin density (Langkammer et al. 2012; Liu, Li, et al. 2011). However, the cortical and deep gray matter regions investigated in this study are low in myelin content and thus the myelin contribution to the susceptibility signal in this study was considered negligible. While spatial co-localization of microhemorrhages with Aβ-plaques may bias iron measures (Dierksen et al. 2010), in the current study no microhemorrhages were observable within the brain regions investigated.

Considering that iron may reflect processes associated with Aβ related neurocognitive dysfunction, further studies are needed to investigate whether the efficacy of therapeutic strategies lowering brain Aβ-plaque-load for slowing down progression of AD (Nitsch and Hock 2008; Winblad et al. 2014), should be complemented by iron-targeted medication (Crapper McLachlan et al. 1991; Wood 2015).

7.6 Acknowledgments

We thank all subjects for their study participation. We thank Linjing Mu, Ph.D. and Geoff Warnock, Ph.D. from the Division of Nuclear Medicine, University of Zürich, Switzerland for their help in generation of (11) carbon-labeled Pittsburgh Compound-B tracer for Positron-Emission-Tomography (Linjing Mu) and calculation of the cortical PiB ratio scores (Geoff Warnock). We thank Daniel Summermatter from the Division of Psychiatry Research and Psychogeriatric Medicine, University of Zürich, Switzerland, for help in interpretation of neuropsychological test results. This work was funded by the Swiss National Science Foundation (Schweizerischer Nationalfonds, SNF), the Clinical Research Priority Program (CRPP) of the University of Zurich on Molecular Imaging (MINZ), a grant from the National Institutes of Health (NIBIB) P41 EB015909, and institutional support from the Division of Psychiatry Research and Psychogeriatric Medicine, University of Zürich and Institute for Biomedical Engineering, University of Zürich and ETH Zürich, Switzerland.

8 Low cortical iron and high entorhinal cortex volume promote cognitive functioning in the oldest-old

J. M. G. van Bergen[1]*, X. Li[2,3], F. C. Quevenco[1], A. F. Gietl[1,4], V. Treyer[1,5], S. E. Leh[4], R. Meyer[1,4], A. Buck[5], P. A. Kaufmann[5], R. M. Nitsch[1,4], P. C. M. van Zijl[2,3], C. Hock[1,4], P. G. Unschuld[1,4]

[1] Institute for Regenerative Medicine, University of Zürich, Switzerland

[2] The Russell H. Morgan Department of Radiology and Radiological Science, Division of MR Research, The Johns Hopkins University School of Medicine, Baltimore, Maryland, USA

[3] F.M. Kirby Research Center for Functional Brain Imaging, Kennedy Krieger Institute, Baltimore, Maryland, USA

[4] Hospital for Psychogeriatric Medicine, University of Zürich, Switzerland

[5] Department of Nuclear Medicine, University Hospital Zürich and University of Zürich, Zürich, Switzerland

Extended from published work in Neurobiology of Aging (Van Bergen et al. 2017)

8.1 Abstract

The aging brain is characterized by an increased presence of neurodegenerative and vascular pathology. However, there is substantial variation regarding the relationship between an individual’s pathological burden and resulting cognitive impairment. To identify correlates of preserved cognitive functioning at highest age, the relationship between β-amyloid plaque-load, presence of small vessel cerebrovascular disease (SVCD), iron-burden and brain atrophy was investigated. 80 cognitively unimpaired participants (44 oldest-old, aged 85-96; 36 younger-old, aged 55-80) were scanned by integrated PET-MRI for assessing β-regional amyloid plaque-load (18F-Flutemetamol), white matter hyperintensities as an indicator of SVCD (FLAIR-MRI) and iron-load (Quantitative Susceptibility Mapping). For the oldest-old group, lower cortical volume, increased β-amyloid plaque-load, prevalence of SVCD and lower cognitive-performance in the normal range was found. However, compared to normal-old, cortical iron burden was lower in the oldest old. Moreover, only in the oldest-old, entorhinal cortex volume positively correlated with β-amyloid plaque-load. Our data thus indicate that the co-occurrence of aging-associated neuropathologies with reduced QSM-measures of cortical iron-load constitutes a lower vulnerability to cognitive loss.

8.2 Introduction

While advanced age is associated with substantial brain change and increased risk for cognitive decline, several studies on populations of older adults have revealed high levels of cognitive functioning despite considerable brain pathology. The resilience against such pathologies can be described as the brain's reserve; the cognitive and physiological properties that allow an individual to better tolerate age-related brain alterations and neuropathological burden before cognitive performance is impaired (Barulli and Stern 2013). Alternatively, maintained cognitive functioning could be attributed not to reserve, but to the presence of neuroprotective factors such as genetic variants, or alterations in clearance mechanisms that prevent the accumulation of neuropathologies at high age (Nyberg et al. 2012). Individuals in the age-group of 85 years and above ("oldest-old") are of particular interest when investigating both the relationship between manifest brain change and risk for Alzheimer's disease (AD) (Kawas et al. 2013), and potential physiological factors that promote resistance against age-related neuropathological burden (Nyberg et al. 2012; Rogalski et al. 2013). While Apolipoprotein E ε4 (APOE4) carrier-status is the strongest known risk factor for sporadic AD in the younger-old (Corder et al. 1993) and has been linked to increased β-amyloid plaque burden in the cognitively normal (Hollands et al. 2017), there also are reports suggesting no association of APOE4 status with incident dementia or compensatory reserve mechanisms in the oldest-old (Corrada et al. 2013; Garibotto et al. 2012).

Several studies have reported substantial discrepancies between measurable neuropathology and expected cognitive performance. This includes increased levels of β-amyloid plaques, which may reflect risk for future cognitive decline due to AD (Kawas et al. 2013; Sperling et al. 2009) and can be measured in cognitively healthy older adults (Mintun et al. 2006). In addition, regional atrophy was linked to AD-associated neurodegenerative brain change, typically affecting hippocampus and entorhinal cortex years before manifestation of cognitive decline (de Leon et al. 1989; Frisoni et al. 2010). The coexistence of β-amyloid plaques with other non-AD specific neurodegenerative alterations could indicate the greatest risk for progression to cognitive decline (Jagust 2016; Mormino, Betensky, Hedden, Schultz, Amariglio, et al. 2014). For example, small-vessel cerebrovascular disease (SVCD) is a frequent finding in cognitively healthy older adults, and relates to pathogenic markers of AD including β-amyloid plaque burden and regional atrophy, thus increasing risk for cognitive dysfunction (Guzman et al. 2013). Cerebral accumulation of iron is another neuropathological finding associated with aging, but also with neurodegenerative disorders including AD (Ayton et al. 2015; Ayton et al. 2017). Local iron accumulations in the vicinity of β-amyloid plaques may reflect both oxidative stress (Andersen, Johnsen, and Moos 2014; Meadowcroft et al. 2009; Rottkamp et al. 2001) and presence of activated microglia (Zeineh et al. 2015). Additionally, activated proinflammatory microglia have been correlated to β-amyloid associated neurodegeneration and cognitive impairment (Serrano-Pozo et al. 2016; Fan et al. 2017), suggesting that in vivo measures of iron could indicate both oxidative stress and β-amyloid associated neurodegeneration (van Bergen, Li, et al. 2016; Derry and Kent 2017; Ayton et al. 2017). While functional brain networks are altered at very early stages in AD and have been linked to Aβ-pathology (Buckner 2005; Sperling et al. 2009; Koch et al. 2014; Quevenco et al. 2017), they are also considered to provide means for neural compensation for pathological brain change during aging (Franzmeier et al. 2017; Marques et al. 2016; Steffener and Stern 2012).

State-of the art neuroimaging using multiple imaging modalities can provide in vivo information on various neuropathological burdens. Radioactive tracers may be used for measuring cerebral β-amyloid plaque burden by Positron-Emission-Tomography (PET) (Klunk et al. 2004; Vandenberghe et al. 2010). T1 weighted MRI is an established measure for regional atrophy in AD (Frisoni et al. 2010) and SVCD severity can be inferred from white matter hyperintensities (WMH), as measured by Fluid-Attenuated Inversion Recovery (FLAIR) MRI (Guzman et al. 2013). Recent developments on quantitative susceptibility mapping (QSM) techniques (Deistung, Schafer, et al. 2013; Li, Wu, and Liu 2011; Lim et al. 2013; Schweser et al. 2012) allow for in vivo measures of cerebral iron-load. Finally, functional connectivity (FC) measures can be assessed from BOLD functional MRI (fMRI) at rest and is an established measure of cognitive brain network integrity in a context of AD-pathology (Buckner 2005; Sperling et al. 2009; Koch et al. 2014).

While research on oldest-old populations may significantly advance knowledge on both protective and risk factors in AD and other age-related cognitive disorders (Kawas et al. 2013), not much is known on mechanisms that determine the relationship between presence of major neuropathologies and preserved cognitive functioning in the oldest-old. Aims of the current study therefore were 1.) to assess prevalence of aging-related brain change in a population of cognitively healthy older adults by assessing cerebral β-amyloid burden, differences in structural volume as an indicator of present neurodegenerative change, cerebral iron-load and the regional distribution of WMH as a proxy of SVCD; 2.) to characterize brain-physiology and neural mechanisms associated with preserved cognitive function, by assessing interactive relationships of pathological alterations and differences between cognitively healthy oldest-old and younger-old.

8.3 Methods

8.3.1 Participants

For the current study, two cohorts at the Hospital for Psychogeriatric Medicine and Institute for Regenerative Medicine (IREM), University of Zurich (UZH), Switzerland were combined resulting in a total sample of 80 healthy and cognitively unimpaired older adults. Within the recruited sample, two groups were compared: 36 "younger-old" (ages 55-80 years) and 44 "oldest-old" (ages 85-96 years) participants. Study procedures were in concordance with Human Research Act of Switzerland as well as with the declaration of Helsinki. Written informed consent was obtained from all participants before inclusion in the study.

Inclusion criteria were: preserved everyday functioning and no significant cognitive impairment, as assessed by the CERAD neuropsychological battery (Sotaniemi et al. 2012) and additional tests used in earlier studies of ours (van Bergen, Li, et al. 2016), including Mini Mental State Examination (MMSE), Verbal Learning and Memory Test (VLMT), Boston Naming Test (BNT), Trail Making Test B/A, and Stroop inference test. Exclusion criteria included: significant medication or drug abuse with possible effects on cognition, inability to partake MRI, MRI scans with the evidence of infection or infarction, clinically relevant changes in red blood cell count, serious medical or neuropsychiatric illness and significant exposure to radiation.

8.3.2 MRI data acquisition

All participants were scanned using a 3T GE SIGNA PET-MR whole-body scanner (GE Medical Systems, Milwaukee, WI, USA) equipped with an 8-channel head coil. T1-weighted BRAVO images (TI=450ms, voxel size=1x1x1mm3, flip-angle=12°, ASSET factor=2, scan time=6:00min) were acquired for anatomical referencing and automated image segmentation. MR phase measurements used for QSM calculation were acquired using a multi-echo 3D gradient recalled echo (GRE) sequence with 6 echoes (TR/TE1/ΔTE=40/6/4ms, voxel size=1x1x1mm3, flip angle=15°, bandwidth=±62.5 kHz, flow compensated, ASSET factor=2, scan time=7:53min). Phase data acquired with an echo time in the range of 18-26ms was used for QSM reconstruction. Images used to determine WMH were acquired using a CUBE FLAIR sequence (TR=6500ms, TE=134, ARC factor=2, voxel size=1x1x1.2mm^3, bandwidth=±31.25 kHz, scan time=6:07min). fMRI for the oldest-old was acquired at rest using a standard gradient echo EPI sequence (TR=2547ms, TE=13.8ms, voxel size=3x3x3mm3, flip angle=90°, ARC factor=2, duration=8:42min). fMRI as part of the study-protocol for the normal-old population was acquired separately with identical settings using a 3T GE SIGNA 750w whole-body scanner with a 32-channel head coil, as differences in head-coil channel-number have been demonstrated earlier to not significantly affect measured resting-state network connectivity (Paolini et al. 2015).

8.3.3 Assessment of structure volumes

To assess regional differences, the T1-weighted image was segmented using a multi-atlas matching approach consisting of 143 Regions of Interest (ROIs) developed as part of the Johns Hopkins University brain atlas. The atlas system is optimized for the parcellation of potential non-healthy brains by applying a Multiple-Atlas Likelihood Fusion algorithm and Ontology Level Control technology on the JHU multi-atlas sets (Djamanakova et al. 2014; Tang et al. 2013; Mori et al. 2016). Specifically, the atlas set of 26 participants aged between 50 and 90 years was used.

To normalize different brain sizes across participants, individual structural volume was corrected with the following approach: *Corrected structure volume = Original structure volume × (whole sample mean intracranial volume / participant intracranial volume)* (van Bergen, Li, et al. 2016). Twelve gray-matter ROIs were selected based on earlier reports on distribution of brain pathology at early stages of AD (Frisoni et al. 2010; Serrano-Pozo et al. 2011).

ROI-masks were eroded with two pixels to account for partial volume effects before being used as a mask to analyze average iron-load (QSM), β-amyloid burden and WMH detection. These imaging volumes were first re-sliced to the individual's T1 space, in which the atlas was defined, before further analysis.

8.3.4 Quantitative susceptibility mapping (QSM) for measuring brain iron-load

Multiple processing steps were performed to calculate from the acquired MR phase images the quantitative susceptibility maps of which local cerebral iron-load was assessed. First, phase unwrapping was performed using Laplacian based phase unwrapping (Li, Wu, and Liu 2011). A brain mask was then obtained by skull-stripping the GRE magnitude image acquired at TE of 14ms using FSL's brain extraction tool (BET, FMRIB Oxford, UK). The unwrapped phase images were then divided by 2π*TE to obtain an image of the frequency shift in Hz for each echo. Subsequently, background fields were eliminated with the sophisticated harmonic artifact reduction for phase data (SHARP) (Schweser et al. 2011) approach using a variable spherical kernel size with a maximum radius of 4mm and a regularization parameter of 0.05 (Schweser et al. 2011; Wu, Li, Guidon, et al. 2012). After removal of background fields, the resulting images of the three echoes were averaged to obtain a higher SNR as compared to single echo reconstruction (Wu, Li, Avram, et al. 2012). Inverse dipole calculations to obtain the susceptibility maps were performed using an iLSQR based minimization (Li et al. 2015). The means of the standard deviations of susceptibility in commonly accepted QSM reference regions, such as various white matter bundles and sections of the cerebrospinal fluid, were evaluated to select the region with the lowest mean standard deviations as the reference region (Deistung, Schafer, et al. 2013). For clarity and consistency with earlier studies, changes in susceptibility values will be referred to as changes in iron-load, due to the previously demonstrated correlation of susceptibility values with tissue iron-load in brain gray matter (Deistung, Schafer, et al. 2013; Li, Wu, and Liu 2011; Lim et al. 2013; Schweser et al. 2012).

8.3.5 Flutemetamol-PET for estimation of brain β-amyloid plaque burden

Flutemetamol-PET was used to estimate individual local brain β-amyloid plaque burden (Vandenberghe et al. 2010). Individual dose of 140MBq of Flutemetamol was injected into the cubital vein. Time-of-flight algorithm including necessary corrections were applied to reconstruct the PET-images. Standard MRAC images were used to derive attenuation correction maps according standard implemented algorithms. Late frame (minutes 85-105) values were standardized by the cerebellar gray matter value (Vandenberghe et al. 2010), resulting in 3D-volumes of Flutemetamol retention as an estimate of β-amyloid burden via standard uptake value ratios (SUVR) (matrix=256x256x89, voxel size=1.2x1.2x2.78mm^3).

Single measures of individual cortical β-amyloid burden and iron-load were calculated for each participant based on average gray-matter ROI values of Flutemetamol-SUVR and susceptibility, respectively, as reported earlier (van Bergen, Li, et al. 2016). To determine "amyloid-positive" status the Flutemetamol-SUVR cutoff value of 1.562 was used (Vandenberghe et al. 2010).

8.3.6 Assessment of SVCD by semi-automated WMH detection

To assess general occurrence of WMH, each participant’s FLAIR images were segmented into gray matter and major white matter regions using the previously generated atlas. The WMH in each white matter region were automatically identified by segmenting and grouping voxels with intensities 1.5 standard deviation above the average gray matter intensity of each participant (Iorio et al. 2013). Automatically segmented regions were then manually validated, for example to only count a WMH in one region when it extended with a small number of voxels into a second white matter region. The SVCD-burden was inferred on by summing the number of regions exhibiting WMH.

8.3.7 Local correlation analysis

For each of the selected ROIs, WMH score and regional volume were used as outcome variables with local β-amyloid burden and local iron-load as predictors, while controlling for age and gender. To investigate differences in the correlation effects between oldest-old and younger-old, Fisher’s r-to-z transformation was applied on the correlation coefficients within each region for each group (Fisher 1921). False Discovery Rate (FDR) correction for multiple testing (Benjamini and Hochberg 1995) was applied to the p-values of all regions for each predictor-outcome pair and results were found significant when p-FDR-corrected < 0.05. All statistical tests were performed in MATLAB R2016b (Mathworks, Natick, MA).

8.3.8 Functional connectivity analysis

Pre-processing of fMRI data was performed using SPM12 (http://www.fil.ion.ucl.ac.uk/spm/). To investigate differences in FC between oldest-old versus normal-old and the respective effects of Aβ-plaque-density, iron-load and SVCD on oldest-old versus normal-old status, these measures were used as covariates in group level covariate analysis of seed-to-voxel FC of the medial prefrontal cortex (MPFC) and posterior cingulate cortex (PCC) region using the CONN-toolbox (Whitfield-Gabrieli and Nieto-Castanon 2012) ($p<0.001$, cluster threshold p-FDR-corrected<0.05). The signal was filtered with a band-pass filter (0.008–0.09 Hz). Motion parameters, cerebrospinal fluid, and white matter were regressed out as variables of no interest.

8.4 Results

8.4.1 Characteristics of the studied populations and neuropsychological performance.

Demographic information for the investigated study populations and neuropsychological test performance at time of inclusion are summarized in **table 1**. The average education level, as measured by years of formal education, was significantly lower in oldest-old compared to younger-old (oldest-old: 14.2 (2.8) years; younger-old: 15.9 (2.6), p=0.010). Clinical examination revealed self-reliance and absence of cognitive impairment in the oldest-old group. However, they performed significantly lower than the younger-old group in all administered neuropsychological tests except CERAD word list recognition (**table 1B**). Eleven out of 36 younger-old (31%) and six out of 44 oldest-old (14%) were APOE4 carriers. Fisher test on the odds ratio of an APOE4 carrier having oldest-old status resulted in a non-significant trend (*p*=0.071, CI=0.11-1.09).

	Whole sample	***Younger-old***	***Oldest-old***
A) Demographics			
N (M/F)	80 (54/26)	36 (21/15)	44 (33/11)
Age	79.20 ± 11.80	67.75 ± 7.75	88.57 ± 2.69 **
Education	14.99 ± 2.85	15.92 ± 2.61	14.23 ± 2.84 **
ApoE-e4 carriers (%)	17 (21%)	11 (31%)	6 (14%)
B) Neuropsychology			
MMSE	28.99 ± 1.10	29.44 ± 0.81	28.60 ± 1.17 **
VLMT: delayed recall	7.93 ± 3.99	8.58 ± 3.93	7.43 ± 4.02 **
Boston Naming Test	14.43 ± 0.77	14.73 ± 0.45	14.21 ± 0.89 **
Trail making test B/A	2.61 ± 1.41	2.17 ± 0.70	2.98 ± 1.71 **
CERAD: Word list recall	6.99 ± 1.93	7.79 ± 1.32	6.36 ± 2.12 **
CERAD: Word list recognition	9.77 ± 0.65	9.76 ± 0.61	9.78 ± 0.69
CERAD: Word list learning	8.23 ± 1.39	8.82 ± 0.98	7.76 ± 1.49 **
CERAD: Fluency	21.54 ± 6.91	24.36 ± 5.61	19.37 ± 7.08 **
Stroop Interference: color-word	32.60 ± 11.26	27.91 ± 7.50	36.48 ± 12.40 **

Table 1*: Overview of sample A) demographics and B) neuropsychological test performance measures as mean ± STD. * = significant difference (two-sample T-test) between the oldest-old and younger-old with $p < 0.05$, ** = $p < 0.01$ and *** = $p < 0.001$.*

8.4.2 Prevalence of neuropathological burden in oldest- versus younger-old.

While corrected structure volume in cortical gray matter regions and the hippocampus was significantly lower in oldest-old compared to younger-old, no significant difference could be observed for the entorhinal cortex (**figure 1A**, **table 2A**). The cutoff for Flutemetamol SUVR (Vandenberghe et al. 2010) identified eight oldest-old and five younger-old participants as "amyloid-positive". Consistently, quantitative assessment of Flutemetamol SUVR indicated significantly higher regional β-amyloid plaque burden in the oldest-old than younger-old for all twelve investigated brain structures (**figure 1B**, **table 2B**). Deep frontal white matter was found to have the lowest average susceptibility standard deviations and was selected as a reference region to assess relative iron-load for each participant. Interestingly, iron-load in the oldest-old was significantly lower in neocortical regions, insula and posterior cingulate. Only in the putamen was iron-load higher in oldest-old than the younger-old (**figure 2, table 2C**). Almost all oldest-old exhibited substantial SVCD upon visual inspection, which is reflected by significantly higher (p=0.0002) SVCD in oldest-old (6.59 ± 0.62) compared to younger-old (2.36 ± 0.29, **table 2C)**. For assessment of effects accountable to age, a 1-way MANCOVA with age as covariate was used to compare neuropsychological test scores, volume, cortical β-amyloid burden, cortical iron and SVCD between oldest-old and younger-old. Here, a significant effect after correction for age could only be observed for prevalence of SVCD (*p*=0.034, t=4.670).

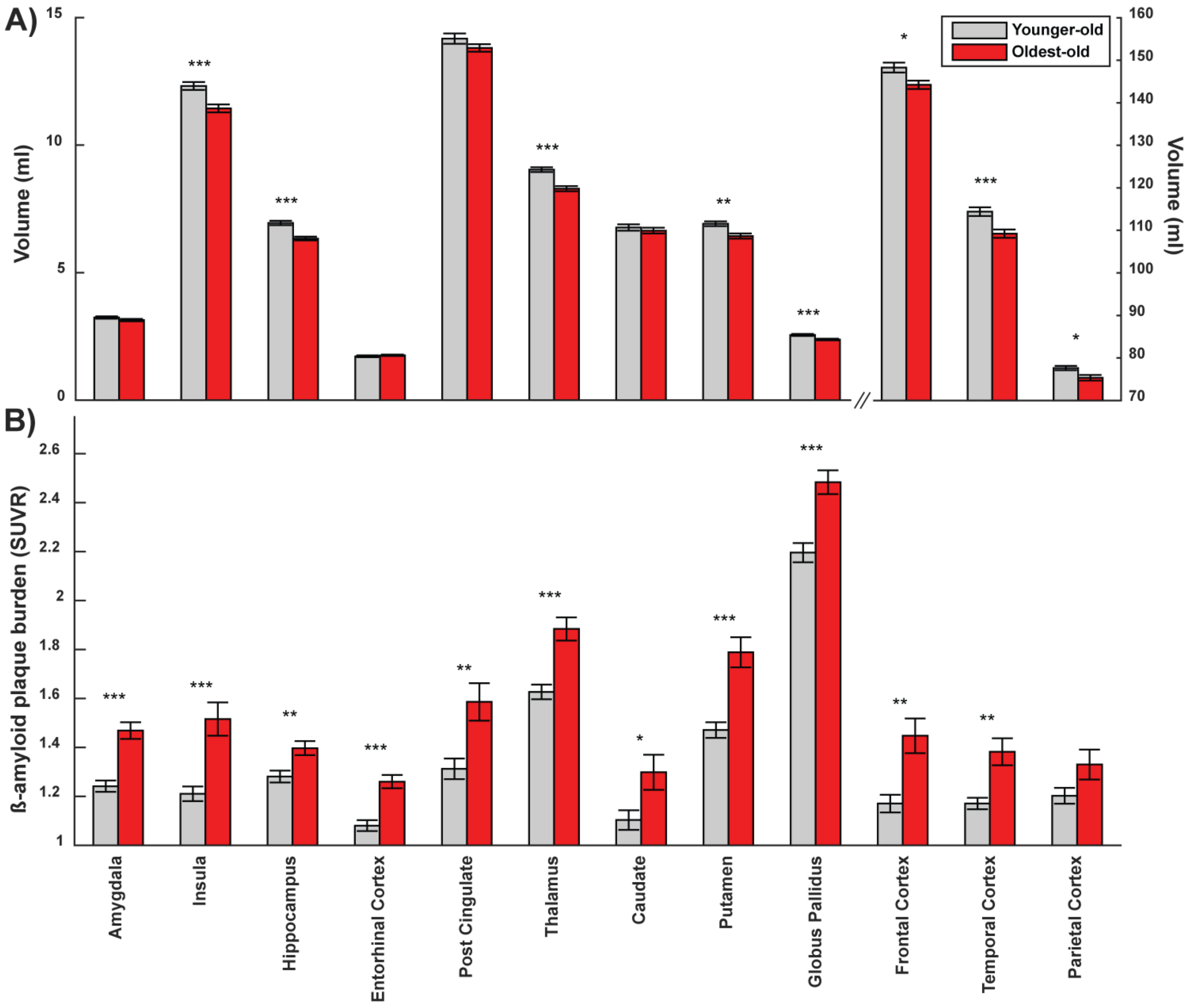

Figure 1: *Mean regional average values (SEM) per group for* ***A)*** *volume (ml),* ***B)*** *β-amyloid plaque burden (18F-Flutemetamol SUVR). Significant differences after FDR-multiple-testing-correction are indicated by * = p < 0.05, ** = p < 0.01 and *** = p < 0.001.*

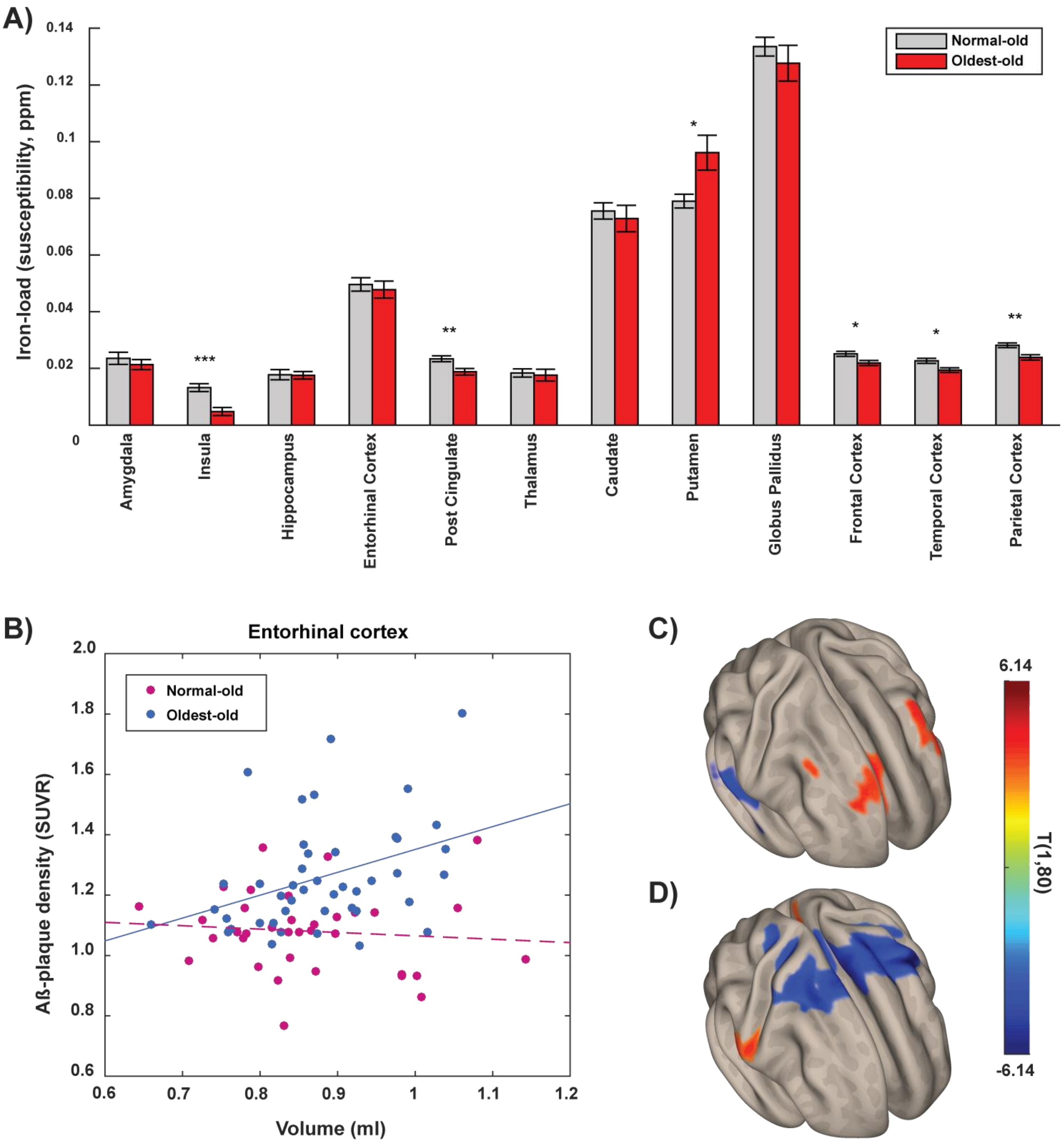

Figure 2A) *Mean regional average values (SEM) per group for iron (susceptibility, ppm). Significant differences after FDR multiple testing correction are indicated by * = p < 0.05, ** = p < 0.01 and *** = p < 0.001.* ***2B)*** *Scatterplot for correlations between entorhinal volume (ml) and entorhinal Aβ-plaque-density for oldest-old (r=0.39, p=0.01), normal-old r=-0.09, p=0.59.* ***2C)*** *Main effects for regional differences in FC between oldest-old and normal-old as measured using the MPFC and PCC (only overlaid T(1,80) > 3.41, indicating p < 0.001) (**2D**).*

	Statistics, correlation analysis	
	β-amyloid plaque burden	***Iron-load***
A) Regional volume		
Amygdala	p=0.01 r=0.28 *	p=0.94 r=-0.03
Insula	p=0.99 r=0.00 †	p=0.02 r=0.28 *
Hippocampus	p=0.55 r=-0.08	p=0.74 r=0.06
Entorhinal Cortex	p=0.08 r=0.21 †	p=0.01 r=-0.30 *
Frontal Cortex	p=0.99 r=0.00	p=0.54 r=0.09
Temporal Cortex	p=0.34 r=0.12	p=0.10 r=0.19
Parietal Cortex	p=0.18 r=-0.16	p=0.03 r=0.26 *
Occipital Cortex	p=0.99 r=-0.02	p=0.68 r=0.06
Neocortex	p=0.90 r=-0.04	p=0.11 r=0.19
B) SVCD (WMH-scores)		
Amygdala	p=0.06 r=0.22	p=0.07 r=-0.22
Insula	p=0.07 r=0.22	p=0.42 r=-0.12
Hippocampus	p=0.99 r=0.01	p=0.98 r=0.04
Entorhinal Cortex	p=0.05 r=0.23 *	p=0.05 r=-0.24 *
Frontal Cortex	p=0.05 r=0.23 *	p=0.06 r=-0.23
Temporal Cortex	p=0.17 r=0.17	p=0.03 r=-0.26 *
Parietal Cortex	p=0.23 r=0.16	p=0.01 r=-0.29 *
Occipital Cortex	p=0.48 r=0.11	p=0.12 r=-0.19
Neocortex	p=0.11 r=0.20	p=0.03 r=-0.26 *

Table 2: *Regional correlation analysis for A) volume and B) SVCD with the respective local β-amyloid plaque burden and iron-load. Indicated are values for the entire sample (n=80), * indicates a significant correlation with p-FDR-corrected < 0.05; † = significant differences in regressions slopes between oldest-old and younger-old using Fisher r-to-z transformation, with $p < 0.05$.*

	Statistics, pathology-measures by group		
	Whole sample	***Younger-old***	***Oldest-old***
A) Volume (ml)			
Amygdala	3.19 ± 0.04	3.24 ± 0.05	3.14 ± 0.05
Insula	11.83 ± 0.12	12.32 ± 0.15	11.44 ± 0.16 ***
Hippocampus	6.61 ± 0.07	6.95 ± 0.08	6.34 ± 0.08 ***
Entorhinal Cortex	1.74 ± 0.02	1.72 ± 0.04	1.76 ± 0.03
Post Cingulate	13.97 ± 0.12	14.18 ± 0.20	13.81 ± 0.15
Thalamus	8.63 ± 0.08	9.04 ± 0.09	8.29 ± 0.10 ***
Caudate	6.70 ± 0.08	6.77 ± 0.13	6.65 ± 0.11
Putamen	6.65 ± 0.07	6.91 ± 0.09	6.44 ± 0.10 **
Globus Pallidus	2.46 ± 0.03	2.56 ± 0.04	2.38 ± 0.03 ***

Frontal Cortex	146.07 ± 0.78	148.31 ± 1.16	144.24 ± 0.97 *
Temporal Cortex	111.56 ± 0.76	114.40 ± 1.02	109.24 ± 0.97 ***
Parietal Cortex	76.37 ± 0.45	77.64 ± 0.51	75.33 ± 0.66 *
B) β-amyloid plaque burden (18F-Flutemetamol SUVR)			
Amygdala	1.37 ± 0.02	1.24 ± 0.02	1.47 ± 0.03 ***
Insula	1.38 ± 0.04	1.21 ± 0.03	1.52 ± 0.07 ***
Hippocampus	1.35 ± 0.02	1.28 ± 0.02	1.40 ± 0.03 **
Entorhinal Cortex	1.18 ± 0.02	1.08 ± 0.02	1.26 ± 0.03 ***
Post Cingulate	1.46 ± 0.05	1.31 ± 0.04	1.59 ± 0.08 **
Thalamus	1.77 ± 0.03	1.63 ± 0.03	1.88 ± 0.05 ***
Caudate	1.21 ± 0.04	1.10 ± 0.04	1.30 ± 0.07 *
Putamen	1.65 ± 0.04	1.47 ± 0.03	1.79 ± 0.06 ***
Globus Pallidus	2.35 ± 0.04	2.20 ± 0.04	2.48 ± 0.05 ***
Frontal Cortex	1.32 ± 0.04	1.17 ± 0.04	1.45 ± 0.07 **
Temporal Cortex	1.29 ± 0.03	1.17 ± 0.02	1.38 ± 0.05 **
Parietal Cortex	1.27 ± 0.04	1.20 ± 0.03	1.33 ± 0.06
Neocortex	1.30 ± 0.03	1.19 ± 0.03	1.39 ± 0.06 **
C) Iron-load (susceptibility, ppm)			
Amygdala	0.022 ± 0.001	0.024 ± 0.002	0.021 ± 0.002
Insula	0.009 ± 0.001	0.013 ± 0.001	0.005 ± 0.001 ***
Hippocampus	0.018 ± 0.001	0.018 ± 0.002	0.018 ± 0.001
Entorhinal Cortex	0.049 ± 0.002	0.050 ± 0.002	0.048 ± 0.003
Post Cingulate	0.021 ± 0.001	0.023 ± 0.001	0.019 ± 0.001 **
Thalamus	0.018 ± 0.001	0.018 ± 0.001	0.018 ± 0.002
Caudate	0.074 ± 0.003	0.076 ± 0.003	0.073 ± 0.005
Putamen	0.088 ± 0.004	0.079 ± 0.002	0.096 ± 0.006 *
Globus Pallidus	0.130 ± 0.004	0.134 ± 0.003	0.128 ± 0.006
Frontal Cortex	0.023 ± 0.001	0.025 ± 0.001	0.022 ± 0.001 *
Temporal Cortex	0.021 ± 0.001	0.023 ± 0.001	0.019 ± 0.001 *
Parietal Cortex	0.026 ± 0.001	0.028 ± 0.001	0.024 ± 0.001 **
D) SVCD-burden (WMH regions identified)			
Whole brain	4.69 ± 1.80	2.36 ± 0.29	6.59 ± 0.62 ***

Table 3*: Overview of average structure volume, β-amyloid plaque burden, iron-load and WHM scores per region and group (mean ± SEM). Group-differences were investigated by independent-sample, two tailed T-test and FDR correction for multiple testing * = p < 0.05, ** = p < 0.01 and *** = p < 0.001.*

8.4.3 Relationship between β-amyloid burden, iron-load, structure volume and prevalence of SVCD.

Significant correlations (p-FDR-corrected<0.05) in the whole sample were found between β-amyloid burden and structure volume in the amygdala; and between iron-load and structure volume in insula, entorhinal cortex and parietal cortex (**table 3A**). Prevalence of SVCD correlated with β-amyloid burden in the entorhinal cortex and frontal cortex. Moreover, SVCD correlated negatively with iron-load in the amygdala, entorhinal cortex, parietal cortex and the neocortex as a whole (**table 3B**). When testing APOE4 carriers separately, significant correlations between β-amyloid burden and SVCD (*p*=0.01 r=0.80) and iron-load and volume (*p*=0.02 r=-0.60) could be observed in the entorhinal cortex.

8.4.4 Group-specific correlations of structure volume with β-amyloid burden.

Secondary, group specific regression-analysis indicated a significant correlation of high local β-amyloid burden with high structure volume in the entorhinal cortex of the oldest-old, which was not present in the younger-old (**figure 2B**, oldest-old *p*=0.01 r=0.39, younger-old *p*=0.59 r=-0.09) and insula (oldest-old *p*=0.04 r=0.31, younger-old *p*=0.31 r=-0.18), significant difference of correlations was confirmed by Fisher's r-to-z transformation (entorhinal cortex *p*=0.031, insula *p*=0.032).

To identify potential effects of education level, correlation analysis was performed with local structure volume and local β-amyloid burden as outcome variables and years of education as predictor, while controlling for age and gender. No significant correlation with years of education was found in any of the structures (**table 4**).

	Whole sample	***Younger-old***	***Oldest-old***
A) ***Volume (ml)***			
Amygdala	p=0.09 r=-0.21	p=0.68 r=-0.15	p=0.62 r=-0.14
Insula	p=0.15 r=-0.19	p=0.99 r=0.04	p=0.52 r=-0.16
Hippocampus	p=0.29 r=-0.15	p=0.09 r=-0.21	p=0.94 r=0.09
Entorhinal Cortex	p=0.07 r=-0.21	p=0.55 r=-0.17	p=0.92 r=-0.09
Post Cingulate	p=0.19 r=-0.18	p=0.99 r=0.08	p=0.35 r=-0.19
Thalamus	p=0.33 r=-0.15	p=0.92 r=0.11	p=0.83 r=-0.11
Caudate	p=0.16 r=-0.19	p=0.99 r=0.00	p=0.32 r=-0.20
Putamen	p=0.23 r=-0.17	p=0.66 r=0.15	p=0.55 r=-0.15
Globus Pallidus	p=0.25 r=-0.16	p=0.99 r=-0.07	p=0.99 r=-0.04
Frontal Cortex	p=0.14 r=-0.20	p=0.99 r=0.01	p=0.42 r=-0.18

Temporal Cortex	p=0.15 r=-0.19	p=0.99 r=0.01	p=0.46 r=-0.17
Parietal Cortex	p=0.19 r=-0.18	p=0.99 r=0.02	p=0.28 r=-0.21
Neocortex	p=0.13 r=-0.20	p=0.99 r=-0.02	p=0.40 r=-0.18
B) β-amyloid plaque burden (18F-Flutemetamol SUVR)			
Amygdala	p=0.99 r=0.03	p=0.90 r=-0.11	p=0.99 r=0.04
Insula	p=0.68 r=0.10	p=0.99 r=-0.06	p=0.99 r=-0.03
Hippocampus	p=0.99 r=0.04	p=0.86 r=-0.11	p=0.36 r=-0.19
Entorhinal Cortex	p=0.50 r=0.12	p=0.09 r=0.13	p=0.99 r=0.00
Post Cingulate	p=0.12 r=0.20	p=0.52 r=0.18	p=0.60 r=0.14
Thalamus	p=0.43 r=0.13	p=0.17 r=-0.21	p=0.83 r=0.11
Caudate	p=0.99 r=0.04	p=0.70 r=-0.14	p=0.66 r=0.13
Putamen	p=0.27 r=0.16	p=0.99 r=0.08	p=0.99 r=0.03
Globus Pallidus	p=0.45 r=0.13	p=0.99 r=0.01	p=0.99 r=0.00
Frontal Cortex	p=0.28 r=0.16	p=0.99 r=0.03	p=0.86 r=0.10
Temporal Cortex	p=0.38 r=0.14	p=0.57 r=0.16	p=0.92 r=-0.10
Parietal Cortex	p=0.99 r=0.06	p=0.99 r=0.08	p=0.88 r=-0.10
Neocortex	p=0.17 r=0.19	p=0.59 r=0.16	p=0.74 r=-0.12

Table 4: *Regional correlation between years of education and A) structure volume and B) local β-amyloid plaque burden.*

8.4.5 Functional connectivity analysis for group-differences and impact of neuropathological burden.

Significantly different connectivity patterns (*p*<0.001, cluster threshold p-FDR-corrected<0.05) were observed for the MPFC (18277 voxels) and PCC (12592 voxels), by seed-based, voxel-wise comparison of BOLD-synchronicity at rest of the normal- versus oldest-old group, allowing for both increased ("positive differences") and decreased connectivity ("negative differences"). For the MPFC seed, positive differences for a network comprising mainly cingulate gyrus, frontal pole, frontal gyrus, occipital gyrus and temporal pole regions, and negative differences for a network comprising mainly hippocampus, cerebellum and parts of the temporal gyrus resulted (**figure 2C**). Analysis of connectivity with the PCC seed indicated a network with positive differences in postcentral gyrus and precuneus, and negative differences in the precentral gyrus, cingulate gyrus and frontal gyrus (**figure 2D**). By separately adding covariates of the per-subject measures of neuropathological burden to the connectivity-term, a substantial share of total variance of FC difference between normal- and oldest-old could be explained (MPFC: 90.3%; PCC: 59.6%). The respective contributions of the included neuropathological measures to the model are indicated in **table 5**.

	A) MPFC: Voxels Explained	*% of Main Effect*	*B) PCC:* Voxels Explained	*% of Main Effect*
Main effect	18277	100%	12592	100%
Only Aβ-plaque-density	5303	29.0%	5741	45.6%
Only Iron-load	10441	57.1%	2313	18.4%
Only SVCD	14160	77.5%	6092	48.4%
Iron-load & SVCD	16100	88.1%	5305	42.1%
Aβ-plaque-density & SVCD	16082	88.0%	7315	58.0%
Aβ-plaque-density & Iron-load	13703	75.0%	5627	44.7%
Aβ-plaque-density & Iron-load & SVCD	16506	90.3%	7507	59.6%

***Table 5:** Seed based analysis using A) MPFC and B) PCC for functional connectivity differences between oldest-old and normal-old, allowing for effects (% of main effect) attributable to the covariates cortical Aβ-plaque-density, cortical iron-load and SVCD-burden. ($p<0.001$, cluster threshold p-FDR-corrected<0.05). The Main Effect for both MPFC and PCC is visualized in **Figure 2**.*

8.5 Discussion

By investigating a study population of cognitively unimpaired younger- and oldest-old by combined PET-MRI, we found significantly higher prevalence of neuropathological burden in the oldest-old, as reflected by cerebral β-amyloid burden, reduced volume of structures and higher prevalence of SVCD. While neuropsychological testing indicated generally lower performance levels in the oldest-old, they did not show significant cognitive impairment. Differences in the oldest-old furthermore included lower iron-load in cortical regions and an association of high entorhinal volume with entorhinal β-amyloid burden. Our findings support earlier considerations that distinct physiological brain properties may allow for maintained high cognitive functioning in the oldest-old, despite present brain pathology (Barulli and Stern 2013; Nyberg et al. 2012). To our knowledge, this is the first report indicating that reduced QSM measures of cortical iron-load constitute a lower vulnerability to loss of cognitive function at highest age.

amyloid-PET tracers, such as 18F-Flutemetamol (Vandenberghe et al. 2010), have become an established approach to estimate regional β-amyloid burden in AD-risk populations. Differences in brain structure volumes were investigated by applying a multi-atlas matching approach to T1-MRI data, using Likelihood Fusion and Ontology Level Control algorithms, as validated for both healthy and diseased study populations (Djamanakova et al. 2014; Tang et al. 2013). Recent efforts in validation of the QSM technology made it possible to quantitatively assess regional iron-load in vivo (Deistung, Schafer, et al. 2013; Langkammer et al. 2012) and assess iron in a context of neurodegenerative disease (van Bergen, Li, et al. 2016; van Bergen, Hua, et al. 2016; Acosta-Cabronero et al. 2013; Ayton et al. 2017). When interpreting the susceptibility data, it needs to be considered that the iron-load could vary on an inter-voxel basis and that QSM is biased by decreased myelin density (Langkammer et al. 2012; Liu, Li, et al. 2011). However, the cortical and deep gray matter regions investigated in this study are low in myelin content and thus the myelin contribution was considered minimal. FC analysis is a widely-used approach for assessing integrity of brain networks in a context of AD-risk and Aβ- pathology (Buckner 2005; Sperling et al. 2009; Koch et al. 2014). Distortion by processes of co-registration of PET with MR-indicators of neuropathological burden or bias due to changes occurring in the time between PET and MR acquisition could be avoided as the respective measures were acquired using an integrated PET-MR instrument.

When investigating the entire study sample, a significant relationship between β-amyloid burden and reduced volume resulted, which appears consistent with earlier reports on biomarker-associations in populations of older adults at risk for AD (Frisoni et al. 2010; Mormino, Betensky, Hedden, Schultz, Amariglio, et al. 2014). Our observation of SVCD correlating with β-amyloid burden concurs with earlier ADNI-findings (Guzman et al. 2013). Interestingly, we find negative correlations between iron and SVCD throughout the brain - which surprised us, as we expected SVCD to be associated with paramagnetic properties due to extravasated hemoglobin and vascular pathology. Our SVCD measure did not include the size but only the occurrence of WMH as a reflection of incidence of vascular breakdown. This limitation could affect the validity of the measure and as such the results at this point are only indicative. Additional studies are needed to validate the use of this score and investigate underlying effects of SVCD on iron, including the potential role of activated microglia and other iron clearing mechanisms in the cognitively healthy older adults with SVCD. Our finding of substantial neuropathological burden in the oldest-old is consistent with earlier studies on high aged populations (Kawas et al. 2013). In general, reduced structural volume and increased β-amyloid burden were more pronounced in the oldest-old than in the younger-old, in line with earlier findings of reduced volume as an indicator of incipient neurodegeneration and cognitive decline (Frisoni et al. 2010; Mormino, Betensky, Hedden, Schultz, Amariglio, et al. 2014; Dekhtyar et al. 2017). The oldest-old population in our study showed a generally lower cognitive performance than the younger-old, which appears consistent with earlier reports on non-pathological cognitive change during aging. Oldest-old status in our sample was associated with fewer years of formal education, which reflects the lower availability of higher-education in Switzerland during adolescence of the very old participants. It is not expected that formal education influence results at this stage of their life, this is supported by the lack of correlation between years of education and β-amyloid burden or structure volume. Additionally, we only found a non-significant trend regarding the effect of APOE4 status for the odds of being oldest-old versus younger-old. This finding could be due to insufficient power in our sample. Alternatively, it might be consistent with earlier reports that suggest other factors of brain physiology beyond APOE4 determine cognitive functioning at a very high age (Corrada et al. 2013; Garibotto et al. 2012). The fact that our oldest-old population exhibited a high degree of cognitive functionality despite present neuropathology concurs with earlier observations of preserved cognition at highest age (Nyberg et al. 2012; Rogalski et al. 2013). Considering the well-established relationship between high β-amyloid burden and risk for cognitive decline during aging (Jansen et al. 2015), our finding of significantly higher β-amyloid burden in cognitively unimpaired oldest-old participants suggests particular resilience against neuropathology. Here, our findings of lower iron-load in brain regions implicated in cognitive processes, such as the neocortex, posterior cingulate and insula, potentially reflect less neuronal damage. Pathological processes that are considered to be reflected by increased local iron-load include oxidative stress and presence of activated microglia (Meadowcroft et al. 2009; Nunez et al. 2012; Rottkamp et al. 2001; Zeineh et al. 2015; Serrano-Pozo et al. 2016). Moreover, increased iron-load is a frequent finding in neurodegenerative disease (Andersen, Johnsen, and Moos 2014; Kruer 2013). Increased iron-load in basal ganglia structures, particularly the putamen, are a known effect of aging (Hallgren and Sourander 1958; Bartzokis et al. 1997) and are consistent with the spatial distribution of our QSM measures of local iron-load. Our observation of low cortical iron-load in the cognitively unimpaired oldest-old might thus reflect lower vulnerability to age-related neuropathology, and may be consistent with reports of elevated brain iron being associated with mild cognitive impairment and liability for AD (van Bergen, Li, et al. 2016; Ayton et al. 2015; Ayton et al. 2017; Derry and Kent 2017). Furthermore, our findings are consistent with recently published data on a relationship between increased QSM measures of cerebral iron and β-amyloid associated cognitive decline (Ayton et al. 2017).

Several studies have investigated changes to the entorhinal cortex associated with aging and incipient AD, as indicated by reduced structural volume (de Leon et al. 1989; Frisoni et al. 2010), and found that increased structural volume of memory regions promotes maintained cognitive performance (Dekhtyar et al. 2017; deToledo-Morrell et al. 2004). Thus, while the current clinical study does not provide information on neurobiological mechanisms, the here reported positive relationship between entorhinal structural volume and β-amyloid plaque-density, which was only observable in the oldest-old, might indicate lower vulnerability. However, as entorhinal cortex volumes in the oldest-old did not differ from the younger-old, this finding needs to be interpreted with caution.

Finally, we found a significant difference in FC between oldest- and normal-old, observable for both the MPFC- and PCC-seed, which both serve as central hubs in cognition-related brain network activity. Our observations in cognitively healthy elderly appear consistent with earlier reports on regional extent of AD-related network changes (Buckner 2005; Sperling et al. 2009) and furthermore indicate distinct neural adaptation to accumulating Aβ-plaque-density, SVCD and iron-load.

Taken together, by investigating a cross-sectional sample of younger- and oldest-old, we provide neuroimaging-evidence that low cortical iron-load and high entorhinal volume despite high β-amyloid burden might characterize individuals less affected by aging-associated neuropathologies. Additional translational studies are needed to characterize the interplay between molecular mechanisms and genetic disposition that allows for maintained cognitive function at highest age. While our findings are consistent with recent reports on low iron burden as a predictor of preserved cognitive functioning in older adults (Ayton et al. 2017), therapeutic trials are needed to investigate whether these correlates of individual resilience may be exploited for specific disease modifying intervention.

8.6 Acknowledgments

We thank all participants for their study participation and Esmeralda Gruber for help with patient recruitment and study administration. This work was funded by the Swiss National Science Foundation (Schweizerischer Nationalfonds, SNF), the Mäxi foundation, the Clinical Research Priority Program (CRPP) of the University of Zürich on Molecular Imaging (MINZ), a grant from the National Institutes of Health (NIBIB) P41 EB015909, investigator initiated research support by GE-healthcare (114-2014-IIR-0075 and 114-2014-IIR-0076), and institutional support from the Institute for Regenerative Medicine (IREM), University of Zürich, Switzerland. This work was supported by the Zürich Impulse Program for the Sustainable Development of Mental Health Services.

9 Simultaneous Quantitative Susceptibility Mapping and Flutemetamol-PET reveals co-localization of iron and β-amyloid as a determinant of cognitive performance at high age.

J. M. G. van Bergen[1]*, X. Li[2,3], F. C. Quevenco[1], A. F. Gietl[1,4], V. Treyer[1,5], R. Meyer[1,4], A. Buck[5], P. A. Kaufmann[5], R. M. Nitsch[1,4], P. C. M. van Zijl[2,3], C. Hock[1,4], P. G. Unschuld[1,4]

[1] Institute for Regenerative Medicine, University of Zurich, Switzerland

[2] The Russell H. Morgan Department of Radiology and Radiological Science, Division of MR Research, The Johns Hopkins University School of Medicine, Baltimore, Maryland, USA

[3] F.M. Kirby Research Center for Functional Brain Imaging, Kennedy Krieger Institute, Baltimore, Maryland, USA

[4] Hospital for Psychogeriatric Medicine, University of Zurich, Switzerland

[5] Department of Nuclear Medicine, University Hospital Zurich and University of Zurich, Zurich, Switzerland

Submitted for peer-review to NeuroImage

9.1 Abstract

The accumulation of β-amyloid plaques is a hallmark of Alzheimer's disease (AD), and recently published data suggest that increased brain iron burden may reflect pathologies that synergistically contribute to the development of cognitive dysfunction. While preclinical disease stages are considered most promising for therapeutic intervention, the link between emerging AD-pathology and earliest clinical symptoms remains largely unclear. In the current study we therefore investigated the regional co-localization of iron and β-amyloid plaques, and their relationship to cognitive performance in healthy older adults.

116 older adults (mean age 75±7.4 years) received neuropsychological testing to calculate a global cognitive performance score incorporating major cognitive domains. All participants were scanned on a combined PET-MRI, including T1-sequences for anatomical mapping, quantitative-susceptibility-mapping (QSM) for assessing iron, and 18F-Flutemetamol-PET for estimating β-amyloid plaque-load. Biological parametric mapping (BPM) was used to generate masks indicating voxels with significant ($p\text{-}FDR<0.05$) correlation between susceptibility and 18F-Flutemetamol-SUVR.

We found a bilateral pattern of clusters with significant regional correlations between measured magnetic susceptibility and 18F-Flutemetamol-SUVR, indicating co-localized iron and β-amyloid plaques. For two bilateral clusters, located in the frontal and temporal cortex, significant relationships ($p\text{-}FDR<0.05$) between local β-amyloid and cognitive performance could be observed. No relationship between global β-amyloid burden and cognitive performance was observable.

Thus we report for the first time the effect of a co-localization of iron-load and β-amyloid plaques on the relation between regional β-amyloid plaque-load and cognitive performance in healthy older adults. Further studies are needed to clarify the pathological correlates of this local interaction of β-amyloid with iron.

9.2 Introduction

The accelerated accumulation of amyloid-beta (Aβ) into β-amyloid plaques is an early observable pathological hallmark of Alzheimer's Disease (AD) (Roberts et al. 2017) and recent studies have demonstrated a close relationship between the individual level of β-amyloid plaque burden and increased risk for AD (Jansen et al. 2015; Pietrzak et al. 2015). According to current hypothetical models, Aβ may trigger several downstream pathologies implicated in neurodegeneration, including aggregation of pathological tau, vascular damage and neuroinflammation (Sperling et al. 2011; Serrano-Pozo et al. 2016; Jagust et al. 2009; Dubois et al. 2016). Recent clinical trial data suggest that the therapeutic removal of β-amyloid may prevent cognitive decline, if performed early enough (Sevigny et al. 2016). However, novel diagnostic measures are needed to better understand the link between clinically silent AD pathology and first cognitive changes (Mortamais et al. 2017).

There are a number of clinical studies that demonstrate that the risk for cognitive decline due to AD-pathology is significantly increased by concurrent neurodegeneration (Jagust 2016; Mormino, Betensky, Hedden, Schultz, Amariglio, et al. 2014). Here, iron may provide useful information as recently published studies suggest a link between increased cerebral iron burden and AD related cognitive decline (Ayton et al. 2015; van Bergen, Li, et al. 2016; Ayton et al. 2017; Kim et al. 2017). Aβ in its monomeric and aggregated forms can bind iron, converting Fe^{3+} into Fe^{2+}, which builds up inside and on the border of the plaques (Everett et al. 2014; Derry and Kent 2017; Peters, Connor, and Meadowcroft 2015) possibly triggering ferroptosis (Dixon et al. 2012). Additionally, this process accelerates the extent and speed of aggregation from Aβ monomers into β-amyloid plaques (Peters, Connor, and Meadowcroft 2015; Everett et al. 2014). Iron associated with β-amyloid plaques has been commonly observed and could be a possible source of the observed oxidative damage in AD brains (Nunomura et al. 2001; Andersen, Johnsen, and Moos 2014; Meadowcroft et al. 2009; Rottkamp et al. 2001; Derry and Kent 2017). Furthermore, iron has also been observed in activated microglia surrounding β-amyloid plaques in the absence of microbleeds (Zeineh et al. 2015). Activated pro-inflammatory microglia have been correlated to β-amyloid associated neurodegeneration and cognitive impairment (Serrano-Pozo et al. 2016; Fan et al. 2017), suggesting that in vivo measures of iron may be able to indicate both oxidative stress and β-amyloid associated neurodegeneration (van Bergen, Li, et al. 2016; Ayton et al. 2017). Small-vessel cerebrovascular disease (SVCD) is a frequent finding both in AD and in populations at risk for AD, therefore local hemosiderin deposits resulting from vascular leakage may be another cause of local iron accumulation (Thal, Attems, and Ewers 2014; Young, Halliday, and Kril 2008; Guzman et al. 2013; Provenzano et al. 2013). Recent developments in quantitative susceptibility mapping (QSM) techniques (Deistung, Schafer, et al. 2013; Li, Wu, and Liu 2011; Lim et al. 2013; Schweser et al. 2012) allow for assessment of relative iron-load in vivo.

By using non-invasive susceptibility measures, we and others recently have demonstrated interactions between iron and β-amyloid pathology, that may predict longitudinal cognitive performance (Ayton et al. 2017; Derry and Kent 2017; Van Bergen et al. 2017; van Bergen, Li, et al. 2016). However, it still remains unclear, whether the interaction between iron and β-amyloid takes place on a global or local level, and also whether this interaction may be used to infer on the present cognitive status of healthy older adults. Therefore, this study cross-sectionally investigated a population of cognitively healthy older adults to 1) investigate region-specific correlations between changes in iron, measured by QSM, and β-amyloid plaque-load, measured by 18F-Flutemetamol-PET, on the voxel-level; 2) investigate whether susceptibility measures are associated with presence of SVCD, as a potential source of local iron-load changes; 3) determine if iron mediates the effect of β-amyloid plaque-load on cognitive performance in cognitively healthy older adults.

9.3 Methods

9.3.1 Participants

For the current study, two cohorts at the Hospital for Psychogeriatric Medicine and Institute for Regenerative Medicine (IREM), University of Zurich (UZH), Switzerland were combined resulting in a total sample of 116 healthy and cognitively unimpaired older participants. Study procedures were in concordance with Human Research Act of Switzerland as well as with the declaration of Helsinki. Written informed consent was obtained from all participants before inclusion in the study.

Inclusion criteria were: preserved everyday functioning and no significant cognitive impairment, as assessed by the CERAD neuropsychological battery (Sotaniemi et al. 2012) and additional tests used in earlier studies of ours (van Bergen, Li, et al. 2016; Van Bergen et al. 2017), including Mini Mental State Examination (MMSE), Verbal Learning and Memory Test (VLMT), Boston Naming Test (BNT), Trail Making Test B/A (TMT), and Stroop inference test.

Exclusion criteria included: significant medication or drug abuse with possible effects on cognition, inability to partake MRI, MRI scans with the evidence of infection or infarction, clinically relevant changes in red blood cell count, serious medical or neuropsychiatric illness and significant exposure to radiation.

To have a single measure indicating cognitive performance, neuropsychology results were converted to z-scores and averaged for the TMT, VLMT Delayed Recall, CERAD Fluency and Stroop Interference color-word tests. These tests were selected because they encompass cognitive domains that are affected early in individuals suffering from cognitive decline due to AD (Albert et al. 2011), such as verbal episodic memory, executive function and language function.

9.3.2 MRI data acquisition

All participants were scanned using a 3T GE SIGNA PET-MR whole-body scanner (GE Medical Systems, Milwaukee, WI, USA) equipped with an 8-channel head coil. T1-weighted BRAVO images (TI=450ms, voxel size=1x1x1mm3, flip-angle=12°, ASSET factor=2, scan time=6:00min) were acquired for anatomical referencing and automated image segmentation. MR phase measurements used for QSM calculation were acquired using a multi-echo 3D gradient recalled echo (GRE) sequence with 6 echoes (TR/TE1/ΔTE=40/6/4ms, voxel size=1x1x1mm3, flip angle=15°, bandwidth=±62.5 kHz, flow compensated, ASSET factor=2, scan time=7:53min). Phase data acquired with an echo time in the range of 18-26ms was used for QSM reconstruction. Images used to determine WMH were acquired using a CUBE FLAIR sequence (TR=6500ms, TE=134, ARC factor=2, voxel size=1x1x1.2mm^3, bandwidth=±31.25 kHz, scan time=6:07min).

9.3.3 Effects of structure volume

The T1-weighted image was segmented using a multi-atlas matching approach consisting of 143 Regions of Interest (ROIs) developed as part of the Johns Hopkins University brain atlas. The atlas system is optimized for the parcellation of potential non-healthy brains by applying a Multiple-Atlas Likelihood Fusion algorithm and Ontology Level Control technology on the JHU multi-atlas sets (Djamanakova et al. 2014; Tang et al. 2013; Mori et al. 2016). Specifically, the atlas set of 26 participants aged between 50 and 90 years was used.

To normalize different brain sizes across participants, individual structural volume was corrected with the following approach: *Corrected structure volume = Original structure volume × (whole sample mean* *intracranial volume / participant intracranial volume)* (van Bergen, Li, et al. 2016). To investigate possible relationships between structure volume and local β-amyloid plaque-load or local iron-load, twelve gray-matter regions of interest (ROIs) were selected from the generated atlas (Van Bergen et al. 2017) based on earlier reports on distribution of brain pathology at early stages of AD (Frisoni et al. 2010; Serrano-Pozo et al. 2011). ROI-masks were eroded with two pixels to account for partial volume effects before being used as a mask to analyze average iron-load (QSM) and β-amyloid burden. For each of the selected ROIs, structure volume was used as outcome variables with local β-amyloid burden and local iron-load as predictors, respectively. These and further correlation analyses in this work were corrected for age and gender after which False Discovery Rate (FDR) correction for multiple testing (Benjamini and Hochberg 1995) was applied to the resulting p-values in each instance.

9.3.4 Quantitative susceptibility mapping (QSM) for measuring brain iron-load

Multiple processing steps were performed to calculate from the acquired MR phase images the quantitative susceptibility maps of which local cerebral iron-load was assessed. First, phase unwrapping was performed using Laplacian based phase unwrapping (Li, Wu, and Liu 2011). A brain mask was then obtained by skull-stripping the GRE magnitude image acquired at TE of 14ms using FSL's brain extraction tool (BET, FMRIB Oxford, UK). The unwrapped phase images were then divided by 2π*TE to obtain an image of the frequency shift in Hz for each echo. Subsequently, background fields were eliminated with the sophisticated harmonic artifact reduction for phase data (SHARP) (Schweser et al. 2011) approach using a variable spherical kernel size with a maximum radius of 4mm and a regularization parameter of 0.05 (Schweser et al. 2011; Wu, Li, Guidon, et al. 2012). After removal of background fields, the resulting images of the three echoes were averaged to obtain a higher SNR as compared to single echo reconstruction (Wu, Li, Avram, et al. 2012). Inverse dipole calculations to obtain the susceptibility maps were performed using an iLSQR based minimization (Li et al. 2015). The means of the standard deviations of susceptibility in commonly accepted QSM reference regions, such as various white matter bundles and sections of the cerebrospinal fluid, were evaluated to select the region with the lowest mean standard deviations as the reference region (Deistung, Schafer, et al. 2013). For clarity and consistency with earlier studies, changes in susceptibility values will be referred to as changes in iron-load, due to the previously demonstrated correlation of susceptibility values with tissue iron-load in brain gray matter (Deistung, Schafer, et al. 2013; Li, Wu, and Liu 2011; Lim et al. 2013; Schweser et al. 2012).

9.3.5 Flutemetamol-PET for estimation of brain β-amyloid plaque burden

Flutemetamol-PET was used to estimate individual local brain β-amyloid plaque burden (Vandenberghe et al. 2010). Individual dose of 140MBq of Flutemetamol was injected into the cubital vein. Time-of-flight algorithm including necessary corrections were applied to reconstruct the PET-images. Standard MRAC images were used to derive attenuation correction maps according standard manufacturer implemented algorithms. Late frame (minutes 85-105) values were standardized by the cerebellar gray matter value (Vandenberghe et al. 2010), resulting in 3D-volumes of Flutemetamol retention as an estimate of β-amyloid burden via standard uptake value ratios (SUVR) (matrix=256x256x89, voxel size=1.2x1.2x2.78mm^3).

9.3.6 Biological Parametric Mapping (BPM)

To normalize the QSM and PET data of all participants to MNI space a multi-atlas matching approach developed as part of the Johns Hopkins University brain atlas was used. The atlas system is optimized for the parcellation of potential non-healthy brains by applying a Multiple-Atlas Likelihood Fusion algorithm and Ontology Level Control technology on the JHU multi-atlas sets (Djamanakova et al. 2014; Tang et al. 2013; Mori et al. 2016). To limit the analysis to gray matter, a mask was generated from the tissue maps generated during the normalization to MNI space. The images were smoothed using a 4 mm FWHM Gaussian kernel limited to the gray matter mask in SPM12 (http://www.fil.ion.ucl.ac.uk/spm/software/spm12) running under MATLAB R2016b (Mathworks, Natick, MA). The normalized PET and QSM images and the mask were then used as inputs for the Robust Biological Parametric Mapping toolbox (https://www.nitrc.org/projects/rbpm/) (Casanova et al. 2007; Yang et al. 2011a) running under MATLAB R2010b. The analysis was performed using the following settings: robust Huber regression analysis correcting for age and gender with proportional threshold set to 0.1. The results were tested using positive sign T-test, selecting voxels where the p-FDR-corrected<0.05 with a cluster-threshold of 100 voxels.

9.3.7 Assessment of SVCD by semi-automated WMH detection

To assess general occurrence of WMH, each participant's FLAIR images were segmented into gray matter and major white matter regions using the previously generated atlas. The WMH in each white matter region were automatically identified by segmenting and grouping voxels with intensities 1.5 standard deviation above the average gray matter intensity of each participant (Iorio et al. 2013). Automatically segmented regions were then manually validated, for example to only count a WMH in one region when it extended with a small number of voxels into a second white matter region. The SVCD-burden was inferred on by summing the number of regions exhibiting WMH.

9.3.8 Whole cortex- and local-effects analysis

Single measures of individual cortical β-amyloid burden and iron-load were calculated for each participant based on average gray-matter ROI values of 18F-Flutemetamol-SUVR and susceptibility, respectively, as reported earlier (van Bergen, Li, et al. 2016; Van Bergen et al. 2017). Clusters resulting from the BPM analysis were extracted and used as masks to extract regional iron-load changes and β-amyloid plaque-load. To identify "amyloid-positive" (*Aβ+*) or “amyloid-negative” (*Aβ-*) status based on single measures and regional gray matter 18F-Flutemetamol-SUVR values, the cutoff value of 1.562 was used (Vandenberghe et al. 2010). For each cluster, the combined neuropsychological score was compared between *Aβ+* and *Aβ-* using a 1-way MANCOVA with age and years of education as covariates. To investigate effects of APOE4, the analysis was also performed on APOE4 carriers and non-carriers separately.

To test the interaction of SVCD and iron-load, the cortical and regional iron-load was correlated with the WMH-score. All statistical tests were performed in MATLAB R2016b.

9.4 Results

9.4.1 Characteristics of the studied populations and neuropsychological performance.

Demographic information for the investigated study population and neuropsychological test performance at time of inclusion are summarized in **Table 1.** Clinical examination revealed self-reliance and absence of cognitive impairment for all participants. APOE4 carrier status was only available for 105 out of 116 participants, of those 105 there were 24 APOE4 carriers (22%).

A) Demographics	
N (M/F)	116 (69/47)
Age (min-max)	74.81 ± 7.52 (51-95)
Education	15.28 ± 2.76
ApoE-e4 carriers	24 (out of 105, 22%)
β-amyloid plaque-load (SUVR)	1.28 ± 0.32
amyloid-positive	18 (16%)
B) Neuropsychology	
MMSE	28.99 ± 1.10
Boston Naming Test	2.56 ± 0.75
Trail making test B/A	2.63 ± 1.26
VLMT: Delayed recall	8.51 ± 4.04
CERAD: Word list recall	7.32 ± 1.61
CERAD: Word list learning	8.31 ± 1.13
CERAD: Fluency	21.78 ± 6.34
Stroop Interference: color-word	31.90 ± 11.53

Table 1: *Overview of sample A) demographics and B) neuropsychological test performance measures as mean ± STD.*

9.4.2 Effects on structure volume

Significant negative correlation between structure volume and local β-amyloid plaque burden was found in the globus pallidus (p=0.001, **Table 2**). None of the cortical or memory regions showed significant correlations of volume with iron-load or β-amyloid plaque burden.

Correlation of structure size with:	**β-amyloid plaque burden**	***Iron-load***
Amygdala	p=0.22 r=0.17	p=0.78 r=-0.07
Hippocampus	p=0.82 r=0.03	p=0.21 r=0.17
Entorhinal Cortex	p=0.81 r=0.05	p=0.21 r=-0.17
Post Cingulate	p=0.82 r=0.04	p=0.97 r=0.01
Thalamus	p=0.80 r=-0.06	p=0.38 r=-0.13
Caudate	p=0.82 r=-0.02	p=0.21 r=-0.19
Putamen	p=0.53 r=-0.11	p=0.21 r=-0.18
Globus Pallidus	p<0.01 r=-0.36 *	p=0.96 r=-0.03
Frontal Cortex	p=0.43 r=0.13	p=0.96 r=0.02
Temporal Cortex	p=0.09 r=0.19	p=0.78 r=0.08
Parietal Cortex	p=0.80 r=-0.06	p=0.21 r=-0.17
Occipital Cortex	p=0.82 r=0.02	p=0.96 r=0.03

Table 2: *Regional correlation analysis for structure volume with the local β-amyloid plaque burden and iron-load. Indicated are values for the entire sample (n=116), * indicates a significant correlation with p-FDR-corrected < 0.05;*

9.4.3 Biological Parametric Mapping (BPM)

Deep frontal white matter was found to have the lowest average susceptibility standard deviations and was selected as a reference region to assess relative iron-load for each participant, with iron-load defined as the magnetic susceptibility in ppm relative to this region. The BPM analysis of correlation between iron-load (susceptibility) and β-amyloid plaque-load (18F-Flutemetamol-SUVR) resulted in 37 clusters of at least 100 voxels with p-FDR-corrected < 0.05. Graphical representation of the clusters is shown in **Figure 1** projected onto a 3D brain and on two exemplary axial slices. Additional axial slices throughout the whole brain can be seen in **Figure 2**. Alternatively, the number of significant voxels in brain regions are listed in **Table 3,** using the coarse region separation of the Hammers maximum probability atlas (Hammers et al. 2003). The strongest correlations were found in the basal ganglia structures. Many clusters were bilateral in nature and no differences were observed in number or size of clusters between hemispheres.

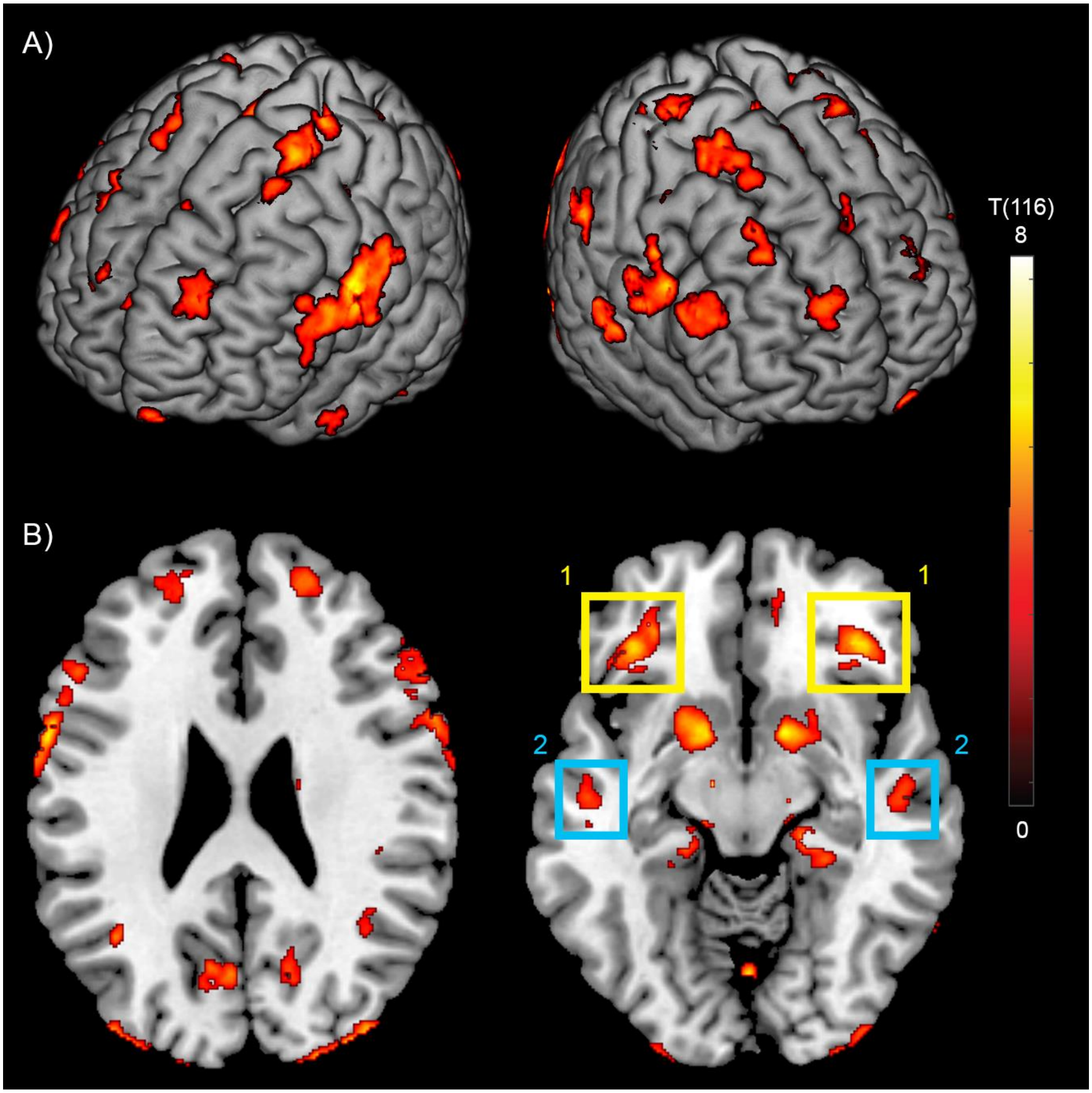

Figure 1: *Overlay of regions with significant correlation between iron-load (susceptibility) and β-amyloid plaque-load (18F-Flutemetamol-SUVR) with p-FDR-corrected<0.05 and a cluster-threshold of 100 voxels, on a 3D brain (A) and on two exemplary slices (B). Extracted β-amyloid plaque-load of regions (1) and (2) indicated in (B) identifies Aβ+ with significantly lower cognitive performance compared to Aβ- participants.*

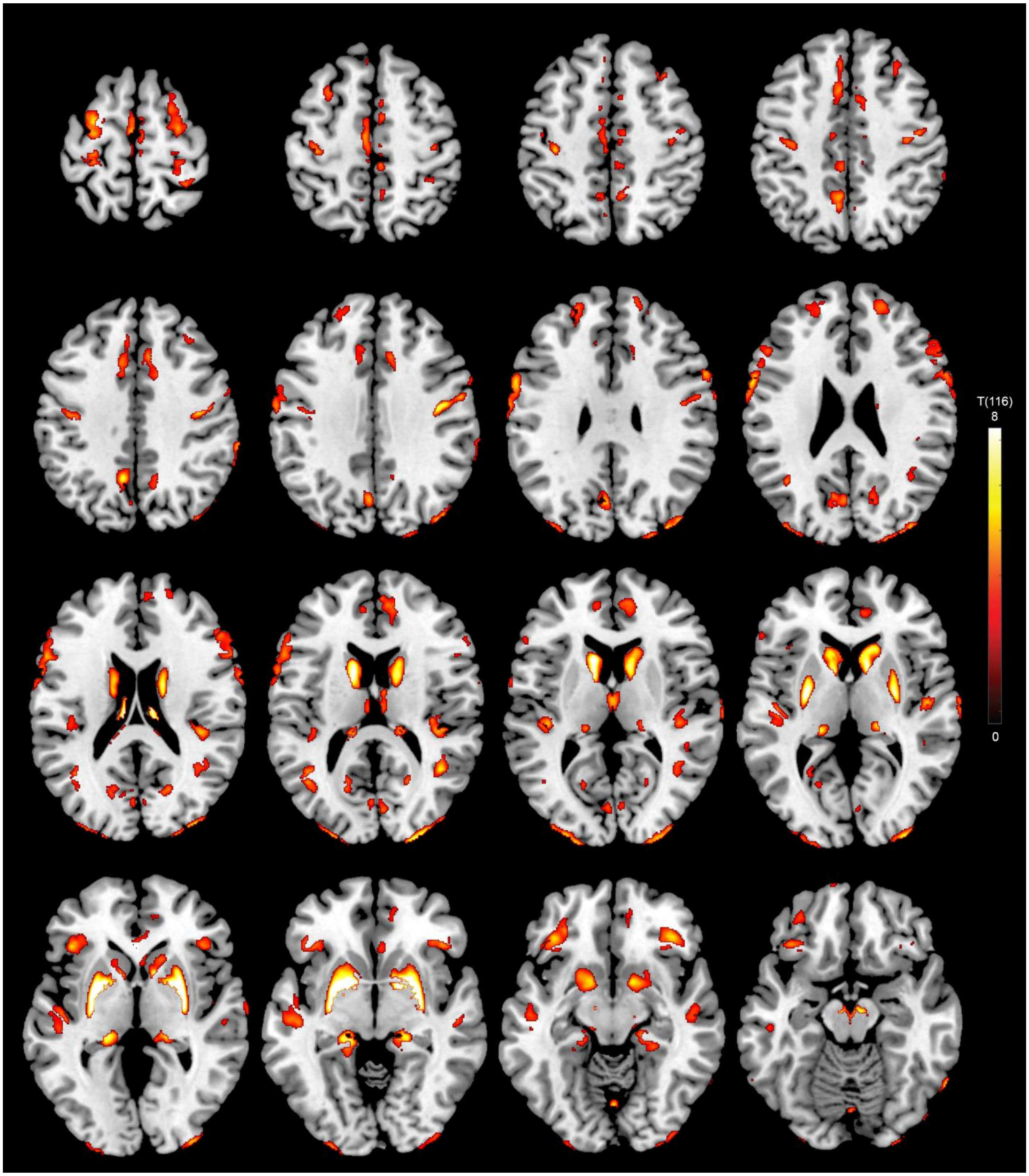

Figure 2: *Overlay of regions with significant correlation between iron-load (susceptibility) and β-amyloid plaque-load (18F-Flutemetamol-SUVR) with p-FDR-corrected<0.05 and a cluster-threshold of 100 voxels.*

Region #	Region Name	Voxels Significant	Percentage of Region
59	Superior frontal gyrus - Right	3690	8%
58	Superior frontal gyrus - Left	3378	7%
50	Precentral gyrus - Left	3258	11%
38	Putamen - Left	3076	74%
35	Caudate nucleus - Right	2879	77%
39	Putamen - Right	2786	69%
51	Precentral gyrus - Right	2661	9%
34	Caudate nucleus - Left	2519	69%
56	Inferior frontal gyrus - Left	2187	13%
62	Superior parietal gyrus - Left	2073	6%
12	Superior temporal gyrus, posterior part - Left	2065	17%
23	Lateral remainder of occipital lobe - Right	1545	4%
11	Superior temporal gyrus, posterior part - Right	1461	11%
31	Posterior temporal lobe - Right	1453	3%
57	Inferior frontal gyrus - Right	1328	8%
22	Lateral remainder of occipital lobe - Left	1297	3%
17	Cerebellum - Right	1295	2%
63	Superior parietal gyrus - Right	1205	3%
61	Postcentral gyrus - Right	1160	5%
33	Inferiolateral remainder of parietal lobe - Right	1076	3%
40	Thalamus - Left	1068	17%
60	Postcentral gyrus - Left	1053	4%
66	Cuneus - Left	893	11%
30	Posterior temporal lobe - Left	871	2%
41	Thalamus - Right	839	14%
29	Middle frontal gyrus - Right	836	2%
28	Middle frontal gyrus - Left	663	1%
67	Cuneus - Right	606	7%
18	Cerebellum - Left	568	1%
25	Cingulate gyrus (gyrus cinguli), anterior part - Right	530	7%
70	Lateral orbital gyrus - Left	512	16%
32	Inferiolateral remainder of parietal lobe - Left	473	1%
71	Lateral orbital gyrus - Right	420	11%
54	Anterior orbital gyrus - Left	417	7%
10	Parahippocampal and ambient gyri - Left	359	9%
43	Pallidum - Right	237	21%
72	Posterior orbital gyrus - Left	237	6%
14	Middle and inferior temporal gyrus - Left	235	1%
73	Posterior orbital gyrus - Right	228	5%
44	Corpus callosum	223	1%
42	Pallidum - Left	195	18%

19	Brainstem	156	1%
26	Cingulate gyurs (gyrus cinguli), posterior part - Left	152	2%
2	Hippocampus - Left	148	8%
13	Middle and inferior temporal gyrus - Right	135	1%
4	Amygdala - Left	131	10%
8	Anterior temporal lobe, lateral part - Left	123	4%
24	Cingulate gyrus (gyrus cinguli), anterior part - Left	110	2%
77	Subgenual frontal cortex - Right	110	10%
68	Medial orbital gyrus - Left	100	2%

Table 3: *Brain regions (Hammers maximum probability atlas, (Hammers et al. 2003)) included by voxel-clusters characterized by significant correlation between iron content (QSM) and A-beta plaque density (18F-Flutemetamol SUVR). Brain regions are ordered by the number of significant voxels.*

9.4.4 Whole cortex- and local cluster-effects analysis

The cutoff for 18F-Flutemetamol-SUVR (Vandenberghe et al. 2010) identified 18 participants (16%) "amyloid-positive" (*Aβ+*) and 98 “amyloid-negative” (*Aβ-*) based on whole cortex β-amyloid plaque-load. The Aβ+ participants that were identified using whole cortex β-amyloid plaque-load did not perform significantly worse than the Aβ- participants on the cognitive performance score (**Figure 3A**).

Out of the 37 clusters identified using the BPM analysis, two bilateral clusters in the frontotemporal cortex showed significantly lower cognitive performance scores in the *Aβ+* group that was identified using local cluster β-amyloid plaque-load (p-FDR-corrected < 0.05, clusters indicated in **Figure 1B**). In the frontal cortex cluster 8 participants with significant lower (p=0.012, **Figure 3B**) cognitive performance score were identified. Similarly, in the temporal cortex cluster 18 participants with significant lower (p=0.049, **Figure 3C**) cognitive performance were identified. APOE4 status did not split either the whole-cortex or regional β-amyloid plaque-load based Aβ+ or Aβ- groups into sub-groups with significant differences between sub-groups.

From the bilateral clusters in the frontal and temporal cortex regional iron-load and β-amyloid plaque-load measures are shown in **figure 4A and B**. The WMH-score did not correlate with whole cortex iron-load or the extracted iron-load from the two clusters (p > 0.05, **figure 4C and D**). Splitting these correlation analyses by APOE4 status did not result in significant different correlations when using Fisher’s r-to-z transformation on the correlation coefficients (Fisher 1921).

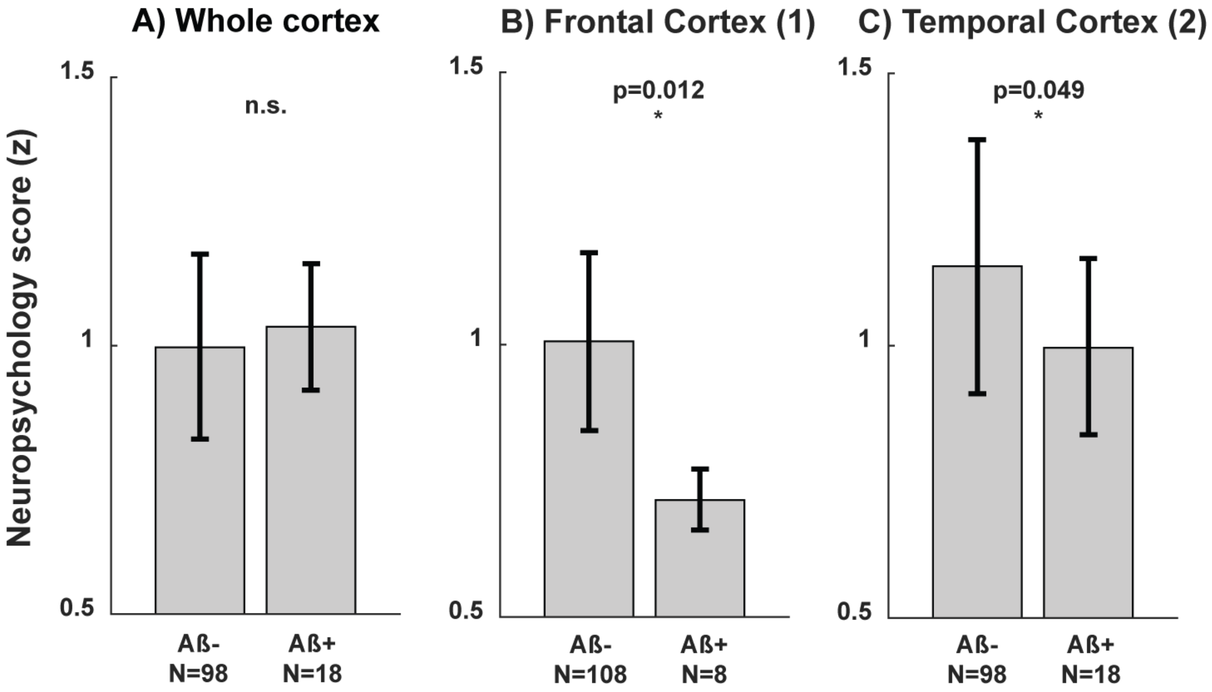

Figure 3: *Cognitive performance score for participants grouped as Aβ+ or Aβ- based on the -amyloid plaque-load (18F-Flutemetamol-SUVR) in the (A) whole cortex, (B) frontal cortex cluster and (C) temporal cortex. * = $p < 0.05$, n.s. = non-significant difference.*

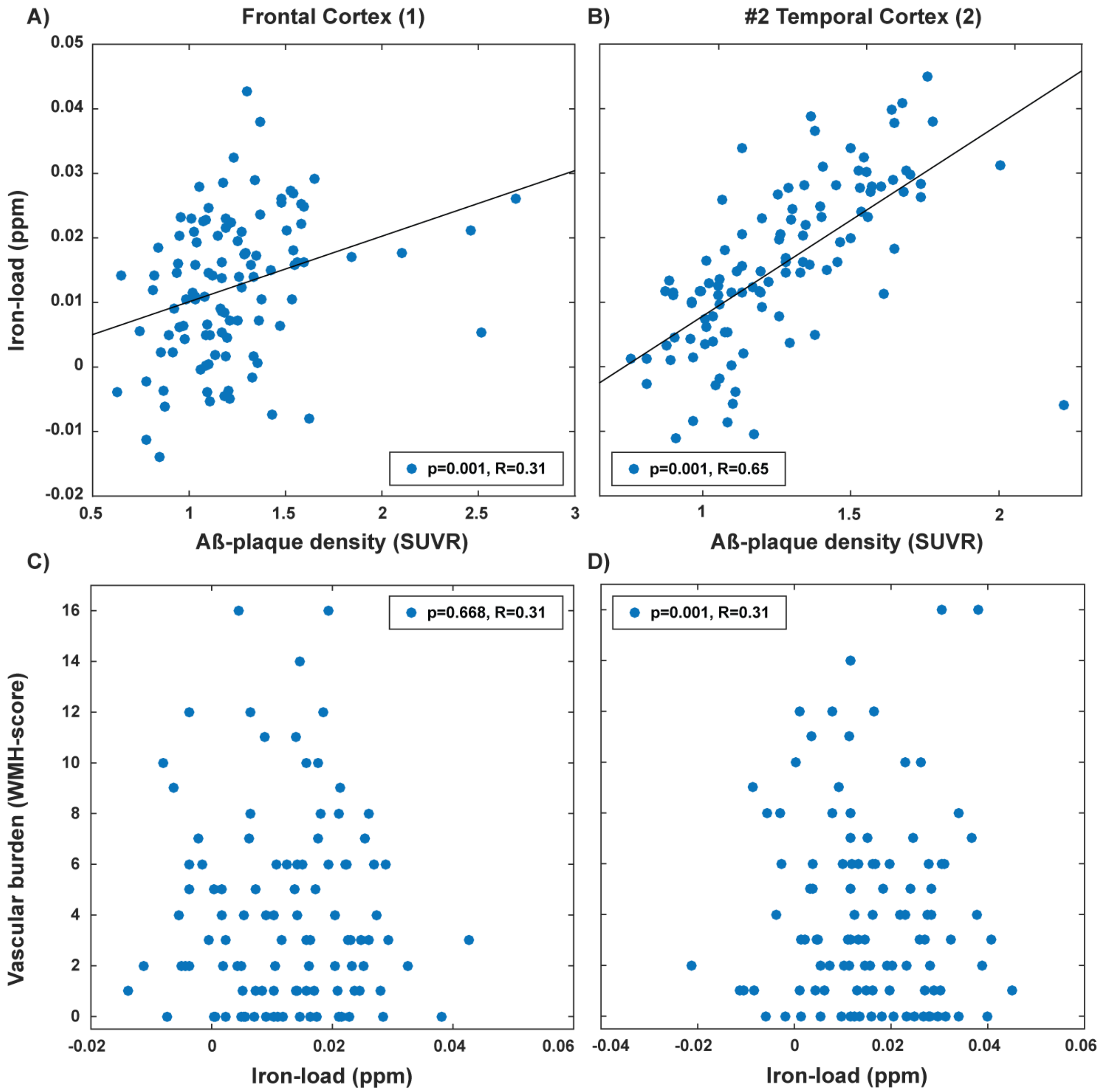

Figure 4: *Extracted iron-load (susceptibility) and β-amyloid plaque-load (18F-Flutemetamol-SUVR) for (A) frontal cortex cluster and (B) temporal cortex clusters found using BPM analysis. Non-significant correlation between vascular burden and iron-load in (C) frontal cortex cluster and (D) temporal cortex clusters.*

9.5 Discussion

In this study we investigated the co-localization and correlation of regional iron- and β-amyloid plaque-load by assessing neuroimaging markers in a voxel-based BPM analysis. We showed that strong correlations between iron-load and β-amyloid plaques are present in a bilateral pattern that particularly includes clusters located in the frontotemporal cortex and basal ganglia. Moreover, β-amyloid plaque-load in frontotemporal clusters was inversely associated with global cognitive performance scores. Interestingly, within these clusters, there was no association between SVCD and local susceptibility measures. To our knowledge this is the first study that shows the effect of a co-localization of iron-load and β-amyloid plaques on the relation between regional β-amyloid plaque-load and cognitive performance in healthy older adults. This co-localization of iron-load and β-amyloid plaques is consistent with earlier considerations on iron as a reflection of synergistic pathologies that promote β-amyloid-toxicity in vulnerable brain regions (Derry and Kent 2017; Ayton et al. 2017; Peters, Connor, and Meadowcroft 2015). As these findings were present in a cross-sectional sample, local susceptibility as a marker of the β-amyloid effects on cognitive performance might be used to separate disease stages.

Earlier studies by Ayton et al. that included longitudinal cognitive performance assessments (Ayton et al. 2017; Ayton et al. 2015; Derry and Kent 2017) indicate relevance of the association between iron and β-amyloid for cognitive decline and risk for AD. Brain regions affected by the here reported co-localization are consistent with regional effects reported earlier both for iron (Cho et al. 2016; Ayton et al. 2017) and general vulnerability for AD-pathology (Serrano-Pozo et al. 2011).

The relationships of structure volume in globus pallidus with β-amyloid plaque-load overlaps with the strongest region of correlation between β-amyloid plaque-load and iron-load found using the BPM analysis. When the data was not corrected for age, there was a significant negative correlation between iron-load and structure volume in the basal ganglia (p-FDR-corrected<0.05, data not shown) which seems to indicate both pathologies are, possibly synergistically, affecting this structures throughout the investigated age range. These findings are consistent with earlier observations of increased iron deposition in basal ganglia structures during aging (Hallgren and Sourander 1958; Bartzokis et al. 1997).

While only two bilateral regions showed the ability to differentiate low cognitive performers, these regions were located in cortical structures commonly affected by AD (Albert et al. 2011; Braak and Braak 1991).

No significant effect on cognition was observable for global β-amyloid burden in our study, similar to earlier reports of weak associations between β-amyloid plaque-load and cognition in cognitively healthy cross-sectional samples (Mortamais et al. 2017). However, our finding of significant effects of local β-amyloid in frontotemporal regions of cognitively healthy participants may be consistent with the spatio-temporal spread of disease pathology in neurodegenerative diseases (Brettschneider et al. 2015). As we only could observe the effect of β-amyloid on cognition when using iron to define the spatial clusters, iron might function as a mediating factor of β-amyloid plaque effects on cognition. Taking into account that β-amyloid plaque burden can be present in cognitively healthy older dults and reflects risk for progression to AD (Jansen et al. 2015), iron-load may be a potential marker for linking β-amyloid plaque burden to variation in cognitive performance, and thus may potentially be used to identify subtle dysfunction as very first manifestation of pre-clinical AD (Mortamais et al. 2017). While predictive value of QSM for cognitive decline has been demonstrated recently (Ayton et al. 2017; Kim et al. 2017), our current findings suggest informative value of local iron as a state marker of individual risk for cognitive decline due to cerebral amyloidosis.

Recent efforts in validation of the QSM technology make it possible to quantitatively assess regional iron-load in vivo (Deistung, Schafer, et al. 2013; Langkammer et al. 2012) and assess iron in a context of neurodegenerative disease (van Bergen, Li, et al. 2016; van Bergen, Hua, et al. 2016; Acosta-Cabronero et al. 2013; Ayton et al. 2017). When interpreting the susceptibility data, it needs to be considered that the iron-load could vary on an inter-voxel basis and that QSM is biased by decreased myelin density (Langkammer et al. 2012; Liu, Li, et al. 2011). Myelin loss could be substantial in the deep frontal white matter QSM reference region, however, myelin loss would increase average susceptibility in the reference region and thus lead to underestimation of the gray matter iron measures. The gray matter regions investigated in this study are low in myelin content and thus the myelin contribution in these regions was considered negligible and even potentially underestimated. Efforts were made to limit spillover of white matter signal of both QSM and 18F-Flutemetamol-SUVR images by performing the BPM analysis only in the gray matter, and selecting only clusters larger than 100 voxels. Optimized normalization to MNI space was performed to assure adequate input to the BPM analysis, but potential effects of the normalization process on the result cannot be fully excluded. However, distortion by processes of co-registration of PET with MRI images or bias due to changes occurring in the time between PET and MR acquisition could be avoided as the respective measures were acquired using an integrated PET-MRI.

Interestingly, we find no correlations between iron and SVCD throughout the brain, potentially confirming that the measured iron-load is not a measure of extravasated hemoglobin and vascular pathology. Considering earlier reports on iron containing activated microglia, and microglia as a promotor of β-amyloid plaque toxicity (Serrano-Pozo et al. 2016; Zeineh et al. 2015), local neuroinflammation might be an alternative explanation of our finding of elevated iron in the vicinity of β-amyloid plaques. However, the WMH-score used to infer upon SVCD in the gray matter is only based on occurrence of WMH and not size or specific location. This limitation could affect the validity of the measure and as such the results at this point are only indicative of potential effects of SVCD on QSM iron measures.

Previous work by us and others did show Aβ burden-related effects of APOE4 carriers status on iron measures in older populations with advancing cognitive impairment (van Bergen, Li, et al. 2016; Ayton et al. 2017). The fact that in the current study no significant effects of APOE4 were observable is most likely caused by a low number (all N<5) of APOE4 carriers in the Aβ+ groups, thus reducing statistical power. Additionally, the investigated sample showed no signs of cognitive impairment and spanned a large age-range which also could limit the effects of APOE4 status, as reported earlier (Corrada et al. 2013; Garibotto et al. 2012).

To conclude, in this cross-sectional study we have demonstrated that the co-localization of markers for iron and β-amyloid plaques characterizes brain regions where β-amyloid plaque-load inversely relates to the individual cognitive performance level. While the individual risk for AD-dementia has been demonstrated to relate to total β-amyloid burden (Roberts et al. 2017; Pietrzak et al. 2015), we here demonstrate a regional impact of β-amyloid on brain functionality characterized by iron-load in a non-demented older adult population. Further histological and molecular imaging studies are needed to characterize the interplay between iron and various other downstream pathologies that are possibly implicated in conferring local β-amyloid related neuronal damage.

9.6 Acknowledgments

We thank all participants for their study participation and Esmeralda Gruber for help with patient recruitment and study administration. This work was funded by the Swiss National Science Foundation (Schweizerischer Nationalfonds, SNF), the Mäxi foundation, the Clinical Research Priority Program (CRPP) of the University of Zurich on Molecular Imaging (MINZ), a grant from the National Institutes of Health (NIBIB) P41 EB015909, investigator initiated research support by GE-healthcare (114-2014-IIR-0075 and 114-2014-IIR-0076), and institutional support from the Institute for Regenerative Medicine (IREM), University of Zurich, Switzerland. This work was supported by the Zurich Impulse Program for the Sustainable Development of Mental Health Services.

10 Discussion

In this cumulative work we tried to investigate the role of iron in pre-clinical AD using neuroimaging markers. Neuroimaging iron measures and the associated post-processing were successfully implemented both at 7T and at the 3T PET-MRI. In the next sections, we will summarize for each of the previously postulated hypotheses what results were obtained.

10.1 Iron accumulation in human brains co-localizes with β-amyloid plaques in healthy and pre-clinical Alzheimer's disease subjects independent from iron accumulations due to microbleeds.

An important question in the field of iron-neuroimaging is the source of the measured iron-load signal. Iron sources can be either tissue-specific or hemosiderin leftovers of previously occurring microbleeds. In particular in the aging brain WMH are often found due pathological degradation of the vasculature. The WMH-score implemented for the current studies is intended as an indication of vascular integrity and as such the possible presence of deposits of extravasated hemoglobin. The current implementation is relatively crude and while it was not correlated to any of the iron-load measures, it cannot be concluded that the iron-load measures are not due to some form of microbleeds. The diagnostic value of WMH in pre-clinical and early stage AD has been investigated in several samples and results indicate a strong link between the two (Agosta et al. 2011; Esiri et al. 2015; Guzman et al. 2013; Holland et al. 2008; Provenzano et al. 2013; Yoshita et al. 2006; Young, Halliday, and Kril 2008). In general, the link between vascular dysfunction and AD is not only strong due to CAA but also because the most common risk factors for AD are related to the vasculature: APOE4 status, hypertension, hypotension, diabetes and hypercholesterolemia (Dickstein et al. 2010).

The WMH-score has given us an indication that the regional iron-load is not entirely dependent on vascular damage. Specifically, in the oldest-old population we found decreased cortical iron-load, despite their more than two-fold higher occurrence of WMH. Further research using histology is required to investigate the relationship between (white matter) vascular damage and QSM iron-load measures. However, previous studies have shown that abnormal iron accumulation and presence of iron within activated microglia also occurs in the absence of microbleeds (Zeineh et al. 2015; Meadowcroft et al. 2009). With these pathology findings and our oldest-old findings, there are enough grounds to interpret iron findings separate from vascular pathology.

We were the first to show correlations of neuroimaging markers in an MCI sample, using the enhanced data quality of 7T MRI (van Bergen, Li, et al. 2016). We repeated this at 3T using the PET-MRI, allowing for voxel-wise correlation (BPM) analysis that revealed strong bi-lateral clusters of co-localized iron and β-amyloid plaques. This is the first study of this scale that was able to detect these voxel-wise correlations due to the benefits of the PET-MRI, allowing for truly simultaneous assessment of iron and β-amyloid plaques.

Limiting factor in the analysis is that the neuroimaging markers used cannot differentiate between intercellular, extracellular or bound iron. Thus, within the measured imaging voxels that were 1x1x1mm3, the iron could be either inside microglia (Zeineh et al. 2015), stored in ferritin or bound to β-amyloid plaques (Rottkamp et al. 2001).

10.2 Iron accumulation co-localized with β-amyloid plaques in human brains negatively affects cognitive performance in healthy and pre-clinical Alzheimer's disease subjects.

While the individual risk for AD-dementia has been demonstrated to relate to total β-amyloid burden in some studies (Roberts et al. 2017; Pietrzak et al. 2015), the neurodegenerative and cognitive effects of this pathology do not correlate to cognitive performance in all individuals (Jansen et al. 2015). Build-up of β-amyloid plaque does not occur in all brain regions simultaneously, some regions are affected earlier than others and spread of pathology is faster between functionally connected regions (Thal, Attems, and Ewers 2014; Seeley et al. 2007; Seeley et al. 2009). This supports considerations that region specific measures of β-amyloid plaque-load could be more predictive of cognitive decline (Brettschneider et al. 2015).

Chronologically, we found the first evidence of the effect of co-localized iron and β-amyloid on cognitive performance in the 7T MRI results. Here subjects with a clinical diagnose of MCI showed local correlation between iron and β-amyloid plaque-load in a functionally affected region (see 10.3). However, the clinical diagnose of MCI is not limited to AD-MCI (Albert et al. 2011) and thus makes it hard to draw conclusions regarding the actual effects of iron in pre-clinical AD.

The first 3T project involving oldest-old participants without signs of cognitive decline revealed that lower cortical iron-load might play a role in their successful aging (Van Bergen et al. 2017). Of particular interest was the very high β-amyloid plaque-load in the oldest-old, which was for some subjects in the same range as normally seen in AD (Vandenberghe et al. 2010). While one cannot directly conclude that lower cortical iron has protected the oldest-old from AD-pathology, it can still be seen as a marker of lower inflammation and other active neurodegenerative processes (Andersen, Johnsen, and Moos 2014). Additionally, the lack of correlation between SVCD-burden and iron-load is a conformation that what we observed is potentially a real protective effect and not a simple consequence of SVCD. Apart from SVCD, many physiological factors (life-style, diet, blood pressure, medication, etc.) and non-physiological factors (formal education, cognitively challenging environments, etc.) might have influenced the brain's state at this highest age (Nyberg et al. 2012) and as such conclusions are still speculative. It is an intriguing result that warrants further exploration to clarify the factors that affect the build-up, clearance and downstream effects of cortical iron.

The larger sample BPM analysis added to the oldest-old results by showing that local β-amyloid plaque-load in clusters of strong correlation between iron and β-amyloid plaque, show significant differences in cognitive performance between Aβ+ and Aβ- subjects. In this same sample, using the cortical β-amyloid plaque-load did not result in significantly different performance between the two groups.

10.3 Iron accumulation in human brains correlates with changes in functional connectivity between brain regions measured by fMRI.

Changes in brain connectivity measured with fMRI have been identified in several studies, revealing large differences between AD and healthy controls but is also able to identify preclinical disease stages (Agosta et al. 2012; Binnewijzend et al. 2012; Damoiseaux et al. 2012; Franzmeier et al. 2016; Koch et al. 2012; Sheline and Raichle 2013; Sheline et al. 2010; Sperling et al. 2009; Steininger et al. 2014). The region of altered functional connectivity found in the 7T study reveals potential effects of iron on brain functioning. However, in that context it is hard to draw conclusions due to the ambiguity about what increased iron measures potentially reflect, specifically related to brain functioning. The location in the frontal cortex and the strong correlations between iron and β-amyloid plaques found in this region aligns with previous functional connectivity work that also implicate this region in early changes. The role of iron in changes to functional connectivity deserves further investigation, in order to separate other effects that could contribute to the observed changes.

An attempt was made to separate contributions of several pathologies (iron, β-amyloid and SVCD) on the functional connectivity changes in the oldest-old study. The results show that for different regions the impact of each pathology differs and that combinations of the three cover the majority of the difference. However, the differences between the two investigated networks in how much each pathology contributed was large. The interplay of the three investigated pathologies is likely large and thus such overlaps are to be expected. It would be challenging to find enough participants having only one of the pathologies to really separate each pathology for further studies. Previous studies investigating functional network changes of β-amyloid plaque-load did not look at other pathologies and are therefore also inherently limited (Rombouts et al. 2005; Sheline et al. 2010; Sperling et al. 2010; Steininger et al. 2014).

10.4 APOE-e4 genotype is associated with high β-amyloid plaque related iron accumulation.

The 7T study revealed significantly higher β-amyloid plaque-load and iron-load in the MCI subjects that were APOE4 positive. However, the sample was relatively small and similar differences were not observed in the larger 3T study. It could indicate that APOE4 status only in later stages of cognitive decline affects iron-loading, but APOE4 status does affect β-amyloid throughout life (Morris et al. 2010). Similar to our 3T study, the longitudinal study by Ayton et al. that investigate the effects of iron-load in more advanced cognitive decline did not show strong APOE4 effects on iron (Ayton et al. 2017). In several brain regions the study actually found the opposite effect: APOE4 positive status was associated with decreased iron-load, although this effect was not present in all brain regions and stages of cognitive decline (Ayton et al. 2017). Therefore, no claims of direct association of APOE4 with β-amyloid plaque related iron accumulation can be made at this point.

11 Conclusions and future directions

With the background summarized in the introduction (4.2) and knowledge obtained in this work there is ample evidence of a role of iron in AD pathology, both in disease progression and as a biomarker. Iron-load and β-amyloid plaque-load correlate throughout various brain regions, which could indicate both iron-bound iron and activated microglia, each in their own way influencing neuropathology. However, as this was neuroimaging based work we cannot excluded that the observed changes result from iron being only a downstream marker of β-amyloid plaque pathology. Alterations in iron seem to affect disease progression, with decreased iron-loading being linked to preserved cognition at higher age and increased iron with faster progression of cognitive decline (Ayton et al. 2017; Derry and Kent 2017).

With this in mind, the following questions arise for future investigations:

- **What is the relationship between iron and neuroinflammation?** TSPO-PET tracers are able to give readings on activated microglia in vivo (Fan et al. 2017). Combined TSPO-PET-MRI would be the ideal tool to investigate if the observed iron-load is actually a marker of activated microglia or plaque-bound iron. As activated microglia are also present around β-amyloid plaques, this should be combined with histological work in humans and animals. Additionally, investigating iron-load in vivo and on pathology after β-amyloid removal therapy (Sevigny et al. 2016) might also provide insights into location and effect of the measured iron.
- **Does local iron promote spread of neurodegenerative change in AD?** This question was partially answered by the work of Ayton et al. (Ayton et al. 2017; Derry and Kent 2017), but could benefit from longitudinal repeated amyloid-PET-MRI analysis. This would allow for a reading on β-amyloid plaque changes combined with associated iron-load changes and how they potentially shift during development of β-amyloid plaque pathology.
- **Does local iron promote spread of neurodegenerative change in AD?** The longitudinal repeated amyloid-PET-MRI analysis would also allow for in vivo inferences on the “chicken-and the egg” problem: does iron-loading promote AD-pathology, or does AD-pathology promote iron-loading?
- **Does the co-localization of iron with β-amyloid characterize a clinical subpopulation with distinct therapeutic needs?** It is very likely that regulation of iron and as such also dysregulation is subject-dependent. As described in the introduction (4.2), numerous proteins are involved in

handling of iron in the brain and thus can vary on an individual level. The lower levels of CSF ferritin in APOE4 carriers is a prime example of such differences (Ayton et al. 2015). Microglial activity, mobility or efficiency involved in iron clearance could be altered and accelerate disease progression. The previously described future directions followed up with chelation therapy in early disease stages could reveal if there are groups of subjects that benefit in particular from iron removal.

- **Is iron a good MRI based (theranostic) marker for AD?** With knowledge on the previous problem iron measures could be used as a theranostic marker during treatment. If iron-loading promotes AD-pathology, early intervention by iron chelators could be tracked via MRI based iron measures.

12 References

Acosta-Cabronero, Julio, Guy B. Williams, Arturo Cardenas-Blanco, Robert J. Arnold, Victoria Lupson, and Peter J. Nestor. 2013. 'In vivo quantitative susceptibility mapping (QSM) in Alzheimer's disease', *PLoS ONE*, 8: e81093-e93.

Agosta, F., M. Pievani, S. Sala, C. Geroldi, S. Galluzzi, G. B. Frisoni, and M. Filippi. 2011. 'White Matter Damage in Alzheimer Disease and Its Relationship to Gray Matter Atrophy', *Radiology*, 258: 853-63.

Agosta, Federica, Michela Pievani, Cristina Geroldi, Massimiliano Copetti, Giovanni B. Frisoni, and Massimo Filippi. 2012. 'Resting state fMRI in Alzheimer's disease: beyond the default mode network', *Neurobiology of Aging*, 33: 1564-78.

Albert, M. S., S. T. DeKosky, D. Dickson, B. Dubois, H. H. Feldman, N. C. Fox, A. Gamst, D. M. Holtzman, W. J. Jagust, R. C. Petersen, P. J. Snyder, M. C. Carrillo, B. Thies, and C. H. Phelps. 2011. 'The diagnosis of mild cognitive impairment due to Alzheimer's disease: recommendations from the National Institute on Aging-Alzheimer's Association workgroups on diagnostic guidelines for Alzheimer's disease', *Alzheimers Dement*, 7: 270-9.

Andersen, H. H., K. B. Johnsen, and T. Moos. 2014. 'Iron deposits in the chronically inflamed central nervous system and contributes to neurodegeneration', *Cell Mol Life Sci*, 71: 1607-22.

Association, Alzheimer's. 2017. '2017 Alzheimer's disease facts and figures', *Alzheimer's & Dementia*, 13: 325-73.

Ayton, S., N. G. Faux, A. I. Bush, and Initiative Alzheimer's Disease Neuroimaging. 2015. 'Ferritin levels in the cerebrospinal fluid predict Alzheimer's disease outcomes and are regulated by APOE', *Nat Commun*, 6: 6760.

Ayton, S., A. Fazlollahi, P. Bourgeat, P. Raniga, A. Ng, Y. Y. Lim, I. Diouf, S. Farquharson, J. Fripp, D. Ames, J. Doecke, P. Desmond, R. Ordidge, C. L. Masters, C. C. Rowe, P. Maruff, V. L. Villemagne, O. Salvado, A. I. Bush, and Australian Imaging Biomarkers Life. 2017. 'Cerebral quantitative susceptibility mapping predicts amyloid-beta-related cognitive decline', *Brain*, 140: 2112-19.

Ayton, Scott, Ibrahima Diouf, and Ashley Ian Bush. 2017. 'Evidence that iron accelerates Alzheimer's pathology: a CSF biomarker study', *Journal of Neurology, Neurosurgery & Psychiatry*.

Ball, M. J., M. Fisman, V. Hachinski, W. Blume, A. Fox, V. A. Kral, A. J. Kirshen, H. Fox, and H. Merskey. 1985. 'A new definition of Alzheimer's disease: a hippocampal dementia', *Lancet*, 1: 14-6.

Barbosa, Jeam Haroldo Oliveira, Antonio Carlos Santos, Vitor Tumas, Manju Liu, Weili Zheng, E. Mark Haacke, and Carlos Ernesto Garrido Salmon. 2015. 'Quantifying brain iron deposition in patients with Parkinson's disease using quantitative susceptibility mapping, R2 and R2', *Magnetic resonance imaging*, 33: 559-65.

Bartzokis, G., M. Beckson, D. B. Hance, P. Marx, J. A. Foster, and S. R. Marder. 1997. 'MR evaluation of age-related increase of brain iron in young adult and older normal males', *Magn Reson Imaging*, 15: 29-35.

Bartzokis, G., D. Sultzer, J. Cummings, L. E. Holt, D. B. Hance, V. W. Henderson, and J. Mintz. 2000. 'In vivo evaluation of brain iron in Alzheimer disease using magnetic resonance imaging', *Archives of general psychiatry*, 57: 47-53.

Bartzokis, G., and T. a Tishler. 2000. 'MRI evaluation of basal ganglia ferritin iron and neurotoxicity in Alzheimer's and Huntingon's disease', *Cellular and Molecular Biology*, 46: 821-33.

Barulli, D., and Y. Stern. 2013. 'Efficiency, capacity, compensation, maintenance, plasticity: emerging concepts in cognitive reserve', *Trends Cogn Sci*, 17: 502-9.

Benilova, I., E. Karran, and B. De Strooper. 2012. 'The toxic A beta oligomer and Alzheimer's disease: an emperor in need of clothes', *Nature Neuroscience*, 15: 349-57.

Benjamini, Yoav, and Yosef Hochberg. 1995. "Controlling the False Discovery Rate: A Practical and Powerful Approach to Multiple Testing." In, 289-300.

Bertram, Lars, Christoph Lange, Kristina Mullin, Michele Parkinson, Monica Hsiao, Meghan F. Hogan, Brit M. M. Schjeide, Basavaraj Hooli, Jason Divito, Iuliana Ionita, Hongyu Jiang, Nan Laird, Thomas Moscarillo, Kari L. Ohlsen, Kathryn Elliott, Xin Wang, Diane Hu-Lince, Marie Ryder, Amy Murphy, Steven L. Wagner, Deborah Blacker, K. David Becker, and Rudolph E. Tanzi. 2008. 'Genome-wide association analysis reveals putative Alzheimer's disease susceptibility loci in addition to APOE', *American journal of human genetics*, 83: 623-32.

Betts, M. J., J. Acosta-Cabronero, A. Cardenas-Blanco, P. J. Nestor, and E. Duzel. 2016. 'High-resolution characterisation of the aging brain using simultaneous quantitative susceptibility mapping (QSM) and R2* measurements at 7T', *NeuroImage*, 138: 43-63.

Binnewijzend, M. A., M. M. Schoonheim, E. Sanz-Arigita, A. M. Wink, W. M. van der Flier, N. Tolboom, S. M. Adriaanse, J. S. Damoiseaux, P. Scheltens, B. N. van Berckel, and F. Barkhof. 2012. 'Resting-state fMRI changes in Alzheimer's disease and mild cognitive impairment', *Neurobiol Aging*, 33: 2018-28.

Bishop, Nicholas a, Tao Lu, and Bruce a Yankner. 2010. 'Neural mechanisms of ageing and cognitive decline', *Nature*, 464: 529-35.

Biswal, B., F. Z. Yetkin, V. M. Haughton, and J. S. Hyde. 1995. 'Functional Connectivity in the Motor Cortex of Resting Human Brain Using Echo-Planar Mri', *Magnetic Resonance in Medicine*, 34: 537-41.

Braak, H., and E. Braak. 1991. 'Neuropathological stageing of Alzheimer-related changes', *Acta Neuropathol*, 82: 239-59.

Brettschneider, J., K. Del Tredici, V. M. Lee, and J. Q. Trojanowski. 2015. 'Spreading of pathology in neurodegenerative diseases: a focus on human studies', *Nat Rev Neurosci*, 16: 109-20.

Brier, M. R., J. B. Thomas, A. Z. Snyder, T. L. Benzinger, D. Y. Zhang, M. E. Raichle, D. M. Holtzman, J. C. Morris, and B. M. Ances. 2012. 'Loss of Intranetwork and Internetwork Resting State Functional Connections with Alzheimer's Disease Progression', *Journal of Neuroscience*, 32: 8890-99.

Buckner, R. L. 2005. 'Molecular, Structural, and Functional Characterization of Alzheimer's Disease: Evidence for a Relationship between Default Activity, Amyloid, and Memory', *Journal of Neuroscience*, 25: 7709-17.

Buckner, R. L., J. Sepulcre, T. Talukdar, F. M. Krienen, H. Liu, T. Hedden, J. R. Andrews-Hanna, R. A. Sperling, and K. A. Johnson. 2009. 'Cortical hubs revealed by intrinsic functional connectivity: mapping, assessment of stability, and relation to Alzheimer's disease', *J Neurosci*, 29: 1860-73.

Bush, Ashley I. 2013. 'The metal theory of Alzheimer's disease', *Journal of Alzheimer's disease : JAD*, 33 Suppl 1: S277-81.

Bush, Ashley I., Scott Ayton, Noel Garry Faux, He Xu, David Finkelstein, and Paul Adlard. 2014. 'Evidence for APOE protecting against brain iron overload', *Alzheimer's & Dementia: The Journal of the Alzheimer's Association*, 10: P878.

Caldeira, G. L., I. L. Ferreira, and A. C. Rego. 2013. 'Impaired transcription in Alzheimer's disease: key role in mitochondrial dysfunction and oxidative stress', *J Alzheimers Dis*, 34: 115-31.

Casanova, R., R. Srikanth, A. Baer, P. J. Laurienti, J. H. Burdette, S. Hayasaka, L. Flowers, F. Wood, and J. A. Maldjian. 2007. 'Biological parametric mapping: A statistical toolbox for multimodality brain image analysis', *NeuroImage*, 34: 137-43.

Cho, H., J. Y. Choi, M. S. Hwang, Y. J. Kim, H. M. Lee, H. S. Lee, J. H. Lee, Y. H. Ryu, M. S. Lee, and C. H. Lyoo. 2016. 'In Vivo Cortical Spreading Pattern of Tau and Amyloid in the Alzheimer Disease Spectrum', *Annals of Neurology*, 80: 247-58.

Coby, A. J., F. Picardal, E. Shelobolina, H. Xu, and E. E. Roden. 2011. 'Repeated anaerobic microbial redox cycling of iron', *Appl Environ Microbiol*, 77: 6036-42.

Cole, D. M., S. M. Smith, and C. F. Beckmann. 2010. 'Advances and pitfalls in the analysis and interpretation of resting-state FMRI data', *Front Syst Neurosci*, 4: 8.

Connor, J. R., S. L. Menzies, S. M. St Martin, and E. J. Mufson. 1992. 'A histochemical study of iron, transferrin, and ferritin in Alzheimer's diseased brains', *Journal of Neuroscience Research*, 31: 75-83.

Connor, J. R., B. S. Snyder, J. L. Beard, R. E. Fine, and E. J. Mufson. 1992. 'Regional distribution of iron and iron-regulatory proteins in the brain in aging and Alzheimer's disease', *Journal of Neuroscience Research*, 31: 327-35.

Conti, M. 2011. 'Focus on time-of-flight PET: the benefits of improved time resolution', *Eur J Nucl Med Mol Imaging*, 38: 1147-57.

Corder, E. H., a M. Saunders, W. J. Strittmatter, D. E. Schmechel, P. C. Gaskell, G. W. Small, a D. Roses, J. L. Haines, and M. a Pericak-Vance. 1993. 'Gene dose of apolipoprotein E type 4 allele and the risk of Alzheimer's disease in late onset families', *Science (New York, N.Y.)*, 261: 921-23.

Corrada, M. M., A. Paganini-Hill, D. J. Berlau, and C. H. Kawas. 2013. 'Apolipoprotein E genotype, dementia, and mortality in the oldest old: the 90+ Study', *Alzheimers Dement*, 9: 12-8.

Crapper McLachlan, D. R., A. J. Dalton, T. P. Kruck, M. Y. Bell, W. L. Smith, W. Kalow, and D. F. Andrews. 1991. 'Intramuscular desferrioxamine in patients with Alzheimer's disease', *Lancet (London, England)*, 337: 1304-8.

Damoiseaux, Jessica S., Katherine E. Prater, Bruce L. Miller, and Michael D. Greicius. 2012. 'Functional connectivity tracks clinical deterioration in Alzheimer's disease', *Neurobiology of Aging*, 33: 828.e19-30.

Daugherty, A. M., and N. Raz. 2016. 'Accumulation of iron in the putamen predicts its shrinkage in healthy older adults: A multi-occasion longitudinal study', *NeuroImage*, 128: 11-20.

de Leon, M. J., A. E. George, L. A. Stylopoulos, G. Smith, and D. C. Miller. 1989. 'Early marker for Alzheimer's disease: the atrophic hippocampus', *Lancet*, 2: 672-3.

de Rochefort, L., T. Liu, B. Kressler, J. Liu, P. Spincemaille, V. Lebon, J. Wu, and Y. Wang. 2010. 'Quantitative susceptibility map reconstruction from MR phase data using bayesian regularization: validation and application to brain imaging', *Magn Reson Med*, 63: 194-206.

Deibel, M. A., W. D. Ehmann, and W. R. Markesbery. 1996. 'Copper, iron, and zinc imbalances in severely degenerated brain regions in Alzheimer's disease: possible relation to oxidative stress', *J Neurol Sci*, 143: 137-42.

Deistung, A., A. Schafer, F. Schweser, U. Biedermann, R. Turner, and J. R. Reichenbach. 2013. 'Toward in vivo histology: a comparison of quantitative susceptibility mapping (QSM) with magnitude-, phase-, and R2*-imaging at ultra-high magnetic field strength', *NeuroImage*, 65: 299-314.

Deistung, Andreas, Ferdinand Schweser, Benedikt Wiestler, Mario Abello, Matthias Roethke, Felix Sahm, Wolfgang Wick, Armin Michael Nagel, Sabine Heiland, Heinz Peter Schlemmer, Martin Bendszus, Jürgen Rainer Reichenbach, and Alexander Radbruch. 2013. 'Quantitative Susceptibility Mapping Differentiates between Blood Depositions and Calcifications in Patients with Glioblastoma', *PLoS ONE*, 8: e57924-e24.

Dekhtyar, M., K. V. Papp, R. Buckley, H. I. L. Jacobs, A. P. Schultz, K. A. Johnson, R. A. Sperling, and D. M. Rentz. 2017. 'Neuroimaging markers associated with maintenance of optimal memory performance in late-life', *Neuropsychologia*, 100: 164-70.

Derry, Paul J., and Thomas A. Kent. 2017. 'Correlating quantitative susceptibility mapping with cognitive decline in Alzheimer’s disease', *Brain*, 140: 2069-72.

deToledo-Morrell, L., T. R. Stoub, M. Bulgakova, R. S. Wilson, D. A. Bennett, S. Leurgans, J. Wuu, and D. A. Turner. 2004. 'MRI-derived entorhinal volume is a good predictor of conversion from MCI to AD', *Neurobiol Aging*, 25: 1197-203.

Dickstein, D. L., J. Walsh, H. Brautigam, S. D. Stockton, S. Gandy, and P. R. Hof. 2010. 'Role of Vascular Risk Factors and Vascular Dysfunction in Alzheimer's Disease', *Mount Sinai Journal of Medicine*, 77: 82-102.

Dierksen, Gregory A., Maureen E. Skehan, Muhammad A. Khan, Jed Jeng, R. N. Kaveer Nandigam, John A. Becker, Ashok Kumar, Krista L. Neal, Rebecca A. Betensky, Matthew P. Frosch, Jonathan Rosand, Keith A. Johnson, Anand Viswanathan, David H. Salat, and Steven M. Greenberg. 2010.

'Spatial relation between microbleeds and amyloid deposits in amyloid angiopathy', *Annals of Neurology*, 68: 545-8.

Dixon, S. J., K. M. Lemberg, M. R. Lamprecht, R. Skouta, E. M. Zaitsev, C. E. Gleason, D. N. Patel, A. J. Bauer, A. M. Cantley, W. S. Yang, B. Morrison, 3rd, and B. R. Stockwell. 2012. 'Ferroptosis: an iron-dependent form of nonapoptotic cell death', *Cell*, 149: 1060-72.

Dixon, S. J., and B. R. Stockwell. 2014. 'The role of iron and reactive oxygen species in cell death', *Nature Chemical Biology*, 10: 9-17.

Djamanakova, A., X. Tang, X. Li, A. V. Faria, C. Ceritoglu, K. Oishi, A. E. Hillis, M. Albert, C. Lyketsos, M. I. Miller, and S. Mori. 2014. 'Tools for multiple granularity analysis of brain MRI data for individualized image analysis', *NeuroImage*, 101: 168-76.

Donahue, Manus J., Ediri Sideso, Bradley J. MacIntosh, James Kennedy, Ashok Handa, and Peter Jezzard. 2010. 'Absolute arterial cerebral blood volume quantification using inflow vascular-space-occupancy with dynamic subtraction magnetic resonance imaging', *Journal of cerebral blood flow and metabolism : official journal of the International Society of Cerebral Blood Flow and Metabolism*, 30: 1329-42.

Driscoll, I., D. A. Hamilton, H. Petropoulos, R. A. Yeo, W. M. Brooks, R. N. Baumgartner, and R. J. Sutherland. 2003. 'The aging hippocampus: cognitive, biochemical and structural findings', *Cereb Cortex*, 13: 1344-51.

Dubois, B., H. Hampel, H. H. Feldman, P. Scheltens, P. Aisen, S. Andrieu, H. Bakardjian, H. Benali, L. Bertram, K. Blennow, K. Broich, E. Cavedo, S. Crutch, J. F. Dartigues, C. Duyckaerts, S. Epelbaum, G. B. Frisoni, S. Gauthier, R. Genthon, A. A. Gouw, M. O. Habert, D. M. Holtzman, M. Kivipelto, S. Lista, J. L. Molinuevo, S. E. O'Bryant, G. D. Rabinovici, C. Rowe, S. Salloway, L. S. Schneider, R. Sperling, M. Teichmann, M. C. Carrillo, J. Cummings, C. R. Jack, Jr., Group Proceedings of the Meeting of the International Working, A. D. the American Alzheimer's Association on "The Preclinical State of, July, and U. S. A. Washington Dc. 2016. 'Preclinical Alzheimer's disease: Definition, natural history, and diagnostic criteria', *Alzheimers Dement*, 12: 292-323.

Duce, James a, Andrew Tsatsanis, Michael a Cater, Simon a James, Elysia Robb, Krutika Wikhe, Su Ling Leong, Keyla Perez, Timothy Johanssen, Mark a Greenough, Hyun Hee Cho, Denise Galatis, Robert D. Moir, Colin L. Masters, Catriona McLean, Rudolph E. Tanzi, Roberto Cappai, Kevin J. Barnham, Giuseppe D. Ciccotosto, Jack T. Rogers, and Ashley I. Bush. 2010. 'Iron-Export Ferroxidase Activity of β-Amyloid Precursor Protein is Inhibited by Zinc in Alzheimer's Disease', *Cell*, 142: 857-67.

Duvernoy, H., S. Delon, and J. L. Vannson. 1983. 'The vascularization of the human cerebellar cortex', *Brain Res Bull*, 11: 419-80.

Ellis, R. J., J. M. Olichney, L. J. Thal, S. S. Mirra, J. C. Morris, D. Beekly, and A. Heyman. 1996. 'Cerebral amyloid angiopathy in the brains of patients with Alzheimer's disease: the CERAD experience, Part XV', *Neurology*, 46: 1592-6.

Esiri, M., S. Chance, C. Joachim, D. Warden, A. Smallwood, C. Sloan, S. Christie, G. Wilcock, and A. D. Smith. 2015. 'Cerebral amyloid angiopathy, subcortical white matter disease and dementia: literature review and study in OPTIMA', *Brain Pathol*, 25: 51-62.

Everett, J., E. Céspedes, L. R. Shelford, C. Exley, J. F. Collingwood, J. Dobson, G. Van Der Laan, C. a Jenkins, E. Arenholz, and N. D. Telling. 2014. 'Ferrous iron formation following the co-aggregation of ferric iron and the Alzheimer's disease peptide β-amyloid (1–42)', *Journal of The Royal Society Interface*, 11: 20140165-65.

Fan, Z., D. J. Brooks, A. Okello, and P. Edison. 2017. 'An early and late peak in microglial activation in Alzheimer's disease trajectory', *Brain*, 140: 792-803.

Farrer, L. A., L. A. Cupples, J. L. Haines, B. Hyman, W. A. Kukull, R. Mayeux, R. H. Myers, M. A. Pericak-Vance, N. Risch, and C. M. van Duijn. 1997. 'Effects of age, sex, and ethnicity on the association between apolipoprotein E genotype and Alzheimer disease. A meta-analysis. APOE and Alzheimer Disease Meta Analysis Consortium', *JAMA*, 278: 1349-56.

Fisher, R. a. 1921. 'On the 'probable error' of coefficient of correlations deduced from a small sample', *Metron*, 1: 1-32.

Folstein, M. F., S. E. Folstein, and P. R. McHugh. 1975. '"Mini-mental state". A practical method for grading the cognitive state of patients for the clinician', *Journal of Psychiatric Research*, 12: 189-98.

Franzmeier, N., K. Buerger, S. Teipel, Y. Stern, M. Dichgans, M. Ewers, and Initiative Alzheimer's Disease Neuroimaging. 2017. 'Cognitive reserve moderates the association between functional network anti-correlations and memory in MCI', *Neurobiol Aging*, 50: 152-62.

Franzmeier, N., M. A. Caballero, A. N. Taylor, L. Simon-Vermot, K. Buerger, B. Ertl-Wagner, C. Mueller, C. Catak, D. Janowitz, E. Baykara, B. Gesierich, M. Duering, M. Ewers, and Initiative Alzheimer's Disease Neuroimaging. 2016. 'Resting-state global functional connectivity as a biomarker of cognitive reserve in mild cognitive impairment', *Brain Imaging Behav*.

Frisoni, G. B., N. C. Fox, C. R. Jack, Jr., P. Scheltens, and P. M. Thompson. 2010. 'The clinical use of structural MRI in Alzheimer disease', *Nat Rev Neurol*, 6: 67-77.

Friston, Karl J. 1994. 'Statistical parametric mapping.' in, *Functional neuroimaging: Technical foundations.* (Academic Press: San Diego, CA, US).

Garibotto, V., B. Borroni, S. Sorbi, S. F. Cappa, A. Padovani, and D. Perani. 2012. 'Education and occupation provide reserve in both ApoE epsilon4 carrier and noncarrier patients with probable Alzheimer's disease', *Neurol Sci*, 33: 1037-42.

Greicius, Michael D., Ben Krasnow, Allan L. Reiss, and Vinod Menon. 2003. 'Functional connectivity in the resting brain: a network analysis of the default mode hypothesis', *Proceedings of the National Academy of Sciences of the United States of America*, 100: 253-8.

Guo, C., P. Wang, M. L. Zhong, T. Wang, X. S. Huang, J. Y. Li, and Z. Y. Wang. 2013. 'Deferoxamine inhibits iron induced hippocampal tau phosphorylation in the Alzheimer transgenic mouse brain', *Neurochemistry International*, 62: 165-72.

Guo, C., T. Wang, W. Zheng, Z. Y. Shan, W. P. Teng, and Z. Y. Wang. 2013. 'Intranasal deferoxamine reverses iron-induced memory deficits and inhibits amyloidogenic APP processing in a transgenic mouse model of Alzheimer's disease', *Neurobiology of Aging*, 34: 562-75.

Guzman, V. A., O. T. Carmichael, C. Schwarz, G. Tosto, M. E. Zimmerman, A. M. Brickman, and Initiative Alzheimer's Disease Neuroimaging. 2013. 'White matter hyperintensities and amyloid are independently associated with entorhinal cortex volume among individuals with mild cognitive impairment', *Alzheimers Dement*, 9: S124-31.

Ha, C., J. Ryu, and C. B. Park. 2007. 'Metal ions differentially influence the aggregation and deposition of Alzheimer's beta-amyloid on a solid template', *Biochemistry*, 46: 6118-25.

Haacke, E. M., S. Mittal, Z. Wu, J. Neelavalli, and Y. C. N. Cheng. 2009. 'Susceptibility-Weighted Imaging: Technical Aspects and Clinical Applications, Part 1', *American Journal of Neuroradiology*, 30: 19-30.

Hallgren, B., and P. Sourander. 1958. 'The effect of age on the non-haemin iron in the human brain', *Journal of Neurochemistry*, 3: 41-51.

Hamalainen, A., M. Pihlajamaki, H. Tanila, T. Hanninen, E. Niskanen, S. Tervo, P. A. Karjalainen, R. L. Vanninen, and H. Soininen. 2007. 'Increased fMRI responses during encoding in mild cognitive impairment', *Neurobiology of Aging*, 28: 1889-903.

Hammers, A., R. Allom, M. J. Koepp, S. L. Free, R. Myers, L. Lemieux, T. N. Mitchell, D. J. Brooks, and J. S. Duncan. 2003. 'Three-dimensional maximum probability atlas of the human brain, with particular reference to the temporal lobe', *Hum Brain Mapp*, 19: 224-47.

Harman, D. 1956. 'Aging: a theory based on free radical and radiation chemistry', *J Gerontol*, 11: 298-300.

Harrison, P. M., and P. Arosio. 1996. 'The ferritins: molecular properties, iron storage function and cellular regulation', *Biochim Biophys Acta*, 1275: 161-203.

Helmstaedter, C., and H. F. Durwen. 1990. '[The Verbal Learning and Retention Test. A useful and differentiated tool in evaluating verbal memory performance]', *Schweiz Arch Neurol Psychiatr*, 141: 21-30.

Holland, C. M., E. E. Smith, I. Csapo, M. E. Gurol, D. A. Brylka, R. J. Killiany, D. Blacker, M. S. Albert, C. R. Guttmann, and S. M. Greenberg. 2008. 'Spatial distribution of white-matter hyperintensities in Alzheimer disease, cerebral amyloid angiopathy, and healthy aging', *Stroke*, 39: 1127-33.

Hollands, S., Y. Y. Lim, S. M. Laws, V. L. Villemagne, R. H. Pietrzak, K. Harrington, T. Porter, P. Snyder, D. Ames, C. Fowler, S. R. Rainey-Smith, R. N. Martins, O. Salvado, J. Robertson, C. C. Rowe, C. L. Masters, P. Maruff, and Aibl Research Group. 2017. 'APOEvarepsilon4 Genotype, Amyloid, and Clinical Disease Progression in Cognitively Normal Older Adults', *J Alzheimers Dis*.

House, Michael J., Timothy G. St. Pierre, Kris V. Kowdley, Thomas Montine, James Connor, John Beard, Jose Berger, Narendra Siddaiah, Eric Shankland, and Lee Way Jin. 2007. 'Correlation of proton transverse relaxation rates (R2) with iron concentrations in postmortem brain tissue from Alzheimer's disease patients', *Magnetic Resonance in Medicine*, 57: 172-80.

Howard, a R. 1950. 'Diagnostic value of the Wechsler Memory Scale with selected groups of institutionalized patients', *Journal of consulting psychology*, 14: 376-80.

Hua, Jun, Qin Qin, Manus J. Donahue, Jinyuan Zhou, James J. Pekar, and Peter C. M. Van Zijl. 2011. 'Inflow-based vascular-space-occupancy (iVASO) MRI', *Magnetic Resonance in Medicine*, 66: 40-56.

Hua, Jun, Qin Qin, Peter C. M. van Zijl, James J. Pekar, and Craig K. Jones. 2014. 'Whole-brain three-dimensional T2-weighted BOLD functional magnetic resonance imaging at 7 Tesla', *Magnetic Resonance in Medicine*, 72: 1530-40.

Huang, X. D., C. S. Atwood, M. A. Hartshorn, G. Multhaup, L. E. Goldstein, R. C. Scarpa, M. P. Cuajungco, D. N. Gray, J. Lim, R. D. Moir, R. E. Tanzi, and A. I. Bush. 1999. 'The A beta peptide of Alzheimer's disease directly produces hydrogen peroxide through metal ion reduction', *Biochemistry*, 38: 7609-16.

Huijbers, Willem, Elizabeth C. Mormino, Sarah E. Wigman, Andrew M. Ward, Patrizia Vannini, Donald G. McLaren, J. Alex Becker, Aaron P. Schultz, Trey Hedden, Keith a Johnson, and Reisa a Sperling. 2014. 'Amyloid deposition is linked to aberrant entorhinal activity among cognitively normal older adults', *Journal of Neuroscience*, 34: 5200-10.

Iannetti, G. D., and R. G. Wise. 2007. 'BOLD functional MRI in disease and pharmacological studies: room for improvement?', *Magnetic resonance imaging*, 25: 978-88.

Iorio, M., G. Spalletta, C. Chiapponi, G. Luccichenti, C. Cacciari, M. D. Orfei, C. Caltagirone, and F. Piras. 2013. 'White matter hyperintensities segmentation: a new semi-automated method', *Front Aging Neurosci*, 5: 76.

Jackson, J.D. 1975. *Magnetic field of a localized current distribution*.

Jagust, W. 2016. 'Is amyloid-beta harmful to the brain? Insights from human imaging studies', *Brain*, 139: 23-30.

Jagust, W. J., S. M. Landau, L. M. Shaw, J. Q. Trojanowski, R. A. Koeppe, E. M. Reiman, N. L. Foster, R. C. Petersen, M. W. Weiner, J. C. Price, C. A. Mathis, and Initiative Alzheimer's Disease Neuroimaging. 2009. 'Relationships between biomarkers in aging and dementia', *Neurology*, 73: 1193-9.

Jansen, W. J., R. Ossenkoppele, D. L. Knol, B. M. Tijms, P. Scheltens, F. R. Verhey, P. J. Visser, Group Amyloid Biomarker Study, P. Aalten, D. Aarsland, D. Alcolea, M. Alexander, I. S. Almdahl, S. E. Arnold, I. Baldeiras, H. Barthel, B. N. van Berckel, K. Bibeau, K. Blennow, D. J. Brooks, M. A. van Buchem, V. Camus, E. Cavedo, K. Chen, G. Chetelat, A. D. Cohen, A. Drzezga, S. Engelborghs, A. M. Fagan, T. Fladby, A. S. Fleisher, W. M. van der Flier, L. Ford, S. Forster, J. Fortea, N. Foskett, K. S. Frederiksen, Y. Freund-Levi, G. B. Frisoni, L. Froelich, T. Gabryelewicz, K. D. Gill, O. Gkatzima, E. Gomez-Tortosa, M. F. Gordon, T. Grimmer, H. Hampel, L. Hausner, S. Hellwig, S. K. Herukka, H. Hildebrandt, L. Ishihara, A. Ivanoiu, W. J. Jagust, P. Johannsen, R. Kandimalla, E. Kapaki, A. Klimkowicz-Mrowiec, W. E. Klunk, S. Kohler, N. Koglin, J. Kornhuber, M. G. Kramberger, K. Van Laere, S. M. Landau, D. Y. Lee, M. de Leon, V. Lisetti, A. Lleo, K. Madsen, W. Maier, J. Marcusson, N. Mattsson, A. de Mendonca, O. Meulenbroek, P. T. Meyer, M. A. Mintun, V. Mok, J. L. Molinuevo, H. M. Mollergard, J. C. Morris, B. Mroczko, S.

Van der Mussele, D. L. Na, A. Newberg, A. Nordberg, A. Nordlund, G. P. Novak, G. P. Paraskevas, L. Parnetti, G. Perera, O. Peters, J. Popp, S. Prabhakar, G. D. Rabinovici, I. H. Ramakers, L. Rami, C. Resende de Oliveira, J. O. Rinne, K. M. Rodrigue, E. Rodriguez-Rodriguez, C. M. Roe, U. Rot, C. C. Rowe, E. Ruther, O. Sabri, P. Sanchez-Juan, I. Santana, M. Sarazin, J. Schroder, C. Schutte, S. W. Seo, F. Soetewey, H. Soininen, L. Spiru, H. Struyfs, C. E. Teunissen, M. Tsolaki, R. Vandenberghe, M. M. Verbeek, V. L. Villemagne, S. J. Vos, L. J. van Waalwijk van Doorn, G. Waldemar, A. Wallin, A. K. Wallin, J. Wiltfang, D. A. Wolk, M. Zboch, and H. Zetterberg. 2015. 'Prevalence of cerebral amyloid pathology in persons without dementia: a meta-analysis', *JAMA*, 313: 1924-38.

Johnson, K. A., M. Gregas, J. A. Becker, C. Kinnecom, D. H. Salat, E. K. Moran, E. E. Smith, J. Rosand, D. M. Rentz, W. E. Klunk, C. A. Mathis, J. C. Price, S. T. Dekosky, A. J. Fischman, and S. M. Greenberg. 2007. 'Imaging of amyloid burden and distribution in cerebral amyloid angiopathy', *Ann Neurol*, 62: 229-34.

Johnson, Keith a, Reisa a Sperling, and Jorge Sepulcre. 2013. 'Functional connectivity in Alzheimer's disease: Measurement and meaning', *Biological Psychiatry*, 74: 318-19.

Karelson, E., N. Bogdanovic, A. Garlind, B. Winblad, K. Zilmer, T. Kullisaar, T. Vihalemm, C. Kairane, and M. Zilmer. 2001. 'The cerebrocortical areas in normal brain aging and in Alzheimer's disease: noticeable differences in the lipid peroxidation level and in antioxidant defense', *Neurochem Res*, 26: 353-61.

Kawas, C. H., D. E. Greenia, S. S. Bullain, C. M. Clark, M. J. Pontecorvo, A. D. Joshi, and M. M. Corrada. 2013. 'Amyloid imaging and cognitive decline in nondemented oldest-old: the 90+ Study', *Alzheimers Dement*, 9: 199-203.

Keep, R. F., Y. Hua, and G. H. Xi. 2012. 'Intracerebral haemorrhage: mechanisms of injury and therapeutic targets', *Lancet Neurology*, 11: 720-31.

Khan, A., J. P. Dobson, and C. Exley. 2006. 'Redox cycling of iron by Abeta42', *Free Radic Biol Med*, 40: 557-69.

Kim, Hyug-Gi, Soonchan Park, Hak Young Rhee, Kyung Mi Lee, Chang-Woo Ryu, Sun Jung Rhee, Soo Youl Lee, Yi Wang, and Geon-Ho Jahng. 2017. 'Quantitative susceptibility mapping to evaluate the early stage of Alzheimer's disease', *NeuroImage: Clinical*.

Kirsch, Wolff, Grant McAuley, Barbara Holshouser, Floyd Petersen, Muhammad Ayaz, Harry V. Vinters, Cindy Dickson, E. Mark Haacke, William Britt, James Larsen, Ivan Kim, Claudius Mueller, Matthew Schrag, and Daniel Kido. 2009. 'Serial susceptibility weighted MRI measures brain iron and microbleeds in dementia', *Journal of Alzheimer's Disease*, 17: 599-609.

Klunk, W. E., H. Engler, A. Nordberg, Y. Wang, G. Blomqvist, D. P. Holt, M. Bergstrom, I. Savitcheva, G. F. Huang, S. Estrada, B. Ausen, M. L. Debnath, J. Barletta, J. C. Price, J. Sandell, B. J. Lopresti, A. Wall, P. Koivisto, G. Antoni, C. A. Mathis, and B. Langstrom. 2004. 'Imaging brain amyloid in Alzheimer's disease with Pittsburgh Compound-B', *Ann Neurol*, 55: 306-19.

Koch, K., N. E. Myers, J. Gottler, L. Pasquini, T. Grimmer, S. Forster, A. Manoliu, J. Neitzel, A. Kurz, H. Forstl, V. Riedl, A. M. Wohlschlager, A. Drzezga, and C. Sorg. 2014. 'Disrupted Intrinsic Networks Link Amyloid-beta Pathology and Impaired Cognition in Prodromal Alzheimer's Disease', *Cereb Cortex*.

Koch, W., S. Teipel, S. Mueller, J. Benninghoff, M. Wagner, A. L. Bokde, H. Hampel, U. Coates, M. Reiser, and T. Meindl. 2012. 'Diagnostic power of default mode network resting state fMRI in the detection of Alzheimer's disease', *Neurobiol Aging*, 33: 466-78.

Koppenol, W. H. 2001. 'The Haber-Weiss cycle--70 years later', *Redox Rep*, 6: 229-34.

Kruer, M. C. 2013. 'The neuropathology of neurodegeneration with brain iron accumulation', *Int Rev Neurobiol*, 110: 165-94.

Langkammer, C., F. Schweser, N. Krebs, A. Deistung, W. Goessler, E. Scheurer, K. Sommer, G. Reishofer, K. Yen, F. Fazekas, S. Ropele, and J. R. Reichenbach. 2012. 'Quantitative susceptibility mapping (QSM) as a means to measure brain iron? A post mortem validation study', *NeuroImage*, 62: 1593-9.

Langkammer, Christian, Nikolaus Krebs, Walter Goessler, Eva Scheurer, Franz Ebner, Kathrin Yen, Franz Fazekas, and Stefan Ropele. 2010. 'Quantitative MR imaging of brain iron: a postmortem validation study', *Radiology*, 257: 455-62.

Lee, J., E. K. Culyba, E. T. Powers, and J. W. Kelly. 2011. 'Amyloid-beta forms fibrils by nucleated conformational conversion of oligomers', *Nature Chemical Biology*, 7: 602-09.

Li, J., S. Chang, T. Liu, Q. Wang, D. Cui, X. Chen, M. Jin, B. Wang, M. Pei, C. Wisnieff, P. Spincemaille, M. Zhang, and Y. Wang. 2012. 'Reducing the object orientation dependence of susceptibility effects in gradient echo MRI through quantitative susceptibility mapping', *Magn Reson Med*, 68: 1563-9.

Li, W., N. Wang, F. Yu, H. Han, W. Cao, R. Romero, B. Tantiwongkosi, T. Q. Duong, and C. Liu. 2015. 'A method for estimating and removing streaking artifacts in quantitative susceptibility mapping', *NeuroImage*, 108: 111-22.

Li, W., B. Wu, and C. Liu. 2011. 'Quantitative susceptibility mapping of human brain reflects spatial variation in tissue composition', *NeuroImage*, 55: 1645-56.

Lill, R., and U. Muhlenhoff. 2006. 'Iron-sulfur protein biogenesis in eukaryotes: components and mechanisms', *Annu Rev Cell Dev Biol*, 22: 457-86.

Lim, I. A., A. V. Faria, X. Li, J. T. Hsu, R. D. Airan, S. Mori, and P. C. van Zijl. 2013. 'Human brain atlas for automated region of interest selection in quantitative susceptibility mapping: application to determine iron content in deep gray matter structures', *NeuroImage*, 82: 449-69.

Liu, Beinan, Aileen Moloney, Sarah Meehan, Kyle Morris, Sally E. Thomas, Louise C. Serpell, Robert Hider, Stefan J. Marciniak, David a Lomas, and Damian C. Crowther. 2011. 'Iron promotes the toxicity of amyloid beta peptide by impeding its ordered aggregation', *Journal of Biological Chemistry*, 286: 4248-56.

Liu, Chunlei, Wei Li, G. Allan Johnson, and Bing Wu. 2011. 'High-field (9.4T) MRI of brain dysmyelination by quantitative mapping of magnetic susceptibility', *NeuroImage*, 56: 930-38.

Liu, Enchi, Mark E. Schmidt, Richard Margolin, Reisa Sperling, Robert Koeppe, Neale S. Mason, William E. Klunk, Chester A. Mathis, Stephen Salloway, Nick C. Fox, Derek L. Hill, Andrea S. Les, Peter Collins, Keith M. Gregg, Jianing Di, Yuan Lu, I. Cristina Tudor, Bradley T. Wyman, Kevin Booth, Stephanie Broome, Eric Yuen, Michael Grundman, and H. Robert Brashear. 2015. 'Amyloid-β 11C-PiB-PET imaging results from 2 randomized bapineuzumab phase 3 AD trials', *Neurology*, 85: WNL.0000000000001877--WNL.77-.

Liu, Tian, Pascal Spincemaille, Ludovic De Rochefort, Bryan Kressler, and Yi Wang. 2009. 'Calculation of susceptibility through multiple orientation sampling (COSMOS): A method for conditioning the inverse problem from measured magnetic field map to susceptibility source image in MRI', *Magnetic Resonance in Medicine*, 61: 196-204.

Logothetis, N. K. 2008. 'What we can do and what we cannot do with fMRI', *Nature*, 453: 869-78.

Logothetis, N. K., J. Pauls, M. Augath, T. Trinath, and A. Oeltermann. 2001. 'Neurophysiological investigation of the basis of the fMRI signal', *Nature*, 412: 150-7.

Malecki, E. A., and J. R. Connor. 2002. 'The case for iron chelation and/or antioxidant therapy in Alzheimer's disease', *Drug Development Research*, 56: 526-30.

Mandelkow, E. M., and E. Mandelkow. 2012. 'Biochemistry and Cell Biology of Tau Protein in Neurofibrillary Degeneration', *Cold Spring Harbor perspectives in medicine*, 2.

Marques, P., P. Moreira, R. Magalhaes, P. Costa, N. Santos, J. Zihl, J. Soares, and N. Sousa. 2016. 'The functional connectome of cognitive reserve', *Hum Brain Mapp*, 37: 3310-22.

Masters, C. L., and D. J. Selkoe. 2012. 'Biochemistry of Amyloid beta-Protein and Amyloid Deposits in Alzheimer Disease', *Cold Spring Harbor perspectives in medicine*, 2.

Mathis, C. A., N. S. Mason, B. J. Lopresti, and W. E. Klunk. 2012. 'Development of positron emission tomography beta-amyloid plaque imaging agents', *Semin Nucl Med*, 42: 423-32.

McKhann, Guy M., David S. Knopman, Howard Chertkow, Bradley T. Hyman, Clifford R. Jack, Claudia H. Kawas, William E. Klunk, Walter J. Koroshetz, Jennifer J. Manly, Richard Mayeux, Richard C. Mohs, John C. Morris, Martin N. Rossor, Philip Scheltens, Maria C. Carrillo, Bill Thies, Sandra Weintraub, and Creighton H. Phelps. 2011. 'The diagnosis of dementia due to Alzheimer's disease:

Recommendations from the National Institute on Aging-Alzheimer's Association workgroups on diagnostic guidelines for Alzheimer's disease', *Alzheimer's and Dementia*, 7: 263-69.

Meadowcroft, M. D., J. R. Connor, M. B. Smith, and Q. X. Yang. 2009. 'MRI and histological analysis of beta-amyloid plaques in both human Alzheimer's disease and APP/PS1 transgenic mice', *J Magn Reson Imaging*, 29: 997-1007.

Mechelli, A., C. J. Price, K. J. Friston, and J. Ashburner. 2005. 'Voxel-based morphometry of the human brain: Methods and applications', *Current Medical Imaging Reviews*, 1: 105-13.

Meiser, J., D. Weindl, and K. Hiller. 2013. 'Complexity of dopamine metabolism', *Cell Commun Signal*, 11: 34.

Mintun, M. A., G. N. Larossa, Y. I. Sheline, C. S. Dence, S. Y. Lee, R. H. Mach, W. E. Klunk, C. A. Mathis, S. T. DeKosky, and J. C. Morris. 2006. '[11C]PIB in a nondemented population: potential antecedent marker of Alzheimer disease', *Neurology*, 67: 446-52.

Mittal, S., Z. Wu, J. Neelavalli, and E. M. Haacke. 2009. 'Susceptibility-Weighted Imaging: Technical Aspects and Clinical Applications, Part 2', *American Journal of Neuroradiology*, 30: 232-52.

Mladenka, P., T. Simunek, M. Hubl, and R. Hrdina. 2006. 'The role of reactive oxygen and nitrogen species in cellular iron metabolism', *Free Radic Res*, 40: 263-72.

Moos, T., T. R. Nielsen, T. Skjorringe, and E. H. Morgan. 2007. 'Iron trafficking inside the brain', *Journal of Neurochemistry*, 103: 1730-40.

Mori, S., D. Wu, C. Ceritoglu, Y. Li, A. Kolasny, M. A. Vaillant, A. V. Faria, K. Oishi, and M. I. Miller. 2016. 'MRICloud: Delivering High-Throughput MRI Neuroinformatics as Cloud-Based Software as a Service', *Computing in Science & Engineering*, 18: 21-35.

Mormino, E. C., R. A. Betensky, T. Hedden, A. P. Schultz, R. E. Amariglio, D. M. Rentz, K. A. Johnson, and R. A. Sperling. 2014. 'Synergistic effect of beta-amyloid and neurodegeneration on cognitive decline in clinically normal individuals', *JAMA Neurol*, 71: 1379-85.

Mormino, Elizabeth C., Rebecca a Betensky, Trey Hedden, Aaron P. Schultz, Andrew Ward, Willem Huijbers, Dorene M. Rentz, Keith a Johnson, and Reisa a Sperling. 2014. 'Amyloid and APOE ε4 interact to influence short-term decline in preclinical Alzheimer disease', *Neurology*, 82: 1760-67.

Morris, John C., Catherine M. Roe, Chengjie Xiong, Anne M. Fagan, Alison M. Goate, David M. Holtzman, and Mark A. Mintun. 2010. 'APOE predicts amyloid-beta but not tau Alzheimer pathology in cognitively normal aging', *Annals of Neurology*, 67: 122-31.

Morris, M., S. Maeda, K. Vossel, and L. Mucke. 2011. 'The Many Faces of Tau', *Neuron*, 70: 410-26.

Mortamais, M., J. A. Ash, J. Harrison, J. Kaye, J. Kramer, C. Randolph, C. Pose, B. Albala, M. Ropacki, C. W. Ritchie, and K. Ritchie. 2017. 'Detecting cognitive changes in preclinical Alzheimer's disease: A review of its feasibility', *Alzheimers Dement*, 13: 468-92.

Mosher, Kira Irving, and Tony Wyss-Coray. 2014. 'Microglial dysfunction in brain aging and Alzheimer's disease', *Biochemical pharmacology*, 88: 594-604.

Mucke, L., and D. J. Selkoe. 2012. 'Neurotoxicity of amyloid beta-protein: synaptic and network dysfunction', *Cold Spring Harb Perspect Med*, 2: a006338.

Murakami, Y., S. Kakeda, K. Watanabe, I. Ueda, A. Ogasawara, J. Moriya, S. Ide, K. Futatsuya, T. Sato, K. Okada, T. Uozumi, S. Tsuji, T. Liu, Y. Wang, and Y. Korogi. 2015. 'Usefulness of Quantitative Susceptibility Mapping for the Diagnosis of Parkinson Disease', *American Journal of Neuroradiology*, 36: 1102-08.

Nasreddine, Ziad S., Natalie a Phillips, Valérie Bédirian, Simon Charbonneau, Victor Whitehead, Isabelle Collin, Jeffrey L. Cummings, and Howard Chertkow. 2005. 'The Montreal Cognitive Assessment, MoCA: A brief screening tool for mild cognitive impairment', *Journal of the American Geriatrics Society*, 53: 695-99.

Nicholas, Linda E., Robert H. Brookshire, Donald L. Maclennan, James G. Schumacher, and Shirley a Porrazzo. 1989. "Revised administration and scoring procedures for the Boston Naming test and norms for non-brain-damaged adults." In, 569-80.

Nitsch, Roger M., and Christoph Hock. 2008. 'Targeting β-amyloid pathology in Alzheimer’s disease with Aβ immunotherapy', *Neurotherapeutics*, 5: 415-20.

Nunez, M. T., P. Urrutia, N. Mena, P. Aguirre, V. Tapia, and J. Salazar. 2012. 'Iron toxicity in neurodegeneration', *Biometals*, 25: 761-76.

Nunomura, A., G. Perry, G. Aliev, K. Hirai, A. Takeda, E. K. Balraj, P. K. Jones, H. Ghanbari, T. Wataya, S. Shimohama, S. Chiba, C. S. Atwood, R. B. Petersen, and M. A. Smith. 2001. 'Oxidative damage is the earliest event in Alzheimer disease', *Journal of neuropathology and experimental neurology*, 60: 759-67.

Nyberg, L., M. Lovden, K. Riklund, U. Lindenberger, and L. Backman. 2012. 'Memory aging and brain maintenance', *Trends Cogn Sci*, 16: 292-305.

Ortiz, E., J. M. Pasquini, K. Thompson, B. Felt, G. Butkus, J. Beard, and J. R. Connor. 2004. 'Effect of manipulation of iron storage, transport, or availability on myelin composition and brain iron content in three different animal models', *J Neurosci Res*, 77: 681-9.

Paolini, M., D. Keeser, M. Ingrisch, N. Werner, N. Kindermann, M. Reiser, and J. Blautzik. 2015. 'Resting-state networks in healthy adult subjects: a comparison between a 32-element and an 8-element phased array head coil at 3.0 Tesla', *Acta Radiol*, 56: 605-13.

Pasek, M. A., and D. S. Lauretta. 2005. 'Aqueous corrosion of phosphide minerals from iron meteorites: a highly reactive source of prebiotic phosphorus on the surface of the early Earth', *Astrobiology*, 5: 515-35.

Patel, Krishna Rutvij. 2015. 'Biogen's aducanumab raises hope that Alzheimer's can be treated at its source', *Managed care (Langhorne, Pa.)*, 24: 19-19.

Peters, D. G., J. R. Connor, and M. D. Meadowcroft. 2015. 'The relationship between iron dyshomeostasis and amyloidogenesis in Alzheimer's disease: Two sides of the same coin', *Neurobiology of Disease*, 81: 49-65.

Petersen, R. C., G. E. Smith, S. C. Waring, R. J. Ivnik, E. G. Tangalos, and E. Kokmen. 1999. 'Mild cognitive impairment: clinical characterization and outcome', *Archives of Neurology*, 56: 303-08.

Pietrzak, R. H., Y. Y. Lim, D. Ames, K. Harrington, C. Restrepo, R. N. Martins, A. Rembach, S. M. Laws, C. L. Masters, V. L. Villemagne, C. C. Rowe, P. Maruff, Biomarkers Australian Imaging, and Group Lifestyle Research. 2015. 'Trajectories of memory decline in preclinical Alzheimer's disease: results from the Australian Imaging, Biomarkers and Lifestyle Flagship Study of ageing', *Neurobiol Aging*, 36: 1231-8.

Pipitone, J., M. T. M. Park, J. Winterburn, T. A. Lett, J. P. Lerch, J. C. Pruessner, M. Lepage, A. N. Voineskos, M. M. Chakravarty, and Alzheimer's Dis Neuroimaging Initi. 2014. 'Multi-atlas segmentation of the whole hippocampus and subfields using multiple automatically generated templates', *NeuroImage*, 101: 494-512.

Provenzano, F. A., J. Muraskin, G. Tosto, A. Narkhede, B. T. Wasserman, E. Y. Griffith, V. A. Guzman, I. B. Meier, M. E. Zimmerman, A. M. Brickman, and Initiative Alzheimer's Disease Neuroimaging. 2013. 'White matter hyperintensities and cerebral amyloidosis: necessary and sufficient for clinical expression of Alzheimer disease?', *JAMA Neurol*, 70: 455-61.

Quevenco, F. C., M. G. Preti, J. M. van Bergen, J. Hua, M. Wyss, X. Li, S.J. Schreiner, S. C. Steininger, R. Meyer, I.B. Meier, A. M. Brickman, S.E. Leh, A.F. Gietl, A. Buck, R. M. Nitsch, K. P. Pruessmann, P. C. van Zijl, C. Hock, D. Van de Ville, and P. G. Unschuld. 2017. 'Memory performance related dynamic brain connectivity indicates pathological burden and genetic risk for Alzheimer's disease', *Alzheimer's Research and Therapy*, in press.

Rane, Swati, Pratik Talati, Manus J. Donahue, and Stephan Heckers. 2015. 'Inflow-vascular space occupancy (iVASO) reproducibility in the hippocampus and cortex at different blood water nulling times', *Magnetic Resonance in Medicine*, c: n/a-n/a.

Reiman, Eric M., Kewei Chen, Xiaofen Liu, Daniel Bandy, Meixiang Yu, Wendy Lee, Napatkamon Ayutyanont, Jennifer Keppler, Stephanie a Reeder, Jessica B. S. Langbaum, Gene E. Alexander, William E. Klunk, Chester a Mathis, Julie C. Price, Howard J. Aizenstein, Steven T. DeKosky, and Richard J. Caselli. 2009. 'Fibrillar amyloid-beta burden in cognitively normal people at 3 levels of genetic risk for Alzheimer's disease', *Proceedings of the National Academy of Sciences of the United States of America*, 106: 6820-25.

Roberts, B. R., M. Lind, A. Z. Wagen, A. Rembach, T. Frugier, Q. X. Li, T. M. Ryan, C. A. McLean, J. D. Doecke, C. C. Rowe, V. L. Villemagne, and C. L. Masters. 2017. 'Biochemically-defined pools of amyloid-beta in sporadic Alzheimer's disease: correlation with amyloid PET', *Brain*.

Rogalski, E. J., T. Gefen, J. Shi, M. Samimi, E. Bigio, S. Weintraub, C. Geula, and M. M. Mesulam. 2013. 'Youthful memory capacity in old brains: anatomic and genetic clues from the Northwestern SuperAging Project', *J Cogn Neurosci*, 25: 29-36.

Rombouts, Serge a R. B., Frederik Barkhof, Rutger Goekoop, Cornelis J. Stam, and Philip Scheltens. 2005. 'Altered resting state networks in mild cognitive impairment and mild Alzheimer's disease: An fMRI study', *Human Brain Mapping*, 26: 231-39.

Rottkamp, C. A., A. K. Raina, X. Zhu, E. Gaier, A. I. Bush, C. S. Atwood, M. Chevion, G. Perry, and M. A. Smith. 2001. 'Redox-active iron mediates amyloid-beta toxicity', *Free Radic Biol Med*, 30: 447-50.

Schenck, J. F. 1996. 'The role of magnetic susceptibility in magnetic resonance imaging: MRI magnetic compatibility of the first and second kinds', *Medical Physics*, 23: 815-50.

Schmechel, D. E., A. M. Saunders, W. J. Strittmatter, B. J. Crain, C. M. Hulette, S. H. Joo, M. A. Pericak-Vance, D. Goldgaber, and A. D. Roses. 1993. 'Increased amyloid beta-peptide deposition in cerebral cortex as a consequence of apolipoprotein E genotype in late-onset Alzheimer disease', *Proceedings of the National Academy of Sciences of the United States of America*, 90: 9649-53.

Schmidt, P., C. Gaser, M. Arsic, D. Buck, A. Forschler, A. Berthele, M. Hoshi, R. Ilg, V. J. Schmid, C. Zimmer, B. Hemmer, and M. Muhlau. 2012. 'An automated tool for detection of FLAIR-hyperintense white-matter lesions in Multiple Sclerosis', *NeuroImage*, 59: 3774-83.

Schreiner, Simon J., Xinyang Liu, Anton F. Gietl, Michael Wyss, Stefanie C. Steininger, Esmeralda Gruber, Valerie Treyer, Irene B. Meier, Andrea M. Kälin, Sandra E. Leh, Alfred Buck, Roger M. Nitsch, Klaas P. Pruessmann, Christoph Hock, and Paul G. Unschuld. 2014. 'Regional Fluid-Attenuated Inversion Recovery (FLAIR) at 7 Tesla correlates with amyloid beta in hippocampus and brainstem of cognitively normal elderly subjects', *Frontiers in Aging Neuroscience*, 6: 240-40.

Schweser, F., A. Deistung, B. W. Lehr, and J. R. Reichenbach. 2011. 'Quantitative imaging of intrinsic magnetic tissue properties using MRI signal phase: an approach to in vivo brain iron metabolism?', *NeuroImage*, 54: 2789-807.

Schweser, F., K. Sommer, A. Deistung, and J. R. Reichenbach. 2012. 'Quantitative susceptibility mapping for investigating subtle susceptibility variations in the human brain', *NeuroImage*, 62: 2083-100.

Seeley, W. W., J. M. Allman, D. A. Carlin, R. K. Crawford, M. N. Macedo, M. D. Greicius, S. J. Dearmond, and B. L. Miller. 2007. 'Divergent social functioning in behavioral variant frontotemporal dementia and Alzheimer disease: reciprocal networks and neuronal evolution', *Alzheimer Dis Assoc Disord*, 21: S50-7.

Seeley, W. W., R. K. Crawford, J. Zhou, B. L. Miller, and M. D. Greicius. 2009. 'Neurodegenerative diseases target large-scale human brain networks', *Neuron*, 62: 42-52.

Selkoe, D. J., and J. Hardy. 2016. 'The amyloid hypothesis of Alzheimer's disease at 25 years', *EMBO Mol Med*, 8: 595-608.

Serrano-Pozo, A., R. A. Betensky, M. P. Frosch, and B. T. Hyman. 2016. 'Plaque-Associated Local Toxicity Increases over the Clinical Course of Alzheimer Disease', *Am J Pathol*, 186: 375-84.

Serrano-Pozo, A., M. P. Frosch, E. Masliah, and B. T. Hyman. 2011. 'Neuropathological alterations in Alzheimer disease', *Cold Spring Harb Perspect Med*, 1: a006189.

Sevigny, J., P. Chiao, T. Bussiere, P. H. Weinreb, L. Williams, M. Maier, R. Dunstan, S. Salloway, T. Chen, Y. Ling, J. O'Gorman, F. Qian, M. Arastu, M. Li, S. Chollate, M. S. Brennan, O. Quintero-Monzon, R. H. Scannevin, H. M. Arnold, T. Engber, K. Rhodes, J. Ferrero, Y. Hang, A. Mikulskis, J. Grimm, C. Hock, R. M. Nitsch, and A. Sandrock. 2016. 'The antibody aducanumab reduces Abeta plaques in Alzheimer's disease', *Nature*, 537: 50-6.

Sheline, Y. I., and M. E. Raichle. 2013. 'Resting state functional connectivity in preclinical Alzheimer's disease', *Biol Psychiatry*, 74: 340-7.

Sheline, Y. I., M. E. Raichle, A. Z. Snyder, J. C. Morris, D. Head, S. Wang, and M. A. Mintun. 2010. 'Amyloid plaques disrupt resting state default mode network connectivity in cognitively normal elderly', *Biol Psychiatry*, 67: 584-7.

Smith, S. M., D. Vidaurre, C. F. Beckmann, M. F. Glasser, M. Jenkinson, K. L. Miller, T. E. Nichols, E. C. Robinson, G. Salimi-Khorshidi, M. W. Woolrich, D. M. Barch, K. Ugurbil, and D. C. Van Essen. 2013. 'Functional connectomics from resting-state fMRI', *Trends in Cognitive Sciences*, 17: 666-82.

Solbach, C., M. Uebele, G. Reischl, and H. J. Machulla. 2005. 'Efficient radiosynthesis of carbon-11 labelled uncharged Thioflavin T derivatives using [11C]methyl triflate for beta-amyloid imaging in Alzheimer's Disease with PET', *Appl Radiat Isot*, 62: 591-5.

Sotaniemi, M., V. Pulliainen, L. Hokkanen, T. Pirttila, I. Hallikainen, H. Soininen, and T. Hanninen. 2012. 'CERAD-neuropsychological battery in screening mild Alzheimer's disease', *Acta Neurol Scand*, 125: 16-23.

Sperling, R. A., P. S. Aisen, L. A. Beckett, D. A. Bennett, S. Craft, A. M. Fagan, T. Iwatsubo, C. R. Jack, Jr., J. Kaye, T. J. Montine, D. C. Park, E. M. Reiman, C. C. Rowe, E. Siemers, Y. Stern, K. Yaffe, M. C. Carrillo, B. Thies, M. Morrison-Bogorad, M. V. Wagster, and C. H. Phelps. 2011. 'Toward defining the preclinical stages of Alzheimer's disease: recommendations from the National Institute on Aging-Alzheimer's Association workgroups on diagnostic guidelines for Alzheimer's disease', *Alzheimers Dement*, 7: 280-92.

Sperling, R. A., R. E. Amariglio, G. A. Marshall, and D. M. Rentz. 2015. 'Establishing Clinical Relevance in Preclinical Alzheimer's Disease', *The journal of prevention of Alzheimer's disease*, 2: 85-87.

Sperling, R. A., P. S. Laviolette, K. O'Keefe, J. O'Brien, D. M. Rentz, M. Pihlajamaki, G. Marshall, B. T. Hyman, D. J. Selkoe, T. Hedden, R. L. Buckner, J. A. Becker, and K. A. Johnson. 2009. 'Amyloid deposition is associated with impaired default network function in older persons without dementia', *Neuron*, 63: 178-88.

Sperling, Reisa A., Bradford C. Dickerson, Maija Pihlajamaki, Patrizia Vannini, Peter S. LaViolette, Ottavio V. Vitolo, Trey Hedden, J. Alex Becker, Dorene M. Rentz, Dennis J. Selkoe, and Keith A. Johnson. 2010. 'Functional alterations in memory networks in early Alzheimer's disease', *Neuromolecular medicine*, 12: 27-43.

Sperling, Reisa, Stephen Salloway, David J. Brooks, Donatella Tampieri, Jerome Barakos, Nick C. Fox, Murray Raskind, Marwan Sabbagh, Lawrence S. Honig, Anton P. Porsteinsson, Ivan Lieberburg, H. Michael Arrighi, Kristen a Morris, Yuan Lu, Enchi Liu, Keith M. Gregg, H. Robert Brashear, Gene G. Kinney, Ronald Black, and Michael Grundman. 2012. 'Amyloid-related imaging abnormalities in patients with Alzheimer's disease treated with bapineuzumab: A retrospective analysis', *The Lancet Neurology*, 11: 241-49.

Squitti, Rosanna. 2012. 'Metals in alzheimer's disease: a systemic perspective', *Frontiers in Bioscience*, 17: 451-51.

Steffener, J., and Y. Stern. 2012. 'Exploring the neural basis of cognitive reserve in aging', *Biochim Biophys Acta*, 1822: 467-73.

Steininger, Stefanie C., Xinyang Liu, Anton Gietl, Michael Wyss, Simon Schreiner, Esmeralda Gruber, Valerie Treyer, Andrea Kälin, Sandra Leh, Alfred Buck, Roger M. Nitsch, Klaas P. Prüssmann, Christoph Hock, and Paul G. Unschuld. 2014. 'Cortical amyloid beta in cognitively normal elderly adults is associated with decreased network efficiency within the cerebro-cerebellar system', *Frontiers in Aging Neuroscience*, 6: 52-52.

Sun, Y., A. N. Pham, and T. D. Waite. 2016. 'Elucidation of the interplay between Fe(II), Fe(III), and dopamine with relevance to iron solubilization and reactive oxygen species generation by catecholamines', *J Neurochem*, 137: 955-68.

Tang, M. Y., T. W. Chen, X. M. Zhang, and X. H. Huang. 2014. 'GRE T2*-Weighted MRI: Principles and Clinical Applications', *Biomed Research International*.

Tang, X., K. Oishi, A. V. Faria, A. E. Hillis, M. S. Albert, S. Mori, and M. I. Miller. 2013. 'Bayesian Parameter Estimation and Segmentation in the Multi-Atlas Random Orbit Model', *PLoS ONE*, 8: e65591.

Tanzi, R. E. 2012. 'The genetics of Alzheimer disease', *Cold Spring Harb Perspect Med*, 2.

Thal, D. R., J. Attems, and M. Ewers. 2014. 'Spreading of Amyloid, Tau, and Microvascular Pathology in Alzheimer's Disease: Findings from Neuropathological and Neuroimaging Studies', *Journal of Alzheimers Disease*, 42: S421-S29.

Tombaugh, T. N. 2004. 'Trail Making Test A and B: normative data stratified by age and education', *Arch Clin Neuropsychol*, 19: 203-14.

Van Bergen, J., X. Li, A Gietl, V. Treyer, R. Meyer, A Buck, P. A. Kaufmann, R. Nitsch, P. C. Van Zijl, C. Hock, and P. Unschuld. 2017. 'Low cortical iron and high entorhinal cortex volume promote cognitive functioning in the oldest-old', *Neurobiol Aging*.

van Bergen, J. M., J. Hua, P. G. Unschuld, I. A. Lim, C. K. Jones, R. L. Margolis, C. A. Ross, P. C. van Zijl, and X. Li. 2016. 'Quantitative Susceptibility Mapping Suggests Altered Brain Iron in Premanifest Huntington Disease', *AJNR Am J Neuroradiol*, 37: 789-96.

van Bergen, J. M., X. Li, J. Hua, S. J. Schreiner, S. C. Steininger, F. C. Quevenco, M. Wyss, A. F. Gietl, V. Treyer, S. E. Leh, F. Buck, R. M. Nitsch, K. P. Pruessmann, P. C. van Zijl, C. Hock, and P. G. Unschuld. 2016. 'Colocalization of cerebral iron with Amyloid beta in Mild Cognitive Impairment', *Sci Rep*, 6: 35514.

van der Kant, R., and L. S. B. Goldstein. 2015. 'Cellular Functions of the Amyloid Precursor Protein from Development to Dementia', *Developmental Cell*, 32: 502-15.

van Rooden, Sanneke, Nhat Trung Doan, Maarten J. Versluis, Jeroen D. C. Goos, Andrew G. Webb, Ania M. Oleksik, Wiesje M. van der Flier, Philip Scheltens, Frederik Barkhof, Annelies W. E. Weverling-Rynsburger, Gerard Jan Blauw, Johan H. C. Reiber, Mark a van Buchem, Julien Milles, and Jeroen van der Grond. 2014. '7T T2(∗)-weighted magnetic resonance imaging reveals cortical phase differences between early- and late-onset Alzheimer's disease', *Neurobiology of Aging*, 36: 1-7.

Vandenberghe, R., K. Van Laere, A. Ivanoiu, E. Salmon, C. Bastin, E. Triau, S. Hasselbalch, I. Law, A. Andersen, A. Korner, L. Minthon, G. Garraux, N. Nelissen, G. Bormans, C. Buckley, R. Owenius, L. Thurfjell, G. Farrar, and D. J. Brooks. 2010. '18F-flutemetamol amyloid imaging in Alzheimer disease and mild cognitive impairment: a phase 2 trial', *Ann Neurol*, 68: 319-29.

Verghese, Philip B., Joseph M. Castellano, Kanchan Garai, Yinong Wang, Hong Jiang, Aarti Shah, Guojun Bu, Carl Frieden, and David M. Holtzman. 2013. 'ApoE influences amyloid-β (Aβ) clearance despite minimal apoE/Aβ association in physiological conditions', *Proceedings of the National Academy of Sciences of the United States of America*, 110: E1807-16.

Wang, Y., and T. Liu. 2015. 'Quantitative susceptibility mapping (QSM): Decoding MRI data for a tissue magnetic biomarker', *Magn Reson Med*, 73: 82-101.

Ward, Andrew M., Elizabeth C. Mormino, Willem Huijbers, Aaron P. Schultz, Trey Hedden, and Reisa a Sperling. 2014. 'Relationships between default-mode network connectivity, medial temporal lobe structure, and age-related memory deficits', *Neurobiology of Aging*, 36: 265-72.

Weller, R. O., a Massey, T. a Newman, M. Hutchings, Y. M. Kuo, and a E. Roher. 1998. 'Cerebral amyloid angiopathy: amyloid beta accumulates in putative interstitial fluid drainage pathways in Alzheimer's disease', *The American journal of pathology*, 153: 725-33.

Whitfield-Gabrieli, S., and A. Nieto-Castanon. 2012. 'Conn: a functional connectivity toolbox for correlated and anticorrelated brain networks', *Brain Connect*, 2: 125-41.

Winblad, Bengt, Ana Graf, Marie-Emmanuelle Riviere, Niels Andreasen, and J. Michael Ryan. 2014. 'Active immunotherapy options for Alzheimer's disease', *Alzheimer's research & therapy*, 6: 7-7.

Winterbourn, C. C. 1995. 'Toxicity of iron and hydrogen peroxide: the Fenton reaction', *Toxicol Lett*, 82-83: 969-74.

Wood, Heather. 2015. 'Alzheimer disease: Iron--the missing link between ApoE and Alzheimer disease?', *Nature reviews. Neurology*, 11: 369-69.

Wu, B., W. Li, A. V. Avram, S. M. Gho, and C. Liu. 2012. 'Fast and tissue-optimized mapping of magnetic susceptibility and T2* with multi-echo and multi-shot spirals', *NeuroImage*, 59: 297-305.

Wu, B., W. Li, A. Guidon, and C. Liu. 2012. 'Whole brain susceptibility mapping using compressed sensing', *Magn Reson Med*, 67: 137-47.

Yang, X., L. Beason-Held, S. M. Resnick, and B. A. Landman. 2011a. 'Biological parametric mapping with robust and non-parametric statistics', *NeuroImage*, 57: 423-30.

———. 2011b. 'Robust Biological Parametric Mapping: An Improved Technique for Multimodal Brain Image Analysis', *Proc SPIE Int Soc Opt Eng*, 7962: 79623X.

Yoshita, M., E. Fletcher, D. Harvey, M. Ortega, O. Martinez, D. M. Mungas, B. R. Reed, and C. S. DeCarli. 2006. 'Extent and distribution of white matter hyperintensities in normal aging, MCI, and AD', *Neurology*, 67: 2192-8.

Young, I. R., S. Khenia, D. G. T. Thomas, C. H. Davis, D. G. Gadian, I. J. Cox, B. D. Ross, and G. M. Bydder. 1987. 'Clinical Magnetic-Susceptibility Mapping of the Brain', *Journal of Computer Assisted Tomography*, 11: 2-6.

Young, V. G., G. M. Halliday, and J. J. Kril. 2008. 'Neuropathologic correlates of white matter hyperintensities', *Neurology*, 71: 804-11.

Zeineh, Michael M., Yuanxin Chen, Hagen H. Kitzler, Robert Hammond, Hannes Vogel, and Brian K. Rutt. 2015. 'Activated iron-containing microglia in the human hippocampus identified by magnetic resonance imaging in Alzheimer disease', *Neurobiology of Aging*.

Zhang, X., K. Zhou, R. Wang, J. Cui, S. A. Lipton, F. F. Liao, H. Xu, and Y. W. Zhang. 2007. 'Hypoxia-inducible factor 1alpha (HIF-1alpha)-mediated hypoxia increases BACE1 expression and beta-amyloid generation', *J Biol Chem*, 282: 10873-80.

13 Verification of original content

The three main chapters (7, 8, 9) and the list of references were removed before uploading this work to the UZH Docoloc system for verification of original content. The resulting report is shown below.

Docol©c

Docol©c-Report

Digital signiert

Überprüftes Dokument: **Thesis_v1_Verify.docx**
Überprüft am: **6.10.2017 13:47 CEST**

Insgesamt wurden 417 Sätze überprüft. Davon wurden **32** Sätze (7,7%) in anderen Dokumenten gefunden. 1 Satz wurde als Floskel erkannt bzw. als irrelevanter Treffer eingeordnet und daher nicht als Übereinstimmung gewertet.

Die übereinstimmenden Sätze sind im Text je nach Umfang der Übereinstimmung mit unterschiedlichen Farbtönen markiert. Je kräftiger die Farbmarkierung, desto größer ist die jeweilige Übereinstimmung. Die Markierungen im Text können angeklickt werden, woraufhin Details der gefundenen Quellen angezeigt werden. Erfahren Sie mehr über diesen Report und wie dieser interpretiert werden kann.

Die folgende Grafik gibt einen Überblick über die Verteilung der gefundenen Übereinstimmungen im überprüften Dokument. Die farbig markierten Bereiche zeigen die Bereiche des Dokuments, in denen Übereinstimmungen gefunden wurden. Der linke Rand der Grafik entspricht dabei dem Anfang des Dokuments. Ein Klick in die Grafik führt direkt zur entsprechenden Textstelle im Dokument.

Referenzdokumente

Die folgende Übersicht enthält Titel und Adressen der Dokumente, in denen Übereinstimmungen gefunden werden konnten. Durch einen Klick auf die Anzahl gefundener Sätze („**x** Sätze“) werden die entsprechenden Sätze im Dokument sowie im Navigationsbalken mit einem farbigen Rahmen hervorgehoben und es wird direkt zur ersten Stelle gescrollt. Ein erneuter Klick auf „**x** Sätze“ setzt die Markierungen wieder zurück.

2 Sätze wurden gefunden in einer Textvorlage mit dem Titel: „***Diagnosis and Treatment of Alzheimer’s Disease: ...***“, zu finden unter:
https://honors.usf.edu/documents/Thesis/U12419052.pdf

2 Sätze wurden gefunden in einer Textvorlage mit dem Titel: „***ISSN Online: Analyze of some common brain diseases***“, zu finden unter:
http://www.allresearchjournal.com/archives/2017/vol3issue4/PartC/3-4-61-524.pdf

2 Sätze wurden gefunden in einer Textvorlage mit dem Titel: „***u12419052 | Positron Emission Tomography | Medicare ...***“, zu finden unter:
https://www.scribd.com/document/333946671/u12419052

▶ In 139 weiteren Dokumenten wurde jeweils genau 1 Übereinstimmung gefunden. (zum Anzeigen/Verbergen bitte anklicken)

Nachfolgend der geprüfte Text des Dokuments:

CV

Name: Jiri van Bergen
Born: 28-aug-1989, Tilburg, The Netherlands
Nationality: Dutch
Email: jirivanbergen@gmail.com
Address: Dörflistrasse 115, 8050, Zürich, Switzerland
Krijtestraat 34, 5066BH, Moergestel, Netherlands
+41 78 816 8968

Education

2014-2017 **PhD (Dr. sc. nat.) in Neuroscience**
University of Zürich
Institute for Regerenative Medicine (IREM), Neuroscience Center Zürich (ZNZ)

2010-2013 **Master of Science in Medical Engineering**
Eindhoven University of Technology - University Medical Center Utrecht
Coursework and projects focused on diagnostic sensors, MRI, nuclear imaging and image processing.

2007-2010 **Bachelor of Science in Biomedical Engineering**
Eindhoven University of Technology.

2001-2007 **Secondary Education – VWO (Atheneum)**
Odulphuslyceum, Tilburg, The Netherlands

Work experience

2014-2017 **PhD Candidate in Neuroscience**, University of Zürich and ETH Zürich

Title: MRI-PET for investigating cerebral iron-load and associated pathology in preclinical Alzheimer's Disease *(expected graduation December 2017)*

PhD-committee: Prof. Dr. Roger M. Nitsch, Prof. Dr. Klaas P. Prüssmann, PD Dr. Paul Gerson Unschuld

Investigated the role of cortical iron-load in the pre-clinical stages of Alzheimer's disease using advanced imaging techniques on both the Philips 7T MRI and the integrated GE 3T PET-MRI. Until very recent, cortical iron-load was considered not to be of any relevance in Alzheimer's Disease. The results of this work have contributed significantly to iron now being recognized now as an important potential marker of early disease progression before onset of clinical symptoms. The work was the first to demonstrate in vivo using MRI the co-localization of the pathological hallmark of Alzheimer's Disease (β-Amyloid) and iron [1-4, 6, 8].

Further collaborated with medical doctors and clinical support staff to select which state-of-the-art MRI technologies to use in upcoming larger clinical studies. Implemented data-processing and streamlining of the large research data volumes that were new to the research clinic.

Extensive experience with sequence development (GE-EPIC), QSM, multiband-fMRI, MRSI, 7T-field-monitoring technology (Scope), Amyloid-PET, Tau-PET, FLAIR and ASL.

2014 (Jan-June) **Research Assistant at Johns Hopkins Medical Institutions, Baltimore**

Supervisors: Prof. Dr. Peter C. M. van Zijl and Dr. Xu Li

Extended the work on Quantitative Susceptibility Mapping (QSM) and adapted the experimental research focused processing pipeline into an easy to use toolbox. Introduced the toolbox to clinicians from other departments and collaborators to easily process large datasets without manual intervention.

Applied the QSM method to investigate cerebral iron-load in cohorts of Alzheimer's disease, ADHD and in particular Huntington's disease subjects [5, 7].

Research experience

2013 (Jan-Dec) **Master thesis,** Utrecht University Hospital (UMC), Utrecht

Supervisors: Dr.ir. Sjoerd Crijns and Prof. Dr. Klaas Nicolay

Combined new motion correction algorithms for MRI data to make real time tracking of tissues in the abdomen possible. This work facilitated real time motion correction of the radiotherapy treatment on the MRI-linear accelerator in the UMC. Implemented initial compressed sensing approach to improve quality at 2-4x additional accelerated acquisition.

2012 (June-Nov) **Internship at Johns Hopkins Medical Institutions (JHMI)**, Baltimore

Identified that single-head orientation QSM in MRI which could be used to track the disease progress of Multiple Sclerosis and Huntington's disease [5, 7].

2012 (Jan-March) **Internship Neurology at University Hospital Maastricht**, Maastricht

Developed protocols for CHEPS EEG measurements used in the analysis of nerve degeneration. Identified in a small sample that mental distraction from the applied nerve stimuli resulted in significantly lower EEG responses and lower perceived sensation of identical stimuli.

2011 (Sep-Dec) **Internship at MAASTRO Advanced Radiotherapy clinic**, Maastricht

Analyzed 4D-CT images to characterize displacement of lung tissue as a result of cardiac motion. The results of this study suggested that the identified motion would not affect the radiotherapy treatment on targets in the lungs.

Extracurricular activities

2010-2011 **Board member of study association Biomedical Engineering, Protagoras**

Roles: Internal affairs (committees) and Treasurer

Presided over the 13 committees that organized extracurricular activities. Designed and implemented an online registration and payment system for members to sign up for the activities. Managed the finances of the 500+ member study association.

2009-2010 **Study tour committee**, Australia 2010

Organized and guided the 4-week study tour to Australia for 30 biomedical engineering students and 3 faculty members for the purpose of learning about the biomedical industry and universities in Australia.

2008-2014 **Committee work,** study association Protagoras

Financial control committee, IT committee, Introduction committee.

Additional experience

2015-present **Open Source Software Developer**, SABnzbd

Developer of large multi-platform open source application with 150.000+ active users and around 550 new users a day. Boosted processing throughput of the software by over 150%.

Collaborated with a small team to handle user support, bug fixing and feature development. Gained strong affinity with front-end software development (HTML, CSS, Bootstrap, jQuery, KnockoutJS), back-end software development (Python, C), implementation of unit and functional testing, overseeing contributions of other developers, community management and release management.

2008-2017 **Teaching Assistant**, Eindhoven University of Technology and University of Zürich

Courses: Python for Biologists, Big Images, Bio-informatics, Numerical analysis course, Biomechanics, MATLAB and Statgraphics.

2005-2017 **Sail Studio Web design**,

Developer of websites and web-apps for small to medium sized businesses and nonprofit organizations. Communicated with the customer to meet demands, specify design-plans and estimations of costs. Translating ideas of customers into feasible concepts in accordance with budget estimations. Collaborated with front-end designers and code-specialists when projects were too large to handle individually.

Programming skills: PHP (MVC-designs), Javascript (jQuery), HTML5, CSS (Bootstrap)

Skills

Programming: MATLAB, Mathematica, PHP, MySQL, Javascript *(jQuery, Bootstrap)*, HTML5, XML, Python, Pascal, Delphi, C++, GE-EPIC (MRI-sequences), Linux *(shell, OS).*

Languages:

Dutch	*native speaker*
English	*fluent*
German	*limited working proficiency*

Publications and conference presentations

[1] van Bergen, J., et al., 2017. Simultaneous Quantitative Susceptibility Mapping and Flutemetamol-PET reveals co-localization of iron and β-amyloid as a determinant of cognitive performance at high age. NeuroImage (submitted, under review).

[2] van Bergen, J., et al., 2017. Low cortical iron and high entorhinal cortex volume promote cognitive functioning in the oldest-old. Neurobiol Aging (accepted, awaiting publication).

[3] van Bergen, J., et al., 2017. Correlations of beta-Amyloid and brain iron-load (QSM): preliminary results of simultaneous assessment in a large sample. Presentation ISMRM 2017, Honolulu, Awarded ISMRM Magna Cum Laude Merit Award.

[4] van Bergen, J., et al., 2016. Colocalization of cerebral iron with Amyloid beta in Mild Cognitive Impairment. Sci Rep 6, 35514.

[5] van Bergen, J., et al., 2016. Quantitative Susceptibility Mapping Suggests Altered Brain Iron in Premanifest Huntington Disease. AJNR Am J Neuroradiol 37, 789-796.

[6] van Bergen J., et al., 2016, Simultaneous quantitative susceptibility mapping-MRI and 18F-Flutametamol-PET indicate functional impact of cerebral iron and Amyloid-β plaque burden in cognitively normal super-agers. Presented at 14th International Athens/Springfield Symposium on Advances in Alzheimer Therapy.

[7] van Bergen, J., et al., 2015. Magnetic susceptibilities measured by Quantitative Susceptibility Mapping (QSM) indicate brain iron levels correlate with genetic burden in prodromal Huntington's disease . Presentation ISMRM 2015, Toronto, Awarded ISMRM Magna Cum Laude Merit Award

[8] van Bergen, J., et al., 2015. Regional cerebral iron concentrations as indicated by magnetic susceptibilities measured with Quantitative Susceptibility Mapping (QSM) at 7 Tesla correlate with brain Aβ plaque density as measured by 11-C-Pittsburgh Compound B Positron-Emission-Tomography (PiB-PET) in elderly subjects at risk for Alzheimer’s disease (AD). Presentation ISMRM 2015, Toronto